1998

Aluminum powder metallurgy processing

Joel Fredrick Flumerfelt
Iowa State University

INFORMATION TO USERS

This manuscript has been reproduced from the microfilm master. UMI films the text directly from the original or copy submitted. Thus, some thesis and dissertation copies are in typewriter face, while others may be from any type of computer printer.

The quality of this reproduction is dependent upon the quality of the copy submitted. Broken or indistinct print, colored or poor quality illustrations and photographs, print bleedthrough, substandard margins, and improper alignment can adversely affect reproduction.

In the unlikely event that the author did not send UMI a complete manuscript and there are missing pages, these will be noted. Also, if unauthorized copyright material had to be removed, a note will indicate the deletion.

Oversize materials (e.g., maps, drawings, charts) are reproduced by sectioning the original, beginning at the upper left-hand corner and continuing from left to right in equal sections with small overlaps. Each original is also photographed in one exposure and is included in reduced form at the back of the book.

Photographs included in the original manuscript have been reproduced xerographically in this copy. Higher quality 6" x 9" black and white photographic prints are available for any photographs or illustrations appearing in this copy for an additional charge. Contact UMI directly to order.

UMI

A Bell & Howell Information Company
300 North Zeeb Road, Ann Arbor MI 48106-1346 USA
313/761-4700 800/521-0600

Aluminum powder metallurgy processing

by

Joel Fredrick Flumerfelt

A dissertation submitted to the graduate faculty

in partial fulfillment of the requirements for the degree of

DOCTOR OF PHILOSOPHY

Major: Metallurgy

Major Professor: Iver E. Anderson

Iowa State University

Ames, Iowa

1998

Graduate College

Iowa State University

This is to certify that the Doctoral dissertation of

Joel Fredrick Flumerfelt

has met the dissertation requirements of Iowa State University

Signature was redacted for privacy.

Major Professor

Signature was redacted for privacy.

For the Major Program

Signature was redacted for privacy.

For the Graduate College

TABLE OF CONTENTS

ABSTRACT

In recent years, the aluminum powder industry has expanded into non-aerospace applications. However, the alumina and aluminum hydroxide in the surface oxide film on aluminum powder require high cost powder processing routes. A driving force for this research is to broaden the knowledge base about aluminum powder metallurgy to provide ideas for fabricating low cost aluminum powder components. The objective of this dissertation is to explore the hypothesis that there is a strong linkage between gas atomization processing conditions, as-atomized aluminum powder characteristics, and the consolidation methodology required to make components from aluminum powder.

The hypothesis was tested with pure aluminum powders produced by commercial air atomization, commercial inert gas atomization, and gas atomization reaction synthesis (GARS). The commercial atomization methods are bench marks of current aluminum powder technology. The GARS process is a laboratory scale inert gas atomization facility. A benefit of using pure aluminum powders is an unambiguous interpretation of the results without considering the effects of alloy elements.

A comparison of the GARS aluminum powders with the commercial aluminum powders showed the former to exhibit superior powder characteristics. The powders were compared in terms of size and shape, bulk chemistry, surface oxide chemistry and structure, and oxide film thickness. Minimum explosive concentration measurements assessed the dependence of explosibility hazard on surface area, oxide film thickness, and gas atomization processing conditions. The GARS aluminum powders were exposed to different relative humidity levels, demonstrating the effect of atmospheric conditions on post-atomization oxidation of aluminum powder. An Al-Ti-Y GARS alloy exposed in ambient air at different temperatures revealed the effect of reactive alloy elements on post-atomization powder oxidation.

The pure aluminum powders were consolidated by two different routes, a conventional consolidation process for fabricating aerospace components with aluminum powder and a proposed alternative. The consolidation procedures were compared by evaluating the consolidated microstructures and the corresponding mechanical properties. A low temperature solid state sintering experiment demonstrated that tap densified GARS aluminum powders can form sintering necks between contacting powder particles, unlike the total resistance to sintering of commercial air atomization aluminum powder.

CHAPTER 1. INTRODUCTION

Powder metallurgy (P/M) has become important processing method for producing metals parts, because of its high efficiency in moderate to high volume production of net or near-net shapes. Additional advantages of P/M include uniform properties: fine grain structures, and chemical homogeneity. Current consumer products have an increasing number of P/M components and are found in automotive, aerospace, and non-vehicular applications. In automotive applications, ferrous-based P/M parts predominate over all other available P/M materials. However, non-ferrous P/M components are replacing ferrous components for a number of reasons, for example: weight reduction, equal or superior strength to weight ratios, and potential reduction of production costs.

The United States government regulations have compelled automobile manufacturers to improve fuel efficiencies and reduce emissions. To help meet these regulations, the automotive manufactures are exploring the use of powdered aluminum alloys and powdered aluminum metal matrix composites as substitutes for some incumbent ferrous materials in drive train components. The intrinsic properties of aluminum, for example, density and melting temperature, offer attractive incentives for weight reduction and lower metal working temperatures, which translates to lower cost. However, the automotive makers are hesitant to be solely dependent on aluminum P/M processing. For instance, in order for aluminum P/M parts to be practical for use in automobile drive train components, adequate mechanical properties, e.g., fatigue properties, are necessary. Another major issue reducing current costs of aluminum powder production and consolidation.

Since the early 1960's, aluminum P/M processing includes aluminum powder production by gas (air) atomization and powder consolidation into billets for extruding, forging, or rolling into plate or sheet [1]. A major problem with the consolidation of the aluminum powder, particularly during pressing and sintering operations, was due to the

obtrusive and intrinsic oxide film on aluminum powder particle surfaces. In the early to mid-1980's, when high-strength aluminum P/M alloys were consolidated into aerospace components, changes transpired in gas atomization practices to reduce oxide film thicknesses on aluminum powders. Inert gas atomization was deemed an alternate method to air atomization and successfully reduced surface oxide film thicknesses.

Today, in addition to aerospace uses, aluminum P/M has the opportunity to penetrate broadly into high volume production of automotive components. To enhance the viability of the aluminum powder production and consolidation technologies, the process needs further refinement to reduce manufacturing costs. An investment of time and money should lead to improvements of the current aluminum P/M technology. The expected outcome of these advances would be improvements in the quality of P/M components and reduction of manufacturing costs.

To facilitate the necessary research, consortia and conferences provide a forum whereby technical information can be exchanged between the powder producers, part manufactures, and the automotive industry. Throughout my research, personal active involvement within the United States Automotive Manufacturers Partnership (USAMP) consortium and powder metallurgy conferences have facilitated the opportunity to present various aspects of the aluminum P/M research presented in this dissertation.

A literature survey of aluminum P/M shows that many researchers have explored aluminum alloy powder production practices, aluminum alloy powder characteristics, and aluminum alloy powder consolidation methods. However, there is significantly less information available about pure aluminum powders. Yet, some researchers discuss their results with the assumption that the alloy powders behave as pure aluminum powders and do not fully consider the resultant effects of the alloy elements.

A benefit of studying pure aluminum P/M is that the results are unambiguous. The outcome from this research is an extensive database upon which one can more accurately

assess the results observed in the aluminum alloy powders. Therefore, the objective of this research was to broaden the knowledge base of aluminum P/M through a fundamental study of processing pure aluminum powder. To achieve this objective, four topics were investigated: assessment of current gas atomization methods used to produce aluminum powder; powder characterizations of the resulting pure aluminum powders; consolidation of the pure aluminum powders; microstructure and mechanical property analysis of the consolidated powder samples.

CHAPTER 2. BACKGROUND

Aluminum Powder Production

Gas atomization

Industrial production of pure aluminum and aluminum alloy powders typically involves either commercial air atomization (CAA) or commercial inert gas atomization (CIGA). In either case, the direction of molten metal atomization is either horizontal or vertical. The selection of atomizing position depends on the desired production rate of powder and the powder size distribution. Williams [2] comments on three different atomization positions. The vertically upward design, Figure 2.1a and Figure 2.1b, which uses an aspirating mechanism of the aluminum melt to induce upward liquid metal flow, produces a wide particle size distribution at high production rates. The vertically downward position, Figure 2.2a and Figure 2.2b, relies on the liquid metal head pressure for downward fluid flow, has better control over the powder size distribution, but slower production rates than the vertically upward design. The horizontal system can use either the aspirating design or metal head pressure to induce flow of the molten metal. The horizontal set-up produces medium to coarse powder size distributions. The remainder of this document will concentrate on vertical gas atomization designs, both capable of the fine powder production that is the focus of this study.

The vertically upward system is used by Alcoa at the gas atomization facility in Rockdale, Texas, for CAA of aluminum powders. Before atomization, the spray chamber is purged with a gas similar to the atomization gas composition to minimize undesirable gases, such as water vapors. The molten metal is prepared in a holding furnace and transferred to the atomization melt chamber. The liquid metal has a superheat of 100°C to 150°C to eliminate the possibility of the molten aluminum freezing in the pour tube before the melt exits into the spray chamber. Gas nozzles encircle the pour tube and are focused such that

the compressed dry air [3] impinges upon the molten stream, disintegrating the liquid metal into droplets. Immediately after the melt break-up, cooling air from the ambient atmosphere enters the spray chamber to cool the molten droplets and passivate the surface of the droplets with an oxide film [2]. The intent of the passivation process is to purposely oxidize the aluminum powders in an effort to minimize powder explosions during post-atomization powder handling. The cooling air may not have a low enough dew point to minimize

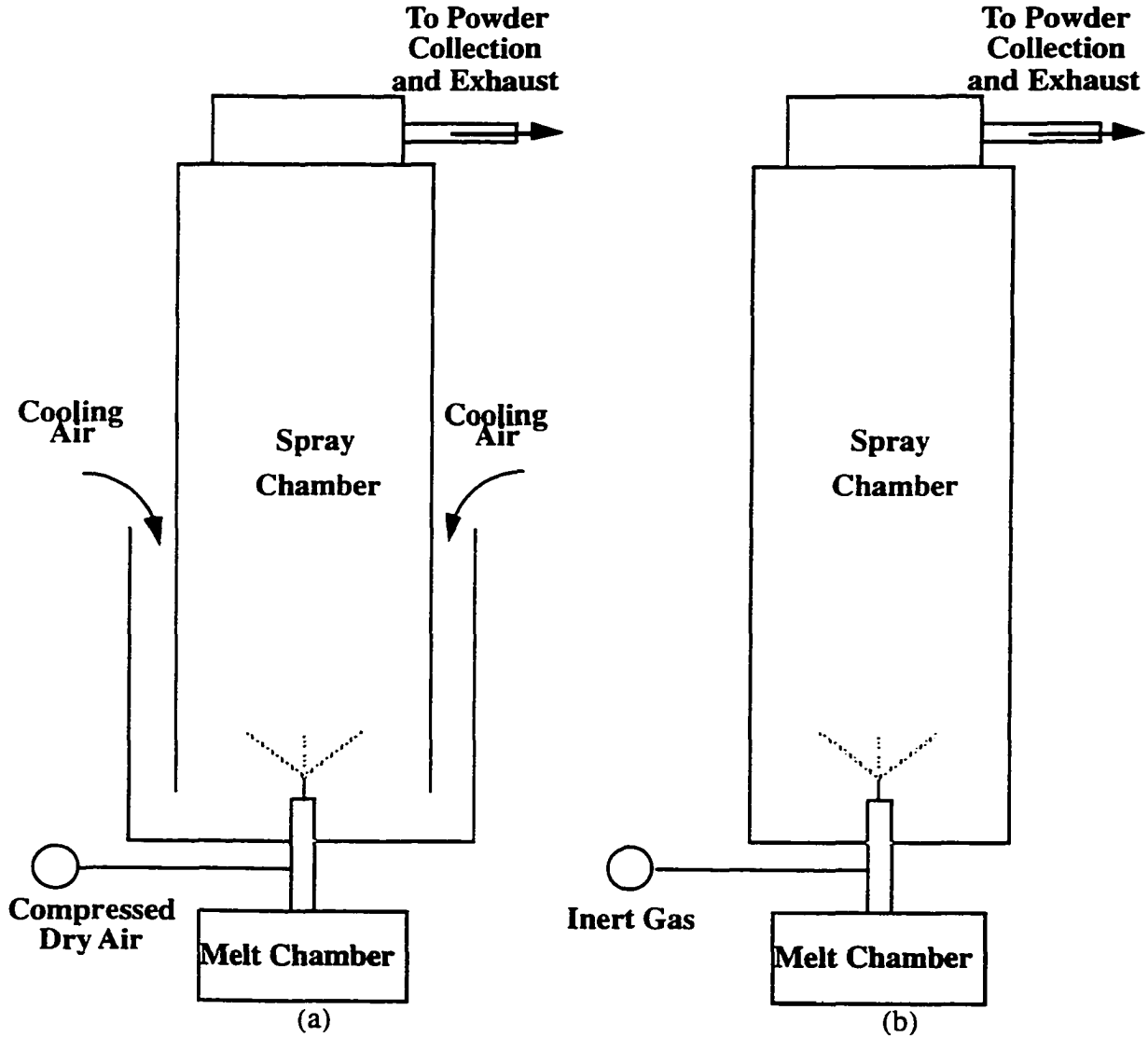

Figure 2.1. a) Schematic of vertically upward atomization system used by Alcoa for CAA of aluminum powders [2]. b) Schematic of vertically upward atomization system used by Alcan-Toyo America for CIGA-ATA of aluminum powders [2, 6].

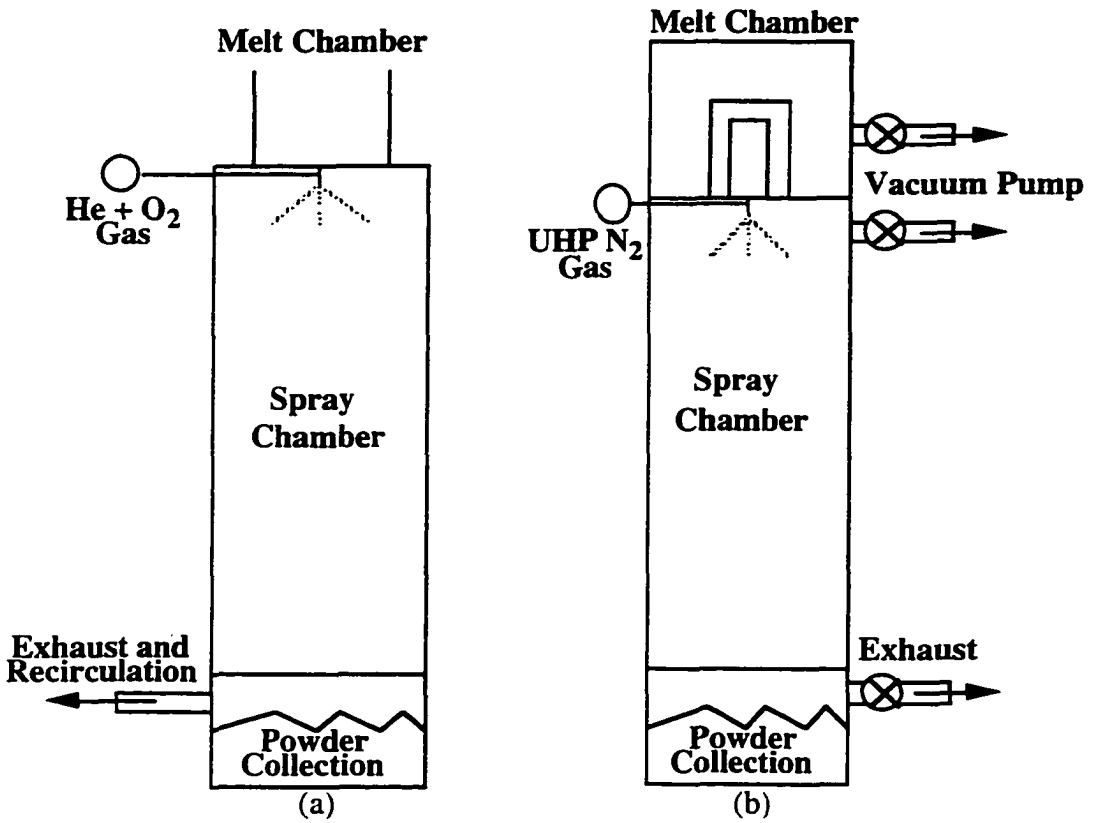

Figure 2.2. a) Schematic of vertically downward atomization system used by Valimet for CIGA-VAL aluminum powders [9]. b) Schematic of vertically downward atomization system used for GARS aluminum powder processing.

hydration of the oxide film [4]. For a point of reference, Bohlen et al. [5] state in their paper that the air atomized process used by Alcoa to produce a 7091 aluminum alloy powder for their research had a dew point of 4°C. After atomization of the melt, the droplets solidify into powder particles and are carried up and out of the spray chamber by the flowing gas. The powders are transferred to cyclones for particle size classification, followed by powder packaging and shipping to the P/M part producers.

A similar atomization system shown is used by Alcan-Toyo America (ATA) in Napierville, Illinois, for CIGA of aluminum powders (Figure 2.1b) but the spray chamber is isolated from the ambient air. Before atomizing, the spray chamber of a CIGA process is purged with an inert gas to remove residual gases, such as air and water vapor [4]. However, Ünal further commented that the purge gas may not completely remove oxygen and gaseous

water from the spray chamber. The implication of incomplete removal of these residual gases would cause the incorporation of the oxygen and water vapor into the oxide film that naturally forms on nascent aluminum metal [4].

The atomization gas used in the CIGA-ATA atomization plant is a by-product of methane (CH_4) combustion in air [6]. Due to proprietary rights on the part of ATA, detailed information about the exact atomization gas is not available. However, one may speculate that the CIGA-ATA atomization gas is similar to flue gas, a dried gas mixture of carbon dioxide (CO_2) and nitrogen (N_2) gases from the combustion of methane in air [7] as shown by equation 2.1. Other forms of inert atomization gases are

$$CH_4(g) + Air + Heat \Rightarrow CO_2(g) + N_2(g) + H_2O(g) \qquad (2.1)$$

used in industry for aluminum powder production. Industrial inert gas, which is similar to flue gas, is composed of gas mixtures of carbon dioxide (CO_2) and nitrogen (N_2) gases [7]. Nitrogen gas produced from liquid nitrogen is another source [7].

The vertically downward atomization system (Figure 2.2a) is used by Valimet, Inc. for CIGA-VAL aluminum powders. The spray chamber is isolated from ambient air and is purged before atomization with an inert gas for similar reasons previously mentioned for the CIGA-ATA aluminum powder production process. The molten aluminum is prepared in a furnace and transferred to the melt chamber by a ladle. The melt chamber volume is kept full to maintain a constant head pressure for the melt to pour into the spray chamber at a constant rate. Upon exiting the pour tube, the molten stream is disintegrated into molten droplets by an atomizing gas nozzle system encircling the pour tube. The used atomization gas is recirculated for reuse to minimize gas consumption costs.

Valimet produces two types of aluminum powders, standard spherical aluminum (SSA) and low oxygen (Lox) powders. The SSA powder is produced by gas atomizing the molten aluminum with a gas mixture of helium and a maximum of two volume percent

oxygen [8]. The powder surfaces oxidize in-flight due to a spontaneous reaction between the oxygen in the atomization gas and the nascent aluminum. The Lox powder is made by atomizing with argon gas and passivating the powder in a powder collection vessel by controlled addition of a gas mixture of nitrogen gas and two volume percent oxygen [9].

An alternative inert gas atomization method, and the subject of this research, is gas atomization reaction synthesis (GARS). The design of the GARS atomization system (Figure 2.2b) is a vertically downward design. The details of the process are described in the Experimental Procedures. In brief, the GARS process uses ultra-high purity (UHP) nitrogen gas for atomization of the molten stream to partially suppress the inherent oxidation kinetics.

Processing effects

In all of the atomization practices described above, the aluminum powders are oxidized in-flight as they pass through the spray chamber. The degree of powder oxidation is proportional to the oxygen content of the atomization gas. Nyborg and Olefjord [10] have derived an expression (equation 2.2a) for oxide thickness, t_{ox} (Å), as a function of partial pressure of oxygen, $p(O_2)$ (Pa), and reaction time, τ (seconds), for a given particle diameter, d (μm). The equation was applied to oxide film growth on ferrous powders during gas atomization, as well as aluminum powder produced by gas atomization [11]. The constant C (equation 2.2b) in equation 2.2a is composed of terms related to physical and chemical properties of the metal, oxygen, and metal oxide, where ρ_{ox} is the oxide density (kg/m^3), $X_{O,ox}$ is the weight fraction of oxygen in the oxide, R is the universal gas constant (J/mol·K), T_g is the gas temperature (K), M_O is the molar weight of elemental oxygen, Sh is the Sherwood number ($Sh= 2+0.6Re^{1/2}Pr^{1/3}$), and $D(O_2)$ is the diffusivity of O_2 in the atomization gas (m^2/s). Equation 2.2a corroborates intuition that atomization gases with large oxygen contents, e.g., air atomization, create thick oxide films on metal powder surfaces.

$$t_{ox} = C \cdot p(O_2) \cdot \tau \tag{2.2a}$$

$$C = \frac{\rho_{ox} \cdot X_{O,ox} \cdot R \cdot T_g \cdot d}{2 \cdot M_O \cdot Sh \cdot D(O_2)} \tag{2.2b}$$

During gas atomization of molten metal, the final particle shape is dependent upon several competing reactions including the oxidizing potential of the atomization gas and liquid metal properties of surface tension and viscosity. Powder spheroidization is a function of the viscosity (σ_m) and surface tension (μ_m) properties of the aluminum melt that are directly dependent on temperature. Nichiporenko and Naida [12] describe an expression (equation 2.3) for the time to spheroidize, t_{sph} (seconds), a molten droplet that is directly dependent on the melt viscosity, μ_m (Pa·s), and inversely dependent on the melt surface tension, σ_m (N/m), where V (m^3) is the powder particle volume, R (m^3) is the particle radius after transformation to the spherical shape and r (m^3) is the particle radius before the transformation. Two assumptions are made by Nichiporenko and Naida, the ratio of R to r is 10 to 1 and the spheroidization occurs in the absence of oxide film formation.

$$t_{sph} = \frac{3\pi^2}{4V} \frac{\mu_m}{\sigma_m} \left(R^4 - r^4 \right) \tag{2.3}$$

Özbilen et al. [13] have shown that the volumetric oxygen content of nitrogen atomization gas affects the aluminum powder particle shape. Their atomization experiments show that increases of the oxygen content in a nitrogen-based atomization gas causes the shape of the powders to become more irregular or less spherical. The limiting volumetric oxygen content of the atomization gas was about three percent oxygen for maintaining spherical or near-spherical shaped powder particles.

An argument for the formation of irregular aluminum powders is based on the decrease of surface tension of the molten aluminum in the presence of oxygen [14]. Özbilen et al. [13] also present another argument for the formation of irregular shape of the aluminum

powder particles. Their first opinion states that molten aluminum droplets in the presence of a high oxidizing potential gas, such as ambient air, will support a large number of nucleation sites for oxide islands to form on each droplet surface. The oxide islands act as pinning sites, restraining the surface tension forces, thus creating powder particles with irregular shapes.

Another argument to support the observation of irregularly shaped aluminum powders is the presence of temperature gradients and compressive stresses in the vicinity of the oxide islands. Because the oxidation of aluminum is an exothermic reaction, the temperature in the region of the oxide may increase, delaying solidification in the region of the oxide. The compressive stresses around the oxide islands develop due to different thermal expansion coefficients of aluminum oxide and aluminum metal. Özbilen et al. [13] cite Spaepen et al. [15] as showing that compressive stresses reduce the melting point of the aluminum, using the Clapeyron-Clausius relation, delaying the droplet solidification. Such an irregular solidification pattern could interfere with the spheroidization driving force of the surface tension properties.

Özbilen et al. concluded that the oxide film on the aluminum powder surfaces would vary in thickness, with thick films formed while the droplet was in the liquid state and thin films between the islands formed after solidification. Nyborg and Olefjord [16] observed similar oxide film thickness variations in their XPS investigation of an aluminum alloy powder produced by helium gas atomization.

Gas atomization conditions, such as pouring temperature, metal flow rate, gas pressure, atomization gas composition and nozzle geometry, affect the aluminum powder size distribution. Ünal [17] discusses these variables of the gas atomization process that appear to be responsible for the resulting powder size distribution. His conclusions summarize his interpretation of the results for the production of AA 2014 aluminum alloy powder. Pouring temperatures greater than 825°C contribute slightly to decreases in the median powder size due to a reduction of the viscosity and the surface tension of the melt with increasing

temperature. The mass median diameter increases proportionally with the square root of the metal flow rate. An increase of the gas pressure shifts the median powder size to lower values, but beyond a certain gas pressure there are diminishing returns with respect to median particle size. Finally, light weight gases, such as helium gas, reduce the median particle size due to higher gas velocities attainable in supersonic flow conditions. A disadvantage to using helium gas is the unit cost, about 34% more than the cost of nitrogen gas in similar compressed gas cylinders. This expense needs to be balanced against the economic value of a finer powder size distribution.

Aluminum Powder Characterization

Bulk chemistry

The bulk chemistry of P/M powders is a quality control point used by P/M parts producers to assure chemical consistency between the different batches of powders shipped to them by the aluminum powder producers. In the case of aluminum P/M, the aluminum alloy composition will determine the elevated metal working temperatures for powder consolidation processes, such as hot isostatic pressing (HIP), vacuum hot pressing (VHP), solid state sintering and liquid phase sintering. If the composition changes from the expected composition, the aluminum P/M parts produced using these types of elevated temperature operations may not meet the design specifications and have to be discarded as scrap.

For example, alloy elements in aluminum metal powder, such as iron, magnesium, silicon, and copper, are known to form low temperature eutectics. If the scheduled temperature of a densification process, such as solid state sintering, is above the solidus of the alloy with the impurities, a liquid phase would form and the consolidated parts would deform. The chain of events would require disposing of the defective parts, decreasing the yield of P/M parts produced, increasing manufacturing costs, which would be passed on to the consumer.

Aluminum powder producers also provide a bulk oxygen content of the aluminum powders. The bulk oxygen content values, though, can be misleading, particularly if the particle size distribution or the surface area of the powders is not available. From a geometrical point of view, if all the oxygen is on the powder surface as an oxide film of uniform thickness and the surface area to volume ratio of the particle increases with decreasing particle size, then the bulk oxygen content increases with decreasing powder particle size. Different researchers have determined with surface analysis methods, e.g., Auger electron spectroscopy (AES) [16, 18] and x-ray photoelectron spectroscopy (XPS) [18, 19], that the oxygen is on the surface of the powder particles in the form of oxide films.

From these aluminum powder surface investigations, the measured bulk oxygen content appears to arise solely from oxides and water molecules combined within the oxide film. A standard oxygen measurement, such as inert gas fusion (IGF), is unable to distinguish between oxygen associated with an oxide or oxygen from water molecules. Both sources of oxygen, oxides and water, originate from the atomization process, i.e., residual oxygen and water vapor in the atomization gas, the spray chamber and/or the powder collection bins.

Powder surface area measurements

The surface area of metal powder can be measured by gas adsorption, permeametry, or from particle size distribution data. The gas adsorption procedure is also known as the Brunauer-Emmet-Teller (BET) method [20, 21]. BET determines the surface area of a powder sample by measuring the amount of gas necessary to cover the powder surface with a monolayer of gas [20]. Typical gases included nitrogen for surface areas greater than one meter squared per gram or krypton for specific surface area less than one meter squared per gram. A strong attribute of the BET method is its ability to include surface area measurements of interior surface-connected pores [20]. BET measurements are suitable for

powder particles of any size and shape.

Gas permeametry measures the resistance of a flowing gas through a powder bed [20]. The technique is limited to powder sizes ranging from 0.5 to 50 μm and is only an approximate measurement tool as it does not assess the dead ended surface connected porosity [21]. Despite some of the limitations of gas permeametry, the method is simple, reproducible to ± 1%, quick, and low cost compared to the equipment costs of other methods, such as BET.

A particle size distribution analysis of a powder sample can also provide a calculated surface area measurement, assuming the shapes of the powder particles are spheres, the powder is not agglomerated, and there are no powder satellites attached to the surface of the powders. If the powder generally meets these requirements, the calculated surface area is a reasonable value [4]. However, the calculated surface area value should not be interchanged with BET measurements, because the calculated surface area does not reflect surface-connected porosity or other topographic characteristics of the powder particles [20].

Aluminum powder surface characterizations

Surface characterization investigations of aluminum powders typically use instrumentation, such as transmission electron microscopy (TEM) [22, 23], AES [11, 24], and XPS [11, 23, 25], to analyze the oxide film. Researchers tend to use various combinations of these techniques for their surface oxide evaluations. Each analytical instrument provides a different view of the same oxide film.

TEM can provide information about the oxide chemistry, oxide thickness, and oxide structure, i.e., whether or not the oxide film is crystalline or amorphous. The oxide chemistry can be measured by various methods, e.g., energy dispersive spectroscopy (EDS) and/or parallel energy electron energy loss spectroscopy (PEELS). A bright field image of the oxide film permits direct measurements of the oxide thickness from either individual powder

particles or from the oxide boundary between two powder particles [26]. The oxide structure can be determined with either secondary area diffraction (SAD) patterns or convergent beam diffraction (CBD) patterns. The difficulty with these last two measurements is focusing the electron beam to a small enough cross-section to minimize detection of neighboring crystalline features. In general, TEM sample preparation is laborious, tedious and time consuming.

AES and XPS, on the other hand, offer relatively simpler sample preparation methods and provide measurements of the oxide film thickness and oxide film chemistry. Both spectroscopic techniques use argon ions for sputtering, or etching away, successive layers of the oxide film and measuring the elemental composition of each layer. The data is presented as elemental composition depth profiles of the oxide film on aluminum powder particles. An advantage of AES is the ability to carry out a point analysis on individual powder particles, providing a comparative measure between fine and coarse powders [16]. The XPS analysis, on the other hand, is an average of many powder particles within a definite area on the order of one square millimeter.

Another type of surface analysis of the oxide film on aluminum powder particles is possible with quadrupole mass spectroscopy (QMS). QMS detects and measures the gases that evolve from the surfaces of the aluminum powder particles during a continuous heating of the powder sample under a dynamic ultra-high vacuum (UHV). The gases typically measured are water and hydrogen, the sources of which comes from water physically adsorbed onto the powder particles' surfaces (physiosorbed water) and water chemically bound within the oxide film (chemisorbed water). In some instances, carbonaceous gases, e.g., carbon monoxide and carbon dioxide, are measured also, but carbon-based gases are more difficult to identify with QMS.

The origins of the physiosorbed and chemisorbed water are traceable to the atomization process and post-atomization powder handling [24, 25]. Direct comparisons of

the QMS results show aluminum alloy powders produced by inert gas atomization have less chemisorbed and physiosorbed water than aluminum alloy powder manufactured by air atomization [27]. A similar type of investigation [25] used aluminum-magnesium base alloys to show that "wet" atomization gases produce more chemisorbed water in the oxide films of aluminum powder particles than "dry" atomization gases. The same research showed no significant difference of the physiosorbed water quantity on the aluminum powders produced by either atomization gas.

The hydrogen detected during QMS experiments is a product of the physiosorbed water or chemisorbed water reacting with aluminum cations diffusing through the oxide film [28, 29]. Possible reactions for the hydrogen product are shown with equations 2.4, 2.5, and 2.6. There is uncertainty and speculation as to which reaction or reactions may be dominant during the heating of the powder sample [28].

One method of hydrogen analysis is a vacuum extraction analysis as described by Peterson et al. [30] and Devrève et al. [31]. In brief, the aluminum sample is heated

$$2Al + H_2O \Rightarrow Al_2O_3 + 3H_2 \qquad (2.4)$$

$$2Al + 6H_2O \Rightarrow Al_2O_3 \cdot 3H_2O + 3H_2 \qquad (2.5)$$

$$2Al + 4H_2O \Rightarrow Al_2O_3 \cdot H_2O + 3H_2 \qquad (2.6)$$

to a temperature of greater than 600°C and less than 800°C, under vacuum conditions of 3.2×10^{-2} Torr to 1×10^{-6} Torr. The hydrogen evolved from the aluminum specimen is collected in a collection volume of known capacity and the pressure increase within the collection volume is measured. Once the pressure reaches a constant value, the hydrogen from the sample is inferred to be completely removed. The equilibrium pressure value is directly proportional to the mass content of hydrogen that was in the aluminum sample. Depending on the system available, the hydrogen extraction process is the rate limiting step, and the calculated hydrogen content can be determined within twenty minutes to several

hours [30].

Caution though is warranted for determining the hydrogen content of aluminum. The measured hydrogen content of aluminum ingots may be influenced by several variables, such as sample porosity, surface contamination, oxide thickness, and grain size [32]. As a result, there are no consistent experimental hydrogen content values for aluminum [33].

Hydrogen analysis of aluminum powders adds one more variable to the list mentioned in reference [32], that needs consideration, the water content of the oxide film. Under the elevated temperature and vacuum conditions, the physiosorbed and chemisorbed water would be removed from the oxide film, and if some of the water did not react with aluminum to form hydrogen, the unreacted water would be gathered into the collection volume with the hydrogen. The water in the collection volume would contribute to the measured pressure, leading to an artificially high hydrogen content of the aluminum powder.

Explosibility of aluminum powders

In 1964, the United States Department of the Interior, Bureau of Mines, prepared a document for the explosibility of metal powders [34]. The report is a standard for all metal powder explosibility testing. The comprehensive investigative report provides explosibility data on 313 elemental metal, alloys, catalysts, and ores comprising 54 types of material. An empirical explosibility index (EI) is used to rate each material tested. The EI value is the mathematical product of the ignition sensitivity (IS) and the explosion severity (ES) (equation 2.7). Table 2.1 lists the relative explosion hazard index with the corresponding index of explosibility ranges. As the information in the table implies, a larger EI value means a more severe explosion.

The ignition sensitivity assumes a dependency on the ignition temperature (IT), minimum ignition energy (MIE), and the minimum explosive concentration (MEC) (equation 2.8). The explosion severity assumes a dependency on the maximum explosion pressure

Table 2.1. Legend for the explosive hazard index and the designated range of values for the index of explosibility [34].

Explosive Hazard Index	Index of Explosibility
None	0
Weak	<0.1
Moderate	0.1 - 1.0
Strong	1.0 - 10.0
Severe	>10

(MEP) and maximum rate of pressure rise (MRPR) (equation 2.9). A value of unity is assigned to the explosibility index, ignition sensitivity, and the explosion severity for materials that have similar ignition and explosion characteristics as Pittsburgh seam coal dust.

The explosibility tests are conducted in a twenty liter spherical dust explosion chamber as described in reference [35]. The metal powder is dispersed in the air inside the explosion vessel and the explosibility of the metal powder is determined. In the case of MEC values, Safety Consulting Engineers, Inc., advises discretion in the interpretation of the MEC

$$EI = IS * ES \tag{2.7}$$

$$IS = \frac{(IT * MIE * MEC)_{Pittsburgh\ Coal\ Dust}}{(IT * MIE * MEC)_{Powder\ Sample}} \tag{2.8}$$

$$ES = \frac{(MEP * MRPR)_{Pittsburgh\ Coal\ Dust}}{(MEP * MRPR)_{Powder\ Sample}} \tag{2.9}$$

values, because the processing conditions and handling of the metal powders strongly influence the degree of hazard [36], i.e., the results should be considered "preliminary results" [37].

There are several variables that contribute to dust explosions, such as particle size, particle shape, particle reactivity, distribution in air or gas media, turbulence, size of cloud and confinement, ignition source size, and ignition delay. As an example of one variable effecting dust explosions, aluminum powder particle size has been correlated with MEC

values [2]. The findings show that the MEC becomes more severe with decreasing aluminum powder particle size. The argument for this observation is that small aluminum powder particles have large surface areas compared with the small surface areas of large aluminum powder particles. Hence, for the small aluminum powder particles, there is more area available for a reaction to occur between the aluminum powder particle and the atmospheric air.

There is experimental evidence available that indicates nitrogen plays a major role in the combustion of aluminum in air [38]. These authors reference a study by Prentice [39] that investigated aluminum burning in an argon-oxygen atmosphere during which he observed a clean metal surface, whereas burning in air created an oxide on the powder. Boborykin also reference other research [40, 41] conducted in pure nitrogen and oxygen mixtures with argon or nitrogen in which aluminum nitride was formed.

Consolidation of Aluminum Powders

Press and high interparticle shear consolidation

A typical consolidation route that an aerospace P/M parts producer would use for consolidating aluminum alloy powders is shown in Figure 2.3. The sequence begins with the production of gas atomized aluminum powder by one of the commercial methods described at the beginning of this chapter. The as-atomized powder is sieved or pneumatically classified to achieve the desired particle size distribution for cold isostatic pressing (CIP). Ideally, the CIP compact should be pressed to a green density of about 75% of theoretical density to ensure an open porosity network for effective degassing of the aluminum powders [42]. The compaction pressure needed for the ideal green density can be determined from a compressibility curve [43].

After the powder is consolidated by CIP, the green compact is placed in a sealed aluminum metal can, except for an open vent pipe to allow the escape of water vapor and

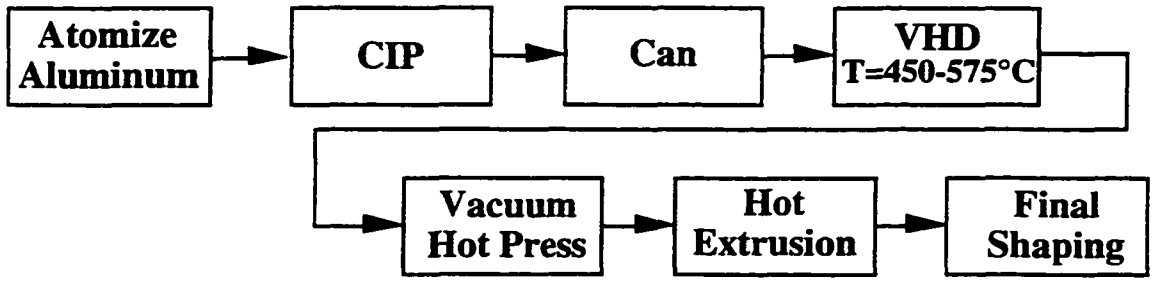

Figure 2.3. Conventional consolidation sequence for aluminum powders used in aerospace applications [1].

gaseous hydrogen from the can during the vacuum hot degassing (VHD) procedure. For the sources of hydrogen evolution refer to equations 2.4, 2.5, and 2.6 above, and see equation 2.10 and 2.11 below for the water vapor sources in the oxide film. The maximum temperature for VHD depends on the solidus temperature of the aluminum alloy powder, which can range from 450°C to 575°C. The purpose for VHD of the green compact is to eliminate the physiosorbed and chemisorbed water from the oxide film on aluminum powder particles. Equations 2.10 and 2.11 describe the dehydration sequence according to the research of Litvintsev and Arbuzova [28].

QMS experimental evidence has shown the oxide film on aluminum powders to be a duplex structure of alumina (Al_2O_3) and alumina trihydrate ($Al_2O_3 \cdot 3H_2O$), with physiosorbed water present on the surface of the oxide film [27]. As the green billet is heated to the degassing temperature, the physiosorbed water evaporates from the oxide surface according to equation 2.10. The decomposition reactions of the hydrated alumina phases are represented in equation 2.11. The trihydrate phase is thermally stable to about 150°C. Above 150°C and below 175°C, chemisorbed water is removed from the trihydrate phase, forming the $Al_2O_3 \cdot 2.5H_2O$ hydrated alumina phase. As the temperature continues to increase from 175°C to 310°C, more chemisorbed water is removed from the $Al_2O_3 \cdot 2.5H_2O$ phase to form the alumina monohydrate ($Al_2O_3 \cdot H_2O$) phase. From 310°C to 500°C, the monohydrate phase is thermally stable. As the temperature increases above 500°C, the monohydrate phase decomposes to an anhydrous alumina (Al_2O_3) phase. If the aluminum

powder is an aluminum alloy with magnesium additions, the highly mobile and reactive magnesium can react with water to form MgO and hydrogen gas, equation 2.12.

$$H_2O_{phys} \Rightarrow H_2O(g) \tag{2.10}$$

$$Al_2O_3 \cdot 3H_2O \Rightarrow Al_2O_3 \cdot 2.5H_2O \Rightarrow Al_2O_3 \cdot H_2O \Rightarrow Al_2O_3 \tag{2.11}$$

$$Mg + H_2O \Rightarrow MgO + H_2(g) \tag{2.12}$$

The typical size of the vacuum hot pressing (VHP) cans range from 25 cm to 76 cm in diameter and the billet mass is 50 kg and 1545 kg, respectively [1]. For the small billet sizes, Billman et al. state the VHD is conducted under a dynamic vacuum during heating and a one hour soak at the VHD temperature, the entire process requires about seven hours. For the large billets, the same authors comment that the billets are heated under argon, either static or hot flowing argon, with a one hour vacuum soak near the end of a thirty hour heating cycle. Typical degassing times at degassing temperature vary from twenty-four hours at the periphery of the billet to one hour at the center of the billet. The degassing temperature should be below the solidus of the aluminum alloy powder, and the time at temperature should be limited to minimize coarsening of the microstructure [1, 42].

Immediately following the VHD procedure, the can is sealed to maintain an evacuated atmosphere within the interconnected porosity of the green billet [1]. Billman et al. state that sealing the evacuated sample prevents exposure to air that could react with the heated P/M billet to form nitrides and oxides within the interconnected porosity. After welding the can closed, the sample is VHP to close the interconnected porosity [42]. Kim continues to comment that the material flow during VHP is adequate to disrupt the dehydrated oxide film into alumina fragments. However, the alumina fragments remain along the prior particle boundaries of the powder particles, leading to incomplete powder particle bonding. Hot extrusion of the VHP billet is necessary to distribute the alumina fragments throughout the matrix. The deformation is completed at extrusion ratios about

20:1 [42]. The shape of these extrusions can be round bar or rectangular bar. The last step of the aluminum powder consolidation is the shaping of the final P/M part by closed die forging and/or machining methods. High economic costs are association with the energy consumption necessary to heat the powder samples for VHD, VHP, and hot extruding. The escalated expenditures limit the use of this consolidation procedure to high-tech applications, prohibiting its use for low cost applications, such as automotive drive train components.

Press and sinter consolidation

Another method used for consolidating metal powders is a pressing and sintering process (Figure 2.4). After the powder is gas atomized and size classified, the aluminum

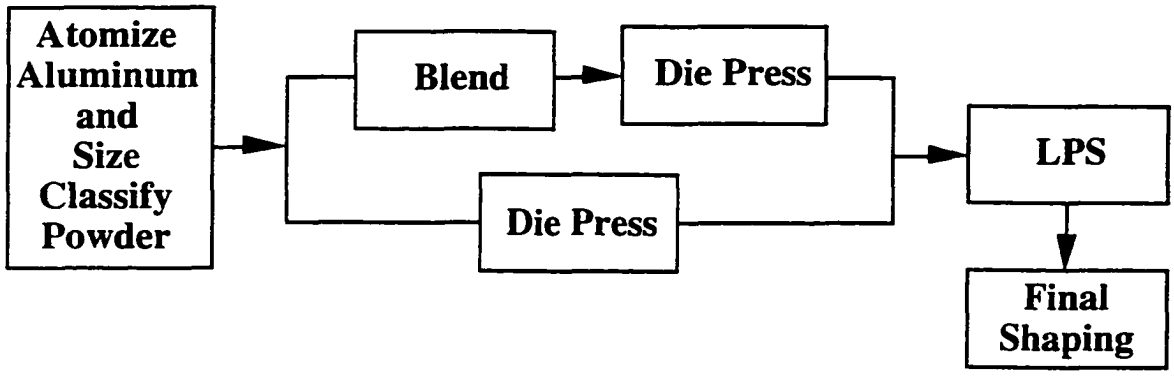

Figure 2.4. Press and liquid phase sintering (LPS) route for aluminum P/M components.

powder can follow one of two routes. Either pure aluminum or aluminum alloy powder is immediately die pressed into the component shape or the aluminum powder is blended with elemental or master alloy powders and then die pressed. The blending procedure may involve mixing non-metallic particles, e.g., alumina and silicon carbide, and/or other metal powders, e.g., copper, magnesium, iron, silicon, zinc, for alloy additions. After die pressing, the green component is transferred to a sintering furnace to thermally enhance densification by liquid phase sintering. Solid state sintering is not practiced because of poor fracture resistance related to oxide powder surfaces. The sintered P/M aluminum part may require

secondary finishing operations, such as drilling, milling, turning, and grinding, which are easily performed on aluminum P/M components [44].

Die pressing

The powders or powder blends that fill the die need to flow well for automated, high production rate presses. The powder particle shape and size affect the flow of the powder into the die. Spherical powders greater than 45 μm in diameter are ideal for die filling, because the powders roll into the die cavity and have low interparticle friction characteristics [45]. Irregular powder particle shapes or fine spherical powders have high surface area to volume ratios that increase the interparticle friction, decreasing the powder flowability [45].

After filling the die cavity, the aluminum powders are squeezed together to make a densified green compact. The ability of the aluminum powders to deform depends on the compressibility characteristics of the powder or powder blend. The oxide film on aluminum powders is one variable that influences compaction of aluminum P/M parts due to the hardness of the oxide [43]. During the compaction process, the powders deform to fill the empty spaces between the powder particles. The presence of the oxide film can slow the deformation of the particles and even inhibit interparticle bonding. Particle shape and size influence the compressibility of the powders, too. Ideally, a P/M parts producer would use spherical powders with a good mixture of particle sizes for filling the maximum space within the die cavity [43]. However, irregular shaped aluminum powder particles are often preferred, in spite of reduced die filling capability, because of mechanical interlocking between the powder particles that enhances the green strength of the compact.

The inherent hardness of the metal powder is another variable effecting compressibility and is dependent on whether aluminum alloy ("prealloyed") powders or elemental powder alloy blends are used. The elemental powder blends are powder mixtures of aluminum powder with other metal powders, such as copper, magnesium, iron, silicon,

and/or zinc. The elemental blends would deform easier at lower compacting pressures than the prealloyed powders [46] due to the elemental powders being softer and more ductile than the prealloyed aluminum powders. In other words, the prealloyed aluminum powders will work harden more and faster than the elemental blends, due to the alloy additions in the matrix, requiring higher compaction pressures for the prealloyed powders. Higher green densities and higher green strengths are advantages to using elemental blends for powder compaction [46] compared to prealloyed powder compacts.

The powder compact ejected from the die has green properties that are dependent on the powder and die pressing conditions. The green density of the P/M aluminum component is directly proportional to the compaction pressure applied to the powder. The compacting pressure, compaction method, and the geometry of the P/M aluminum part influence the magnitude of density gradients within the powder compact [21]. The green strength is directly dependent on the green density and the compaction pressure [21], in other words, as the number of metallurgical bonds created during the die pressing operation increases, the green strength increases. A thick oxide film would inhibit the formation of metallurgical bonds and lead to poor green properties.

Sintering

The green aluminum P/M compact is further densified by sintering, an elevated temperature process to increase the strength of the green compact by bonding adjacent particles by diffusion mechanisms [21]. P/M aluminum sintering may either occur in the solid state or partial liquid state [47]. The former is rarely used whereas the latter is widely used for either elemental powder blends or blends of aluminum powder with master alloy powders.

During solid state sintering, five diffusion mechanisms are possible as shown in Table 2.2. Two of the five mechanisms enhance densification and the other three merely coarsen

the microstructure. A major barrier to the solid state sintering process, and diffusion, is the oxide film thickness on aluminum powder particles [48], reported to range from 40Å to over 200Å [42]. The oxide film may break during the pressing operation, creating cold welds between the powder particles. Gutin et al. [48] make two conclusions from their research. During sintering of lightly oxidized aluminum powders, atoms diffuse over the entire area of contact between the powder particles. On the other hand, during the sintering of severely oxidized aluminum powders, the aluminum atoms diffuse only in the oxide-free zones of the powder particle contacts and the area of interparticle contact does not increase in size.

Munir [49] has developed a predictive model that describes the influence of the surface oxide layer on interparticle neck growth, as determined by the relative sintering

Table 2.2. Possible diffusion mechanisms occurring during solid state sintering [21].

Diffusion Mechanism	Source	Sink	Comments
Volume	Surface	Neck	Coarsening
Surface	Surface	Neck	Coarsening
Vapor Mass	Surface	Neck	Coarsening
Volume	Grain Boundary	Neck	Densification
Grain Boundary	Grain Boundary	Neck	Densification

and diffusional fluxes, x_s and x_d, respectively. The ratio of these fluxes defines the neck growth rate ratio. A neck growth rate ratio greater than one would indicate a retardation of sintering by the oxide layer. If the same ratio is less than or equal to one, sintering continues uninhibited.

Table 2.3 is an excerpt from Table 1 in Munir's paper that shows the neck growth rate ratio as function of sintering temperature and the ratio of the oxide thickness (ξ) to the particle radius (r). For a given aluminum powder size and sintering temperature, as the oxide film thickness increases, the neck growth is increasingly more difficult. Iron, on the other hand, would show good sintering behavior, because the neck growth rate ratio is constant or decreases with an increasing ξ/r ratio (Table 2.3). For both these metals, Munir's model correlates well with experimental results of solid state aluminum powder sintering [48] and

explains the wide spread industrial use of iron-based powder alloys in automotive applications.

The successful solid state sintering of metal powders depends on sintering temperature, sintering time, and sintering atmosphere [50]. A limitation to solid state sintering of aluminum powders is the continuous native aluminum oxide on all aluminum powder particles that inhibits diffusion of aluminum atoms between adjacent powder particles. Another limit to sintering temperature is the effect of alloy elements previously discussed.

Table 2.3. Neck growth rate ratio for solid state sintering aluminum and iron powders as a function of temperature and the ratio of the oxide thickness to particle radius [49].

Metal	Temperature (°C)	ξ/r		
		10^{-5}	10^{-3}	10^{-1}
Aluminum	224	1.7×10^{31}	1.7×10^{33}	1.5×10^{35}
	660	3.3×10^{12}	3.3×10^{14}	3.0×10^{16}
Iron	633	1.0	1.0	1.0
	1539	1.0	1.0	1.0

Liquid phase sintering (LPS) of aluminum alloy elemental blends enhances densification of the microstructure. The LPS temperature is based on the composition of the aluminum alloy, typically in the range of 595°C to 625°C [44]. The sintering time ranges from ten to thirty minutes in a variety of sintering atmospheres, dissociated ammonia, hydrogen, argon, nitrogen, and vacuum [44]. A nitrogen sintering atmosphere is preferred over the other atmospheres, because of the relatively high, as-sintered, mechanical properties of the P/M aluminum parts [44]. Nitrogen gas is also quite economical in large quantities compared to the other gases available for sintering atmospheres. Another sintering variable related to the sintering atmosphere is the dew point of the protective atmosphere. The recommended dew point is less than -40°C, which corresponds to a maximum moisture content of 120 parts per million by atomic percent [44]. A dew point lower than the recommended value minimizes oxidation during the sintering operation [50].

To reduce the costs of sintering green P/M aluminum parts, researchers have experimented with air sintering. Storchheim [51] published a paper in which he describes the viability of using convention P/M process equipment to sinter green aluminum P/M parts in air. The initial sintering experiments were generally poor, requiring thorough evaluation of problems related to the powder size distribution, alloy composition, heating rates, sintering times, and lubrication issues. After implementing solutions to address these problems, the air sintered P/M parts had reasonable mechanical properties after using a T-4 heat treat condition.

A goal of aluminum P/M liquid phase sintering is to homogenize a green microstructure composed of an elemental powder blend. Homogenization occurs by the formation of a liquid phase between the elemental constituents, i.e., the creation of a short circuit diffusion path between the chemical elements [46]. There is a large chemical potential, and hence a large driving force for chemical homogenization, between the solute powders and the aluminum powders. The presence of the liquid phase also permits rearrangement of the aluminum powder to enhance further densification [50].

The liquid phase sintering process is limited to a small number of aluminum alloy powder blends, such as 601AB and 201AB alloy powders. The 601AB alloy is comparable with the composition of the 6061 wrought aluminum alloy and the 201AB alloy has a composition similar to a 2014 wrought aluminum alloy. An advantage of elemental aluminum powder blends is the starting powders can be of high purity, whereas the primary constituents used to make the prealloyed powders may have undesirable impurities.

There are disadvantages to liquid phase sintering aluminum alloy elemental powder blends. One drawback is the large scale heterogeneous microstructure that is present in the as-compacted state, which can be exaggerated with blending elemental powders of significantly different sizes. Another downfall to liquid phase sintering is the oxide film on the aluminum powders may or may not break open during compaction to allow

homogenization of the aluminum alloy [47]. In the case where the aluminum oxide is not disrupted, the oxide film may be too thick for chemical diffusion of aluminum or the elemental constituents through the oxide film. The dimensional control of the P/M compact is a variable that is difficult to maintain during liquid phase sintering. The liquid phase fraction must be small enough to be held by capillary force within the skeleton of the remaining solid phase to retain the compact shape [46]. Coarsening of the microstructure is another problem with liquid phase sintering. The average grain size increases with either the one-half or one-third power of time and is quite sensitive to temperature changes, i.e., elevated temperatures increase grain growth [21].

Aluminum Alloys, Reinforcement Phases, and Mechanical Properties

During the last two decades, P/M processed, high strength aluminum based materials have been designed for elevated temperature use in aerospace applications, such as struts and other structural members. P/M aluminum materials have gained acceptance in critical applications because of their reduced weight and relatively high strength at elevated temperatures. There are two distinct examples of aluminum reinforced P/M materials. One is a uniform blend of aluminum powder and an "extrinsic" dispersoids like silicon carbide or alumina particulates. The other is a rapidly solidified aluminum powder with "intrinsic" dispersoids containing metastable phases such as Al_6Fe found in Al-Fe-X alloys, where X is another transition metal or rare earth metal. The strength of these two types of reinforced aluminum powder materials is attributed to the distribution and thermal stability of each phase in the consolidated microstructure.

Extrinsic dispersoids: Composites

Extrinsic dispersoids include oxides, carbides, and nitrides that are blended with either pure aluminum or aluminum alloy powders and are bonded during composite

consolidation. An example is Al-SiC(p) alloys processed by blending aluminum alloy powder with SiC(p), typically ranging from 4-10 μm [52]. Composite strength with extrinsic dispersoids is improved over conventional P/M aluminum alloys, but the ductility decreases at elevated temperatures, due to pore opening at the aluminum-dispersoid interface [53]. The ambient temperature ductility of Al-SiC(p) composites is good, but extensive mechanical work is often necessary to provide an adequate level of ductility. The mechanical deformation process decreases the matrix porosity, creates new surface for aluminum powder bonding, and disperses the reinforcement particulates more uniformly. These composites have demonstrated ultimate tensile strengths to about 350 MPa at 200°C, decreasing to about 300 MPa at 260°C [54]. This would indicate that a typical Al-SiC(p) composite could be used for long durations at 200°C and for short durations at 260°C.

Intrinsic dispersoids: Rapidly solidified alloys

Intrinsic dispersoids are hard intermetallic compounds that form within the aluminum matrix during P/M aluminum powder processing, and exist as either equilibrium or metastable compounds. For example, the Al-Fe-X alloys, where X is either vanadium, cerium, cobalt, or molybdenum, have been processed to produce equilibrium Al_3Fe, its precursors Θ' and Θ", or metastable Al_6Fe. The ternary additions have high liquid solubility and low solid solubility to promote copious precipitation of the desired intermetallic phases. These aluminum alloys are produced by either gas atomization or melt spinning to promote supersaturation of the alloying elements in the aluminum powder matrix by a rapid solidification process. By controlling the rapid solidification process and fabrication techniques, high volume fractions of finely dispersed intermetallic phases can be produced, giving a dispersion strengthened alloy with high strength and dispersoid thermal stability at elevated temperatures [55]. The size of the dispersoids in a Al-12Fe-2V alloy, i.e., Θ", Θ', or Al_3Fe [56] can vary from 40 to 100 nm [57]. The ultimate tensile strength begins to decrease

rapidly from 500 MPa at temperatures greater than 240°C [56]. Cerium additions to the Al-Fe system have been observed to retard coarsening of the intermetallic phases and suppress the formation of Al_3Fe in favor of more stable, high temperature ternary phases [58], $Al_{10}Fe_2Ce$ and Al_8Fe_4Ce [59]. The tensile strength of Al-Fe-Ce alloys begins to decrease significantly from 300 MPa at 290°C [55] due to microstructural phase coarsening [60]. Al-Fe-Ce alloys have fair ductility, about 6% elongation at 230°C, and fair toughness at elevated temperatures, but thermomechanical processing improves these properties [58]. All aluminum P/M materials form an oxide surface film on the particles during atomization [61], requiring extensive mechanical deformation to disrupt the oxide layer and develop adequate interparticle bonding for sufficient ductility.

Residual gas contamination within the P/M aluminum alloy matrix, such as hydrogen gas, may have deleterious effects on the microstructure and mechanical properties of the aluminum or aluminum alloy P/M component. Kim [61] discusses how the presence of hydrogen is one variable that influences the microstructure and tensile properties of Al-8.4Fe-7.2 Ce, an aluminum alloy produced by gas atomization with flue gas. The tensile properties measured as a function of temperature showed a decrease of tensile strength with increasing temperature. Kim attributes the tensile strength decrease to hydrogen gas released from the decomposition of hydrated oxide fragments. In tension, the neck area relaxes and the newly formed hydrogen assists in crack formation. The size and number of cracks increase with temperature and have the effect of decreasing the cross-sectional area of the tensile specimen.

A New "Hope": Gas Atomization Reaction Synthesis

The problems described so far with aluminum powder processing can be minimized or even eliminated with an atomization method developed at the Ames Laboratory, Gas Atomization Reaction Synthesis (GARS) [62]. The GARS project had the original intent of

producing intrinsic-like dispersoids in the aluminum matrix by a reaction between the atomization gas and the molten aluminum. The key to manufacturing materials with intrinsic dispersoids is to take advantage of a rapid solidification process, such as gas atomization, which extends the solid solubility in many metal alloy systems. However, instead of an enhanced solute addition to the melt in the crucible, the GARS method adds an excess of a reactive gas solute into the molten aluminum droplet, which is trapped in the rapidly solidified aluminum particle. A dispersion hardened aluminum material can be produced by annealing the supersaturated aluminum powders to promote uniform precipitation of refractory compounds, such as nitrides or carbides, within the aluminum matrix. Ideally, each annealed aluminum powder particle would essentially be a metal matrix composite with refractory dispersoids, similar in nature to SiC, dispersed homogeneously as a highly refined reinforcement particulate. After consolidation of these powders, the result would be an aluminum P/M composite formed by an intrinsic dispersoid precipitation mechanism.

To test the GARS process, high-purity aluminum metal was gas atomized with UHP nitrogen gas. The specific goal was to react the nitrogen gas with the aluminum droplets to create a P/M Al-AlN metal matrix composite. During the atomization process, no measurable temperature increases were recorded with a two color optical pyrometer that would indicate an exothermic reaction between the nitrogen gas and the molten aluminum. Extensive post-atomization analysis of the GARS aluminum powders revealed no conclusive evidence of nitrogen supersaturation of the aluminum matrix or formation of AlN. The reaction between the nitrogen gas and the aluminum metal was apparently by-passed because of two physical barriers, a) the limited liquid solubility and negligible solid solubility of nitrogen gas in aluminum [63], and b) the competition between nitridation and oxidation. Even though gas atomization has the potential to extend the solubility limits of metal alloy systems, any extension of the nitrogen solubility limit in the aluminum-nitrogen system was negligible. The dominant physical barrier to nitridation was oxidation [18], both from a

thermodynamic argument, i.e., the nitrogen and oxygen Ellingham diagrams [64, 65], and from kinetic evidence [66].

A re-evaluation of the results from another perspective did reveal the GARS pure aluminum powders to exhibit superior powder characteristics as compared with the CAA, CIGA-ATA, and CIGA-VAL pure aluminum powders. Consequently, the emphasis of the GARS project shifted to a comprehensive investigation of the "clean" aluminum powder in an effort to exploit its potential for new aluminum P/M processing methods. For example, the GARS aluminum powder has a thinner surface oxide film that may enhance the development of metallurgical bonds during aluminum powder consolidation, especially for solid state sintering operations. The contribution of this dissertation to the aluminum P/M industry is to show the strong linkage between gas atomization processing conditions, as-atomized powder characteristics, consolidation behavior, and structure-property relationships of consolidated pure aluminum powders.

CHAPTER 3. EXPERIMENTAL PROCEDURES

To achieve the research goals, four avenues were followed: gas atomization of pure aluminum to produce aluminum metal powder; characterization of the as-atomized aluminum powder; consolidation of the pure aluminum powder; mechanical testing of samples taken from the consolidated specimens. Commercial sources of pure aluminum powder (CAA, CIGA-ATA, and CIGA-VAL) were selected for direct comparative analyses.

Two forms of nomenclature will be used throughout the remainder of this dissertation. First, all mass percentages are reported in weight percent. Second, powder size classifications will be denoted with + and/or - symbols, the former meaning greater than and the latter meaning less than. An example would be -106+75 μm, which would translate to a powder size distribution of powders nominally less than 106 μm but greater then 75 μm.

Gas Atomization Experiments

Atomizer configuration

Aluminum and aluminum alloy powders were produced in a laboratory scale gas atomizer at the Ames Laboratory. The gas atomization system, shown in Figure 3.1, consisted of three components, the melt chamber, the spray chamber, and the collection system. The melt chamber housed an induction heating system using a graphite susceptor around the exterior of a bottom pouring crucible. The aluminum metal charge was placed in the crucible and the metal was heated through the melting temperature to the selected pouring temperature. The first GARS atomization, GARS-2, used a coarse grained, porous, soft-fired alumina crucible. Due to contamination of the melt from the crucible [67], the subsequent GARS atomization runs used a fine grained, dense, hard-fired alumina crucible. The change to the latter type of crucible eliminated the problem of tramp element contamination of the metal.

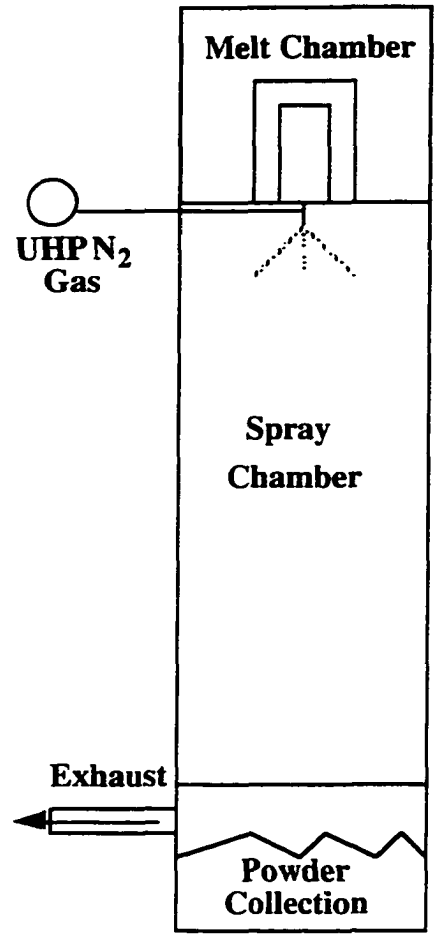

Figure 3.1. Schematic of the gas atomization system used at the Ames Laboratory.

After heating the aluminum charge to the pouring temperature, the stopper rod that plugged the hole in the bottom of the crucible was lifted upwards. The molten aluminum poured down through the bottom of the crucible, passed through the pour tube and exited into the spray chamber. The liquid metal stream entering the spray chamber was immediately disintegrated into molten droplets by high pressure gas flowing through a high pressure gas atomization (HPGA-I) nozzle [68]. The HPGA-I nozzle configuration has a ring of twenty discrete jets focused on the molten metal stream such that close-coupled atomization is achieved. As the molten droplets solidify, they fell down the length of the spray chamber and were carried into the collection box by the gas flow. After atomization, the aluminum powder was removed from the collection box and size classified for characterization.

Atomization parameters

The atomization chamber was evacuated with a roughing pump to a nominal pressure of 50 μm Hg to minimize oxygen and water vapor partial pressures. For the GARS-2 to GARS-6 atomization runs (Table 3.1a) the atomization system was backfilled to atmospheric pressure with high-purity argon gas before heating the metal charge. For the GARS-7 to GARS-9 atomization runs (Table 3.1b) the atomization system was not backfilled until the metal charge was heated to 500°C. At that point in the heating cycle, the entire system was backfilled to atmospheric pressure with UHP (99.998%) nitrogen gas. This gas had a dew point of less than -67°C. The purpose of the vacuum bake-out was to thermally degas the melt chamber, with the intent of further reducing the level of any gaseous impurities, such as oxygen and water, that may have been present in the atmosphere prior to gas atomization.

Table 3.1. Composition, charge mass and pouring temperature of aluminum melts.
a. Heated and melted under UHP argon gas.

	GARS-2	GARS-3	GARS-4	GARS-5	GARS-6
Composition	Al	Al	Al	Al	Al
ChargeMass (g)	250	900	1510	1400	1600
Pouring Temperature	1400°C	1400°C	950°C	1600°C	1200°C

b. Heated under vacuum to 500°C and melted under UHP nitrogen gas.

	GARS-7	GARS-8	GARS-9	Al-Ti-Y
Composition	Al	Al	Al	Al-3Ti-8.2Y
ChargeMass (g)	1533	1760	2100	2200
Pouring Temperature	1400°C	950°C	1200°C	1400°C

The aluminum melts were atomized with UHP nitrogen gas at a pressure of 6.9 MPa. The pouring temperatures, listed in Tables 3.1a and 3.1b, ranged from 950 to 1600°C. Two compositions (Tables 3.1a and 3.1b) were gas atomized for this research, pure aluminum and an aluminum rich ternary alloy with titanium and yttrium additions. The latter alloy was produced in an attempt to enhance the potential of a nitridation reaction between nitrogen atomization gas and the powder particle.

For the GARS-2 and GARS-3 atomization experiments, a high-purity (99.99%)

aluminum ingot from NASA was used as the melt stock. For the remaining GARS atomization experiment, the pure aluminum powder was made from a high-purity aluminum ingot (99.999%) from Alcoa. The melt charge mass for each atomization experiment ranged from 250 grams to 2200 grams (Table 3.1a and 3.1b).

The Al-Ti-Y alloy, listed in Table 3.1b, was made by melting the Alcoa, high-purity aluminum with master alloy buttons of Al-37.2%Ti and Al-91%Y in the melt chamber of the atomizer. The master alloy buttons were made with the Alcoa, high-purity aluminum, 99.80% yttrium from the Ames Laboratory, and 99.99% titanium from Timet. The metal elements were arc melted together to form buttons of the master alloys. The fabrication of the buttons was completed through the Materials Preparation Center at the Ames Laboratory. The purpose for the Al-Ti-Y alloy was an attempt to enhance nitride formation during the gas atomization process between the nitrogen gas and the aluminum alloy. The expectation was additional strong nitride forming elements in the melt would create a nitride phase, resulting with an in-situ metal matrix composite with a stable reinforcement phase.

Metallographic Sample Preparation

Standard metallographic techniques were used to directly observe the microstructures of the as-atomized powder particles and consolidated powder samples. The samples were mounted in epoxy using a vacuum infiltration technique. The samples were first ground by hand on grinding paper, i.e., 240 grit, 320 grit, 400 grit, and 600 grit, respectively. After each paper, the sample was rinsed with water and rotated 90° before grinding on the next paper. After the 600 grit paper, the polishing continued with the 6 μm diamond spray on a rotating wheel until all the scratches from the 600 grit paper were removed. The samples were then placed on an automated polisher using 6 μm and 1 μm diamond paste polishing compounds, respectively. The diamond pastes helped to remove embedded grinding constituents of previous steps from the soft, aluminum matrix. The final polishing step used

a colloidal silica polishing suspension on a Buehler Vibromet 2 with a 10% amplitude setting. The samples remained on the Vibromet for about 3-6 hours until a majority of the scratches had been removed from the previous polishing step.

Powder Characterization of Powders Screened at -45 μm Diameter

Powder shape and size distribution

The shape of the as-atomized powder particles (GARS, CIGA, and CAA) was assessed with the aid of scanning electron microscopy (SEM). To view the loose powders with the SEM, the powders were sprinkled onto conductive carbon tape. Representative micrographs were taken of the loose powders.

A Microtrac II size analyzer provided the size distribution of -45 μm diameter powders. The apparatus uses laser light scattering to measure the size of particles suspended in a fluid medium. For the aluminum powders analyzed, the fluid medium was a mixture of one volume percent polyethylene glycol in deionized water. The polyethylene glycol, a surfactant, helped to dispersion agglomerated powder particles into discrete powder particles for more accurate powder size measurements.

Pycnometry measurements

The as-atomized aluminum powder densities were measured with pycnometry [69], a gas adsorption method used to measure the true density of a powder sample. Pycnometry accounts for any internal porosity that may be present inside the powder particles as a result of the gas atomization process. For this research, a Quantachrome MVP-1 Multipycnometer was used and operated according to the manufacturer's instructions listed in the operations manual. The adsorbate gas was ultra-high purity, zero grade (99.999%), helium gas with a dew point of less than -68°C.

Differential thermal analysis (DTA)

Differential thermal analysis of the as-atomized powders had three intentions: to observe indirectly if the oxide surface film had been destroyed or remained in tact after heating above the melting point of aluminum; to measure the phase transformation temperatures in the Al-Ti-Y alloy and an Al-4.4%Cu-1.5%Mg alloy; to detect any melting point depression in the pure aluminum powders due to impurity elements. The analyses were done with a Perkin-Elmer DTA 7. Before measurements were recorded, the system was purged with argon. The samples were contained in alumina sample holders with heating and cooling rates of 10°C per minute. The pure aluminum, the Al-Cu-Mg alloy and the Al-Ti-Y alloy samples were heated to 700°C, 700°C, and 1200°C, respectively. The analyzed samples were saved for post-analysis examination.

The Al-Cu-Mg alloy powder was manufactured by Valimet using a CIGA process with helium plus a maximum of two volume percent oxygen. The Al-Cu-Mg alloy powder was included in this research to observe the effect of magnesium on the vacuum hot degassing process in an aluminum alloy powder, as compared with pure aluminum powder. A DTA scan and quadrupole mass spectroscopic analyses were conducted and compared to draw some conclusions.

Bulk powder chemistry

The bulk chemical content was measured with inductively coupled plasma (ICP) using an Applied Research Laboratories ARL 3410 ICP. The metallic elements sought in the pure aluminum samples were silicon, iron, copper, magnesium. These metals are commonly the highest percentage metallic impurities in bulk aluminum. Any abnormally high contents could then be detected with a DTA scan as a freezing point depression. The analysis of the Al-Ti-Y alloy included the same list of elements as above, as well as yttrium and titanium. The oxygen and nitrogen contents of similar powders were measured with inert gas fusion

(IGF) using a LECO TC-436 oxygen and nitrogen analyzer. The carbon content was measured by a combustion technique using a Horiba EMIA-520 carbon and sulfur analyzer. The hydrogen contents of the powders were measured by a vacuum extraction technique [31], using instrumentation designed and built at the Ames Laboratory [30].

Auger electron spectroscopy (AES)

A Perkin-Elmer PHI 660 scanning Auger microscope was used to measure the oxygen concentration profile inwards from the powder surface of the as-atomized powders. Argon ions were used to sputter the surfaces of the powders during depth profiling. For the pure aluminum powders, other depth profiles were made at the same time for the aluminum, nitrogen, and carbon concentrations. For the alloy powders, the respective major alloy additions were added to the profiles, copper and magnesium in the Al-4.4Cu-1.5Mg alloy and titanium and yttrium in the Al-Ti-Y alloy.

For the analysis of GARS-2 powder, the powder was pressed into indium foil to hold the powder in place. During the analysis, the indium was sputtered and redeposited onto the powder particles, creating inaccurate depth profiles. To eliminate the need for indium foil, a decision was made to make a powder sample that in effect was its own substrate. The powder was cold isostatically pressed (CIP) into a rod shape, nominally 5 cm long, using 6.35 mm diameter rubber bags and pressures of 103.5 MPa to 138 MPa. The first attempts failed to make straight rods. In these cases, the powder would CIP into several small pellets. Success was achieved by placing the bagged powder samples securely into stainless steel sheaths slightly larger in diameter than a CIP bag diameter and maintaining the samples in an upright position during CIP. The bags were secured in the sheaths by folding the ends of the bag over the edge of the sheath and firmly wrapping electrical tape over the bag end and around the sheath. A majority of the samples prepared this way were single straight rods.

A section of a CIP rod greater than 16 mm was placed into the Auger and fractured

under vacuum to provide a "fresh" surface. Typical analyses consisted of six powder particles, two in the diameter range of 5 to 10 μm, two in the diameter range of 20 to 25 μm diameter, and two in the diameter range of 45 to 50 μm. Powder samples prepared in this fashion eliminated the need to handle loose powders and reduced redeposition problems.

Quadrupole mass spectroscopy (QMS)

The QMS system used a 100C Precision Mass Analyzer, manufactured by Uthe Technology International, to characterize the pure aluminum powders in this study. The gas species of interest were water and hydrogen. The need arose to design and to build a sample chamber capable of minimizing the introduction of atmospheric water and hydrogen into the sample chamber. Figure 3.2 shows the final design and set-up of the sample chamber was connected to the QMS chamber by means of a stainless steel o-ring sealed fitting, Ultra-Torr adapter, made by Cajon. The sample chamber consists of a quartz holding chamber and a quartz furnace crucible connected by the same type of union tee. A type K thermocouple was inserted in the leg of the union tee fitting to approximately measure the temperature of the sample during the analysis.

The data generated from these experiments, i.e., the sample temperature (°C), the sampling time interval (minutes), system vacuum pressure (Torr) and the intensities of mass currents (amps) of the selected atomic mass units (amu), were collected at 0.25 minute intervals with the aid of a computer. The data acquisition program was written in BASIC by Jim Anderegg, an assistant scientist at the Ames Laboratory. The amu's selected were 2, 17 and 18 that correspond to hydrogen gas (H_2), hydroxide (OH) and water (H_2O), respectively.

The GARS, CIGA-ATA, CIGA-VAL, and CAA aluminum powders were analyzed by QMS. All aluminum powders samples were densified by CIP at 138 MPa and retained in hermetically sealed CIP bags. The approximate green density of the CIP samples was 85-90% of theoretical density, according to the compressibility curve in the ASM handbook

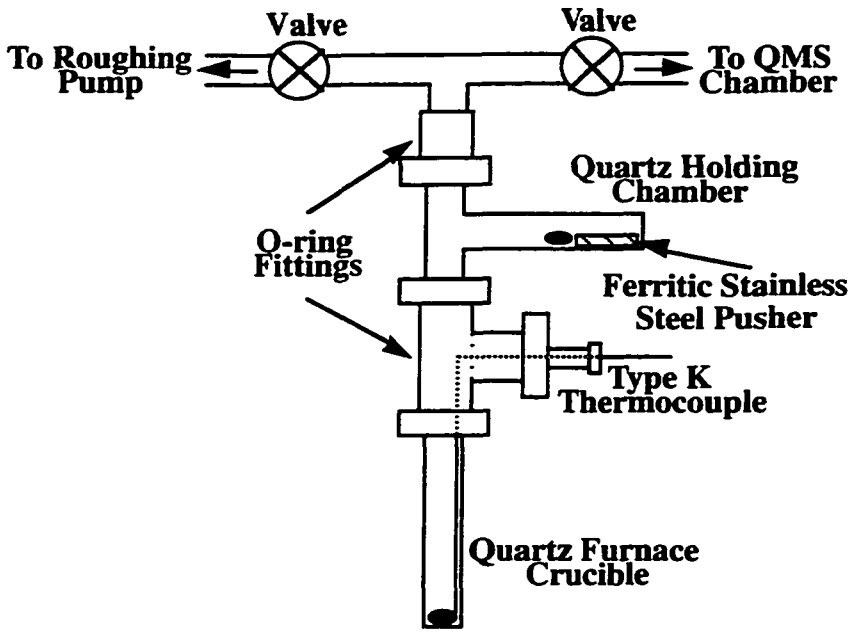

Figure 3.2. Schematic of the QMS sample chamber used for this research.

[43]. Before each QMS experiment, a piece of a CIP sample was weighed and placed in the holding chamber. The sample weights were between 72 and 185 mg. Small samples were necessary to minimize saturation of the QMS instrumentation.

The sample chamber was then evacuated with a roughing pump to $6x10^{-3}$ Torr. During this evacuation, the furnace crucible was heated with a hand held heat gun until the thermocouple registered 120°C. This heating assisted in the removal of any adsorbed water on the crucible walls. After the heated outgassing of the crucible, the furnace crucible cooled to room temperature, and the rough pump valve was closed. The valve between the sample chamber and the QMS chamber was opened, exposing the sample chamber to an ultimate vacuum in the range of $2x10^{-8}$ Torr. The pumping speed of the turbo-pump was 200 liters per minute. The sample chamber was exposed to this vacuum level for about two hours. During this ambient temperature ultra-high vacuum (UHV) degassing, the sample chamber was monitored with the QMS to measure the relative hydrogen and water levels.

After a two hour UHV degassing, the sample was moved, with a ferritic stainless steel pusher, from inside the holding chamber into the furnace crucible, a drop of about 18 cm.

The pusher was moved by the motion of a magnet held against the outside wall of the holding chamber without breaking vacuum. Before starting the furnace, the water and hydrogen levels were measured with the QMS for two minutes. The average of these measured intensities were recorded as the initial intensity (I_o). After the two minute hold, the furnace was turned on and heated at a specified rate from room temperature to 635°C with an automated, proportioning, Eurotherm 808, controller.

Three QMS experiments were done to accurately interpret and validate the results of this analytical technique. One experiment measured the gas evolution due only to the furnace crucible walls and the sheathed thermocouple inside the evacuated crucible, designated as "empty", i.e., no aluminum sample. Another experiment tested a pure hydrated alumina powder sample, $Al_2O_3 \cdot 3H_2O$ (99.6%), grade C-33 from Alcoa, to record the relative positions of the water and hydrogen peaks. In this case, the powders were CIP consolidated at 449 MPa in 6.35 mm diameter rubber bags. A small sample, 0.75 mg, was tested to prevent water saturation of the QMS instrumentation. The heating rate for this experiment was 5°C per minute. The third experiment recorded the relative quantities of water and hydrogen evolving from a sample of the Alcoa 99.999% pure aluminum ingot used as the melt stock for the GARS pure aluminum powders.

The results of the aluminum powders stimulated two more sets of experiments in an effort to better understand and characterize the QMS analysis technique. One test considered how changes in the heating rate, at constant sample density, would affect the water and hydrogen intensities. The specimen was the CAA aluminum powder CIP consolidated at a density of 92.3% of the pycnometry density, heated at three rates, 2.5°C per minute, 5°C per minute, and 10°C per minute. This powder was selected because of the definitive hydrogen peaks in the QMS spectra.

The second examination maintained the heating rate constant, 10°C per minute, and varied the CIP pressure or green density of the CIGA-ATA CIP powders, again, to observe

any changes in the relative intensity of the water and hydrogen profiles. This powder was selected without any established criteria other than its availability and abundance. The densities of these samples, with respect to the pycnometry density, were 71.8%, 83.2%, 86.7%, and 91.7% for CIP pressures of 5 ksi, 15 ksi, 20 ksi, and 30 ksi, respectively.

X-ray diffraction (XRD) of Al-Ti-Y powder

Samples of the Al-Ti-Y alloy powder, at various conditions of heat treatment, were analyzed with a Philips Automatic Powder Diffraction, Model 1729, using copper Kα radiation and a scan rate of 0.05°/sec over the range of 15 to 120 degrees two-theta. The phases present in the as-atomized powder were not readily identifiable. To assist with the phase identification, samples of the as-atomized powders were heat treated, one sample at 300°C for 1.25 hours and another at 500°C for 3 hours, to form equilibrium phases within the powder particles. The phases in the heat treated powders were identified using Joint Committee for Powder Diffraction Standards (JCPDS) cards (Table 3.2) and the characteristic peaks were labeled accordingly. The peaks on the XRD trace of the as-atomized powder were then identified by overlaying the as-atomized powder scan onto the heat treated XRD trace. Before heat treating, the samples were encapsulated in quartz tubes with a cover gas of argon at a partial pressure of 254 Torr. The encapsulation tubes were then placed in an air furnace for the scheduled time and temperature. After heat treating, the hot samples were removed from the furnace and air cooled.

Table 3.2. JCPDS cards used for phase identification in Al-Ti-Y powder alloy.

Compound	JCPDS card number
Al	04-0787
Al_3Ti	37-1449
β-Al_3Y	20-0067
Al_2Y	29-0103
$AlYO_3$	33-0041
$Al_5Y_3O_{12}$	33-0040

Transmission electron spectroscopy (TEM)

TEM was used as a complementary tool to AES to validate the oxide thickness measurements as well as determine the structure of the native surface oxide film on pure aluminum powders. Several methods of TEM sample preparation were employed to make foils to show the structure and thickness of the oxide film on aluminum powders. In considering the type of sample needed to accomplish these objectives, a fully dense sample was deemed the best solution. The foil sample needed to have sufficient strength in very thin sections, <100 μm. Also, the consolidation process and sample preparation had to minimize alteration of the oxide thickness and the native oxide structure, respectively. The powders examined were the GARS-8 and the CAA aluminum powders.

The consolidation sequence began with cold isostatically pressing (CIP) the powders at 138 MPa in 2.54 cm diameter rubber CIP bags. The resulting green density was about 90% of the pycnometry density. The samples were then machined to fit inside a cylindrical stainless steel can with a degassing vent pipe welded to the cap of the can, as shown in Figure 3.3. The samples were then degassed in an evacuated electron beam melting (EBM) chamber. The degassing was conducted at room temperature under a vacuum of better than $1x10^{-6}$ Torr for 24 hours . After degassing and while the sample can was in the EBM chamber, the vent pipe was welded close. The can was then hot isostatic pressed (HIP) at 310 MPa and 300°C for 4 hours. The low HIP temperature was chosen to minimize any oxide phase transformation from an amorphous structure to a crystalline structure which van Beek and Mittemeijer [70] have observed to occur in the temperature range of 400°C to 450°C. A disadvantage of this sample preparation route is the original oxide film thickness may distort due to the powder deformation.

After the HIP cycle, the stainless steel can was removed and 0.8 mm thick disks were cut from the samples. The disks were mechanically ground parallel to a nominal thickness of 0.1 mm on 600 grit grinding paper. Three millimeter diameter foils were mechanically

Figure 3.3. HIP can geometry used for consolidating CIP aluminum powders.

punched from the 0.1 mm thick disks. The TEM foils were dimpled on both sides using a VCR 500 series dimpler. The dimpling procedure was interrupted prior to perforation of the foil.

Foil perforation was achieved using a Fischione twin-jet electrochemical polisher. The dimpling of the foils prior to the electrochemical thinning minimized the time in the etchant solution. The electrolytic thinning conditions were adapted from the procedure described by Conserva and Fiorini [71]. A 3:1 solution of methanol and nitric acid was used as the electrochemical etchant. The solution was cooled to a nominal temperature of -40°C. The etching solution was cooled with liquid nitrogen that was siphoned from a cryogenic dewar and circulated through a cooling coil with the use of a roughing pump. The sample current was set at 60 mA and the corresponding voltage was 40 volts d.c. The time for perforation ranged from two minutes to 4.5 minutes. To minimize oxidation of the perforated samples, they were individually stored in small, capped vials filled with methanol. A Philips CM-30 STEM, set at an excitation voltage of 300kV, was used to measure at the oxide thickness as well as attempt to determine the structure of the surface oxide film.

Powder oxidation

Powder samples of the GARS-7, GARS-8, and GARS-9 as-atomized aluminum powders were collected for a series of post-atomization oxidation experiments. The powders were sieved in either a glove bag or glove box under an inert atmosphere and placed in glass vials. The uncapped vials and aluminum powders were then exposed to air with varying amounts of humidity. The exposure times were 0.3 hours, 3 hours, 10 hours, 30 hours, 100 hours, 300 hours, 1000 hours, and 3000 hours. The powder samples exposed for 0.3 hours are designated as the unexposed state. After the designated time of exposure, the sample vials were capped and electrical tape was wrapped around the edge of the cap and vial to ensure no further exposure. The capped vials were stored in a vacuum dessicator box until the bulk oxygen content was measured.

The GARS-7 and GARS-8 powders were exposed to air between the months of June and September, in Ames, Iowa, where the indoor humidity ranged from 45% to 50% [72]. The GARS-9 powder collected was evenly divided for two air exposure experiments. One exposure condition was ambient air during the months of December and May with humidity levels between 15% and 25% [72]. The second set of samples was placed in a vacuum dessicator box during the same time period. During this exposure, the dessicator box was filled with a flowing gas of UHP dry air. This experiment was designed to maintain a clean and fresh atmosphere throughout the exposure.

The Al-Ti-Y alloy powder was also exposed to ambient air for similar length of times, from the unexposed state to 1000 hours, at nominal temperatures of 25°C, 162°C, and 300°C. The powders exposed at elevated temperatures were placed in quartz tubes closed at one end. The tubes and powders were placed upright in a vertical tube furnace for the specified periods of time. The experiments were conducted indoors between the months of February and May in Ames, Iowa. The relative humidity levels during this time were in the range of 15% to 25%.

Powder explosibility

The MEC of the pure aluminum powders produced for this research were measured with a standard explosibility test chamber as described in references [35, 73] at facilities operated by Alcoa in Pittsburgh, PA. The GARS-3, GARS-4, GARS-5, GARS-6 aluminum powders provided preliminary results of the explosibility hazard of samples sieved in air and stored under an inert atmosphere. The time from atomization to the explosibility testing was not accurately measured, nor was the oxide film growth controlled.

A more thorough experiment was designed to test the dependence of surface area and oxide film thickness on the explosibility of pure aluminum powders. The as-atomized GARS-9 powder was sieved in a glove box filled with an argon atmosphere into two size ranges, -106+75 μm and -38 μm. To grow the as-atomized oxide film, the powder samples were exposed to ambient air for 10, 100 and 1000 hours, at either room temperature, nominally 25°C, or 300°C (Table 3.3). The 300°C exposure was completed in a manner

Table 3.3. Experimental matrix to evaluate the dependence of oxide film thickness and surface area on the MEC of pure aluminum powders.

Sample Indentification	Powder Size (μm)	Exposure Time (Hours)	Exposure Temperature (°C)
-38/10/25	-38	10	25
-38/10/300	-38	10	300
-106+75/10/25	-106+75	10	25
-106+75/10/300	-106+75	10	300
-38/100/25	-38	100	25
-38/100/300	-38	100	300
-106+75/100/25	-106+75	100	25
-106+75/100/300	-106+75	100	300
-38/1000/25	-38	1000	25
-38/1000/300	-38	1000	300
-106+75/1000/25	-106+75	1000	25
-106+75/1000/300	-106+75	1000	300

similar to the thermal oxidation of the Al-Ti-Y powder. At the end of the defined exposure time, several powder characteristics were measured, namely, bulk oxygen content, AES oxide thickness, particle size distribution and MEC. The -38/1000/300 sample was the only 1000 hour exposure sample tested for MEC due to limited financial resources.

Powder Consolidation

Consolidation sequence

Due to limited powder quantities, only small consolidated samples could be fabricated. The consolidation of the pure aluminum powders followed a modified consolidation route (Figure 3.4a) [67,74], typically used for aerospace aluminum powder components (Figure 3.4b) [1]. The consolidation experiments used the GARS-4 aluminum powders and CAA pure aluminum powder from Alcoa. Rubber CIP bags, 2.54 cm diameter, were filled with -45 μm powder to a nominal height of 8 cm. Following the CIP at 138 MPa, the CIP samples were machined to fit into stainless steel cans (Figure 3.3) with dimensions of 1.90 cm diameter, 5 cm tall and a wall thickness of 0.055 cm. Prior to welding the can closed, a vent pipe for the subsequent outgassing treatment was installed on the top of the can.

Two degassing procedures, vacuum hot degassing (VHD) and vacuum cold degassing (VCD), were conducted prior to HIP of the aluminum powders. The VHD treatment consisted of heating the sample and HIP can to a temperature of 550°C under a vacuum of $1x10^{-6}$ to $1x10^{-7}$ Torr for four hours. After the VHD, the vacuum furnace was backfilled with UHP argon gas. The sample was removed from the furnace and placed in an argon filled zip-lock bag. The sample was immediately transported to an electron beam melting chamber and evacuated again at room temperature. After evacuating the sample overnight, about 16 hours, to a similar vacuum level as before, the vent pipe was welded shut. The VCD approach involved a room temperature evacuation of the powder sample and can in the electron beam melter over a period of about 16 hours at a vacuum level ranging from $1x10^{-6}$ to $1x10^{-7}$ Torr. The vent pipe was then welded shut. All the sealed evacuated cans were then HIP at 550°C and 310 MPa for four hours. Sections of these consolidated samples were prepared for metallographic examination. The remaining pieces were fabricated into mechanical property test specimens. Specimens of the GARS-4 and CAA, each consolidated

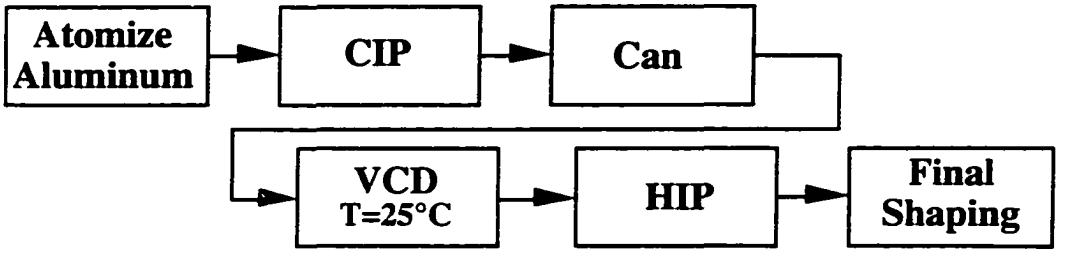

a. Modified consolidation sequence for aluminum powders used for this research.

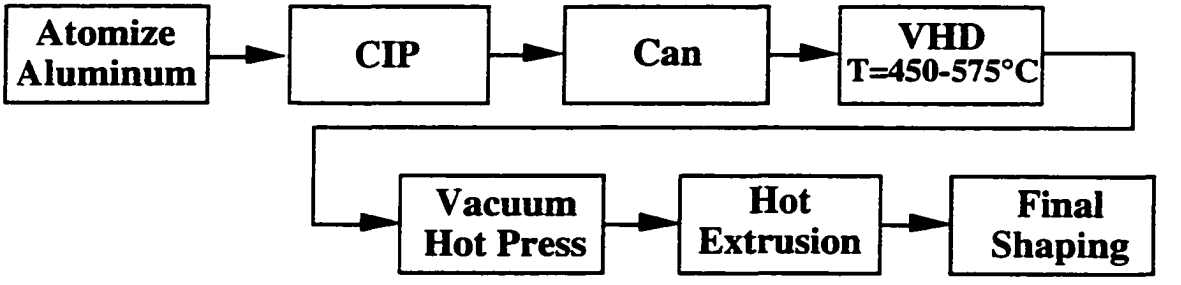

b. Conventional consolidation sequence for aluminum powders used in aerospace applications as described in [1].

Figure 3.4. Consolidation sequences of aluminum powder.

by either the CIP-VHD-HIP or the CIP-VCD-HIP processing route, were evaluated with QMS.

The consolidated sample densities were measured by hydrostatic immersion also referred to as Archimedes method. The density, ρ (g/cm^3), of the sample is determined according to equation 3.1, where M_{dry} (grams) is the weight of the sample in air and M_{wet} (grams) is the weight of the sample measured in a fluid of known specific gravity, SG_{fluid} (g/cm^3). Because some samples were porous, all the surfaces of the samples were lightly sprayed with a polyurethane varnish to prevent water infiltration into the pore network of the consolidated powder product.

$$\rho = \frac{M_{dry}}{\left(M_{dry} - M_{wet}\right)} * SG_{fluid} \tag{3.1}$$

Post consolidation heat treatment

To test the applicability of the VCD procedure to aluminum P/M components used at elevated temperatures, sections of the GARS-4, CIGA-ATA, and CAA CIP-VCD-HIP samples were heat treated at 300°C for one hour. A similar experiment was conducted on another section of the CAA CIP-VCD-HIP sample heat treated at 550°C for one hour. The CIP-VCD-HIP samples were encapsulated in quartz tubes under an argon partial pressure of 10 inches of Hg. The tubes were placed in a muffle air furnace at the appropriate temperature and held for one hour. Sections of the heat treated samples were prepared for mechanical property testing and for QMS evaluation. Both these examinations made direct comparisons between the non-heat treated and the heat treated samples.

Mechanical Property Measurements

Punch testing

The small size of the consolidated samples and the need to maximize the statistical results of the mechanical properties required the use a small punch test. Punch testing [75] is a method for measuring a select group of mechanical properties from a load versus deflection curve. The raw data was initially recorded on x-y chart recorder paper. Later, a computer collected the data for faster and easier data analysis. The measurable properties from the raw data are coupon thickness, t_o (mm), yield load, P_{yield} (N), maximum load, P_{max} (N), fracture energy in E_f (N·mm), and fracture deflection, δ_f (mm). With the aid of empirical equations 3.2 and 3.3, yield stress, σ_{yield} (MPa), and fracture strain, ε_f (mm/mm) were calculated, respectively.

Figure 3.5 is used for the following description to show how the punch test data was determined. The yield load was determined as the intersection of the two tangents shown on the punch test curve. The maximum load was defined at the point were the slope of the curve was zero. For direct relative comparisons, the deflection at maximum load was arbitrarily

$$\sigma_{yield}(MPa) = 360\left(\frac{P_{yield}}{t_o^2}\right)(kN/mm^2) \tag{3.2}$$

$$\varepsilon_{qf} = 0.12\left(\frac{\delta_f}{t_o}\right)^{1.72}(mm/mm) \tag{3.3}$$

chosen as the point of fracture deflection. The fracture energy value required a measurement of the area under the load-deflection curve, as shaded in Figure 3.5.

The CIP-VHD-HIP, CIP-VCD-HIP and CIP-VCD-HIP-heat treated samples were cut transversely into 0.8 mm thick disks and then mechanically ground with 600 grit grinding paper to a nominal 0.6 mm thickness. Each disk yielded three, 6 mm diameter test coupons that were cut using a plunging electrodischarge machining (EDM) technique. The test coupons were ground to a nominal thickness (t_o) of 0.500±0.010 mm on 1500 grit grinding paper. The 6 mm diameter coupons were tested with a punch speed of 0.127 cm per minute.

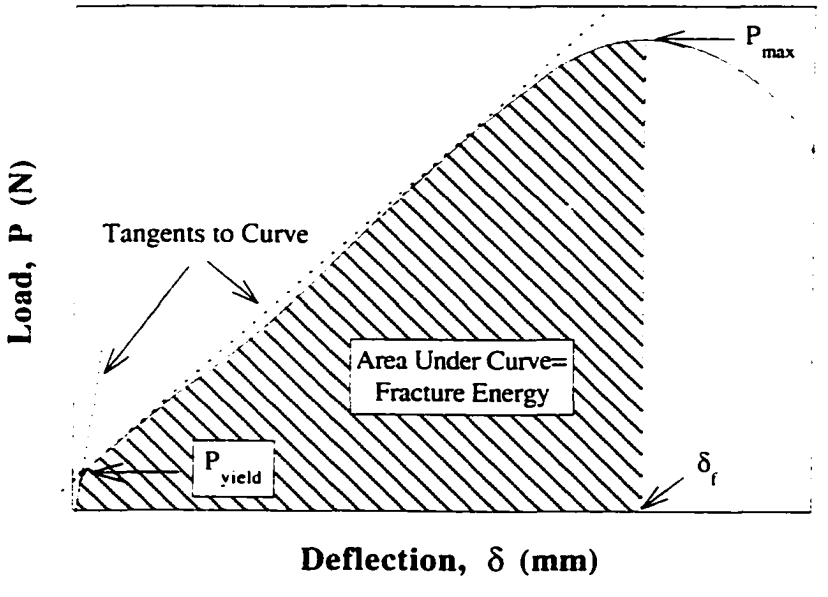

Figure 3.5. Example of the punch test raw data as recorded on a load-deflection curve.

CHAPTER 4. EXPERIMENTAL RESULTS

Powder Characterization of -45 μm Diameter As-atomized Powders

Shape and size distribution

The shape of the aluminum powders is idiosyncratic with the gas atomization method used to manufacture the aluminum powders. To illustrate these idiosyncrasies of the CAA, CIGA-ATA and GARS atomization processes, SEM micrographs were taken of the as-atomized powder particle shapes. The shape of the GARS aluminum powder is spherical (Figure 4.1) with some satellites, i.e., small powders attached to larger particles and agglomerations of small particles. The CIGA-ATA powders (Figure 4.2) range from spherical to irregular shapes. The CAA powders (Figure 4.3) have a ligmental or irregular shape.

Table 4.1 shows a list of parameters describing the size distributions of the GARS,

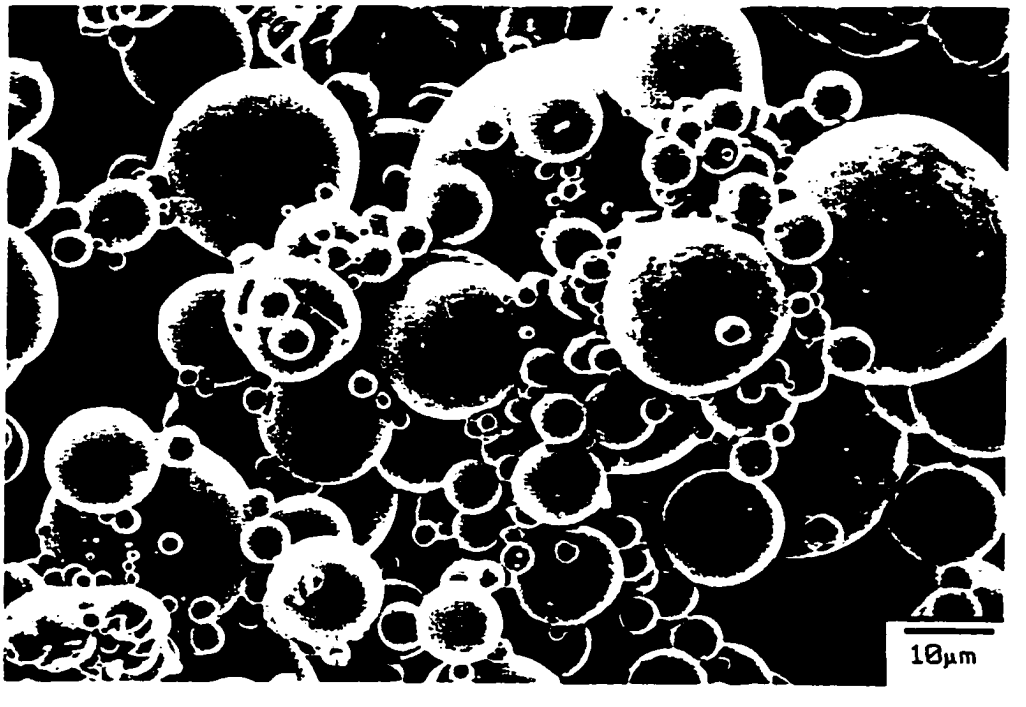

Figure 4.1. SEM photograph of GARS aluminum powder.

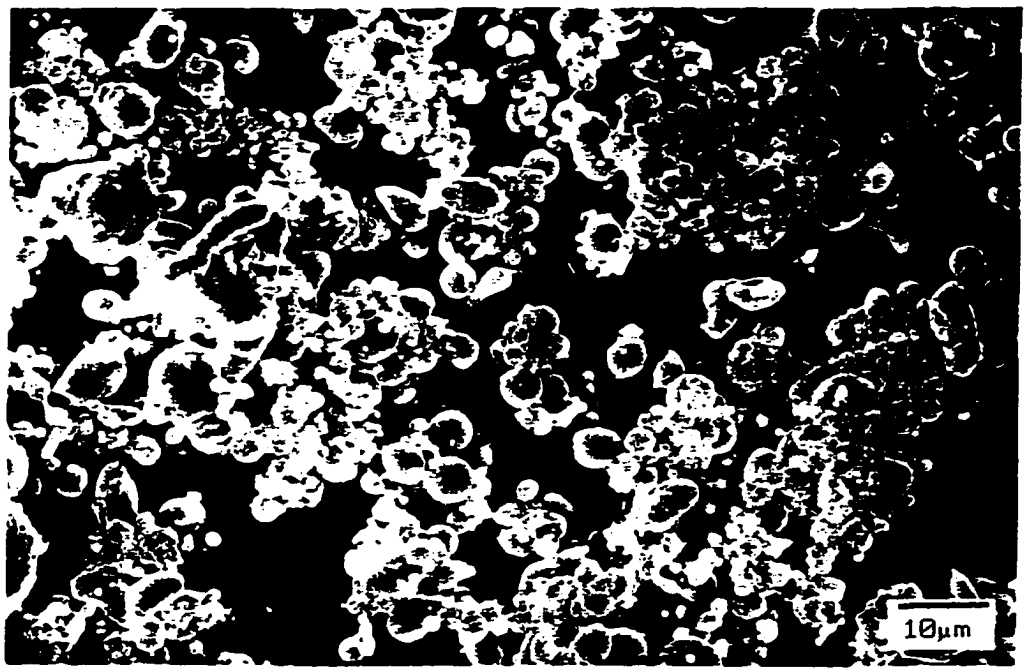

Figure 4.2. SEM micrograph of the as-atomized CIGA-ATA pure aluminum powder.

Figure 4.3. SEM micrograph of the as-atomized CAA aluminum powder.

CIGA-ATA, and CAA pure aluminum powders. The same table shows the size distribution of the Al-Ti-Y alloy powders manufactured with the GARS technology. The columns are the percentile points, d_{16}, d_{50}, and d_{84}, which indicates the measured volume percent of powder which is smaller than the indicated size. The CSA column is the calculated surface area as determined with the Micro Trac II software. Figure 4.4 shows pictorially the size distribution of the GARS-4, CIGA-ATA, CIGA-VAL, and CAA aluminum powders. The GARS-4 aluminum powder, a representative of the other GARS powders, was selected for this figure, because this powder was used in the consolidation and QMS experiments for comparison with the CIGA-ATA and CAA powders.

Table 4.1. Particle size distribution data from a Microtrac II particle size analyzer.

Powder Type	d_{16} (μm)	d_{50} (μm)	d_{84} (μm)	CSA (m^2/cm^3)
GARS-3	12.15	24.16	41.87	0.330
GARS-4	10.66	23.45	44.94	0.356
GARS-5	10.85	21.40	39.38	0.364
GARS-6	12.01	25.43	46.58	0.325
GARS-7	14.25	27.89	47.37	0.280
GARS-8	12.28	26.50	46.50	0.328
GARS-9	12.23	24.29	39.95	0.343
Al-Ti-Y	10.20	20.43	35.14	0.402
CIGA-VAL	10.11	21.79	41.40	0.351
CAA	12.08	22.16	39.23	0.331
CIGA-ATA	2.17	4.99	11.09	1.676

The size distribution data for the CAA aluminum powder is erroneous due to the irregular shape of the powder as observed with the SEM micrograph in Figure 4.3. The algorithm used by the computer software of the Micro Trac II instrumentation uses the assumption that all powder particles passing through the laser light are spherical. The contribution of each irregular shaped particle to the overall light scattering pattern depends greatly on the orientation of the irregular shaped particle with respect to the laser beam [76]. Kaye and Trottier continue to explain that irregular shaped particles presented to the laser from the broadest side, in effect, distorts the coarse end of the size distribution, making the

size distribution appear more coarse. On the other hand, irregular shaped particles having a parallel orientation to the incident beam has the effect of overestimating the quantity of fines in the size distribution. For irregular shape powder particles, the Micro Trac II assigns an apparent spherical powder size based on the "diameter" of the projected area of the powder particle on the detector of the Micro Trac II instrumentation.

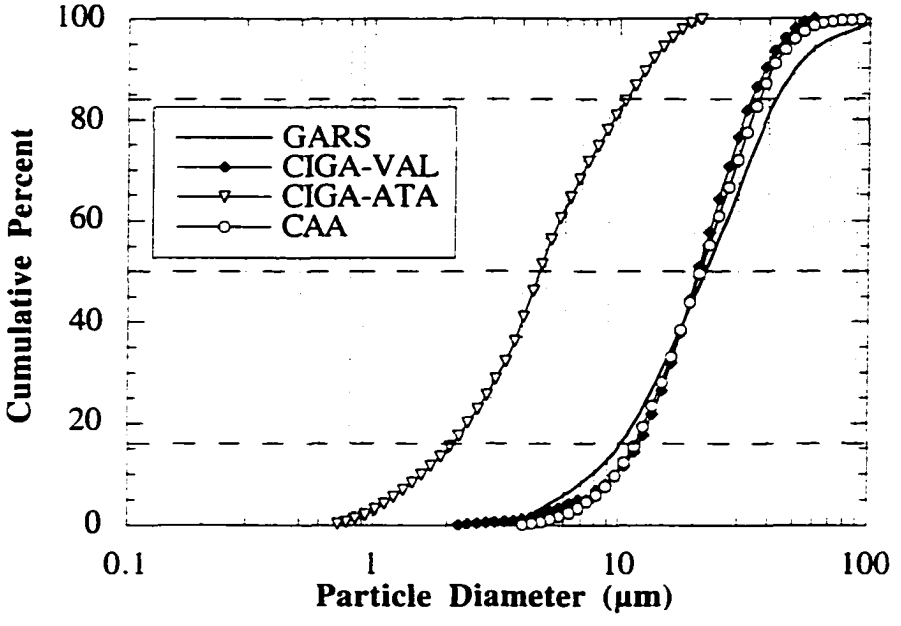

Figure 4.4. Cumulative size distributions of the GARS-4, CIGA-ATA, CIGA-VAL, and CAA aluminum powders.

Density measurements and specific surface area

The powder density and specific surface area measurements are two more characterization methods to describe the aluminum powders. The powder density, measured with pycnometry, was determined to assess the theoretical density of the aluminum powders listed in Table 4.2. The standard deviation of the density values for the all the aluminum powders is less than 0.5% of the measured value. The measured density values of the pure aluminum powders are slightly different than the theoretical density of aluminum, 2.70 grams per cubic centimeter. The difference is possibly due to trace element chemical variations within the powders. Another possible reason for the difference are errors in the pycnometry

calibration values which are used for the calculation of the pycnometry density.

Table 4.2 also lists the specific surface areas of the powders. The specific surface areas were determined from either BET surface area measurements or calculated from the particle size distribution data and the pycnometry density. The calculated specific surface area, in this case, is the quotient of the CSA column in Table 4.1 divided by the respective pycnometry density value in Table 4.2.

Table 4.2. Pycnometry density and specific surface areas of aluminum powders.

Powder	Pycnometry Density (g/cm^3)	Surface Area (m^2/g)	Determination of Surface Area
GARS-3	2.652±0.007	0.122	Calculated
GARS-4	2.641±0.013	0.131	Calculated
GARS-5	2.655±0.008	0.134	Calculated
GARS-6	2.693±0.005	0.120	Calculated
GARS-7	2.677±0.007	0.103	Calculated
GARS-8	2.670±0.005	0.121	Calculated
GARS-9	2.700±0.008	0.127	Calculated
Al-Ti-Y	2.810±0.009	0.143	Calculated
CIGA-VAL	2.659±0.006	0.132	Calculated
CAA	2.699±0.004	0.680	BET
CIGA-ATA	2.667±0.005	0.619	BET

Pure aluminum powder analytical characterization

Bulk chemistry

Bulk chemistry measurements provide chemical information about the aluminum powders which is relevant to three areas of aluminum powder processing, i.e., atomization, consolidation, and mechanical property data interpretations. For this research, bulk chemical measurements were made of the GARS melt stock before atomization and the as-atomized GARS aluminum powders after atomization. These measurements help identify problems related to reactions between the molten aluminum and the refractory materials in contact with the liquid aluminum. Consolidation procedures should also be properly selected as the chemistry of the aluminum powders would affect elevated temperature processes. For example, elevated levels of trace elements may combine with the aluminum to form low

melting point eutectic phases which could distort a consolidated component, creating a scrap work piece and decreasing the component output yield. Another benefit of a bulk chemical analysis is to assist with a proper interpretation of a chemical dependent mechanical property data, such as yield stress.

The melt stock bulk chemistries are summarized in Table 4.3. The NASA aluminum was measured at the Ames Laboratory with Laser Ion Mass Spectroscopy (LIMS) and the Alcoa ingot was measured at Alcoa using Gas Discharge Mass Spectroscopy (GDMS). Both methods of chemical analysis scan the entire period table of the elements and, hence, are semi-quantitative. In other words, the data is a first approximation of the actual chemistry. Note, the GARS-2 and GARS-3 powders were produced from the NASA aluminum ingot and the remaining GARS powders were manufactured with the Alcoa aluminum ingot.

Table 4.3. Bulk chemical measurements of melt stock for GARS aluminum powders. The NASA aluminum was measure by LIMS and the Alcoa was measured by GDMS.

Element	Al (ppmw)	Si (ppmw)	Fe (ppmw)	Mg (ppmw)	Cu (ppmw)	C (ppmw)	O (ppmw)	N (ppmw)
NASA	Balance	3.6	7.0	0.3	20	3.0	35	<1
Alcoa	Balance	4.3	0.2	0.6	0.4	0.4	6	1.9

Table 4.4 shows the bulk chemistries of the as-atomized GARS aluminum powders as measured with ICP-AES. ICP-AES is a quantitative measure of the aluminum powders, because the method only detects operator selected elements. The GARS-2 aluminum powder has a significantly different chemistry than the NASA melt stock. This is due to the molten aluminum reacting with the soft-fired mullite Norton crucible prior to gas atomization. The aluminum melt stock for the subsequent GARS atomization runs was melted in hard-fired high-purity aluminum crucibles. As a result, the elemental contamination of these powders were significantly less than for the GARS-2 powder and are in the neighborhood of the Alcoa ingot melt stock.

Table 4.4. ICP-AES and IGF measurements of as-atomized pure aluminum powders.

Element	Al	Si (wt. %)	Fe (wt. %)	Mg (wt. %)	Cu (wt. %)	C (ppmw)	O (ppmw)	N (ppmw)
GARS-2	Balance	3.8	0.835	----	----	1150	1530	40
GARS-3	Balance	<0.008	0.032	<0.007	0.056	66	965	10
GARS-4	Balance	<0.002	<0.005	<0.002	<0.002	25	761	3
GARS-5	Balance	<0.020	0.020	<0.0002	<0.002	79	1060	6
GARS-6	Balance	0.006	0.0106	0.0002	<0.03	58	595	2
GARS-7	Balance	<0.05	0.55	<0.02	<0.02	76	550	10
GARS-8	Balance	0.013	0.011	0.0002	<0.02	37	598	1
GARS-9	Balance	0.0046	0.0026	0.0002	<0.03	----	595	4
CAA	Balance	0.012	0.0065	0.0004	<0.02	141	3312	28
CIGA-ATA	Balance	0.11	0.17	<0.004	<0.005	84	5446	52

Differential thermal analysis (DTA)

The DTA results for this research show the melting point depression of the pure aluminum powder due to the presence of trace elements that may or may not be measurable with ICP-AES. Also, DTA is an analytical method to complement phase identification and reaction chemistries of the aluminum alloy powders.

A DTA scan of the Alcoa pure aluminum ingot (Figure 4.5) shows the heating and cooling curves at 10°C per minute. The heating curve has a single on-set temperature of 660.2°C which corresponds well with the published value of 660°C. From the calibration with a K_2SO_4 standard at 10°C per minute, the measured on-set value is reproducible to within 1.4°C. A representative DTA trace of the GARS aluminum powders (Figure 4.6) illustrates the reactions observed in the during heating and cooling cycles. The heating curve has two on-set temperatures characteristic of a eutectic phase transformation in addition to the expected melting endotherm of pure aluminum. The eutectic reaction temperature identified on the DTA traces is similar to the published aluminum-iron eutectic on the aluminum rich side of the aluminum-iron phase diagram [77] at 98.1 weight percent aluminum and 655°C. The GARS-3 and GARS-5 powders were the only samples to have only one measurable on-set temperature upon heating. All the cooling curves have only one on-set temperature with no more than 9°C of undercooling. Overall, these DTA scans

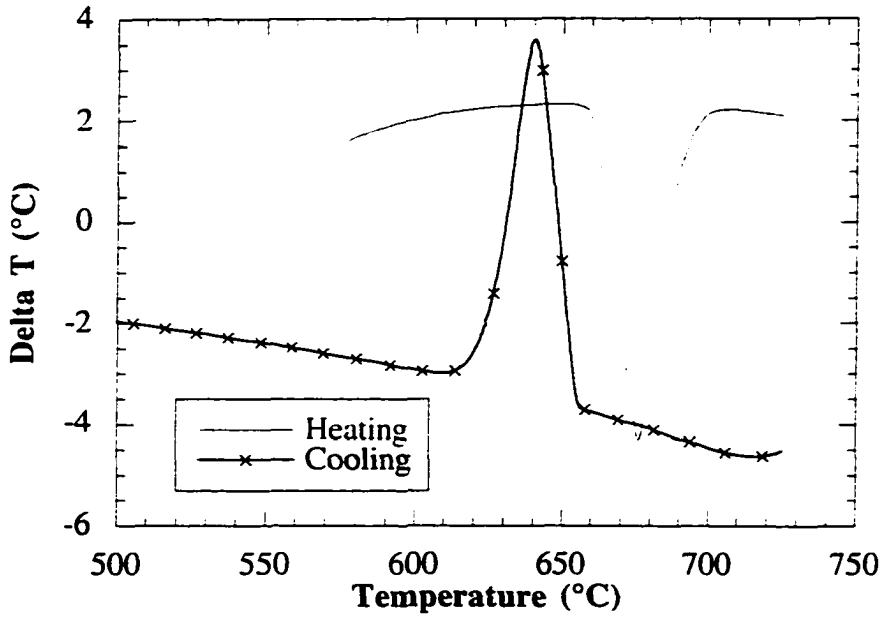

Figure 4.5. DTA trace of Alcoa pure aluminum ingot.

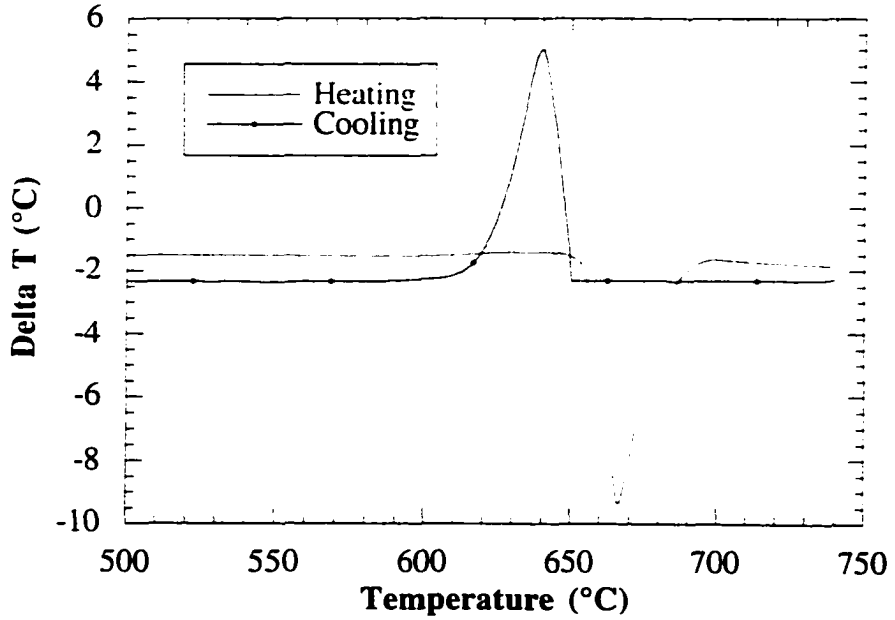

Figure 4.6. DTA scan of the GARS-6 pure aluminum powder in the as-atomized state.

indicate a slight melting point depression due to iron contamination in the aluminum powders. Table 4.5 lists the on-set temperatures for the reactions observed in pure aluminum powders.

Post-analysis examination of the DTA samples revealed that the GARS powders had agglomerated during the analyses. A similar post-DTA examination of a CAA pure aluminum powder, conducted by Dr. James Foley [78], showed the samples to be loose powders. These results seem to indicate a difference in the oxide film thickness between a GARS pure aluminum powder and a CAA pure aluminum powder, i.e., the former has a thinner oxide film than the latter. These post-DTA examinations correlate with the observations made during AES analysis of the GARS and a CAA aluminum powder, refer to the AES oxide thickness section in this chapter.

Table 4.5. DTA on-set temperatures of reactions during the heating and cooling of the Alcoa pure aluminum ingot and the GARS pure aluminum powders.

Powder	Heating Curve		Cooling Curve
Sample	First On-set (°C)	Second On-set (°C)	First On-set (°C)
GARS-3	656.4	None	653.4
GARS-4	656.4	658.3	652.4
GARS-5	656.2	None	652.6
GARS-6	654.4	657.8	651.6
GARS-7	650.5	653.5	649.7
GARS-8	656.4	659.9	652.2
Alcoa ingot	660.5	None	654.7

Quadrupole mass spectroscopy (QMS)

QMS was used to measure the water and hydrogen evolution from the GARS, CIGA-ATA, CIGA-VAL, and CAA aluminum powders under a simulated vacuum hot degassing (VHD) procedure. To facilitate direct comparisons between the QMS spectra of different aluminum powder samples, the QMS plots show the normalized mass currents of the water and hydrogen profiles as a function of temperature. The purpose for the normalization is to eliminate any influence of sample mass and differences of the initial mass current for either

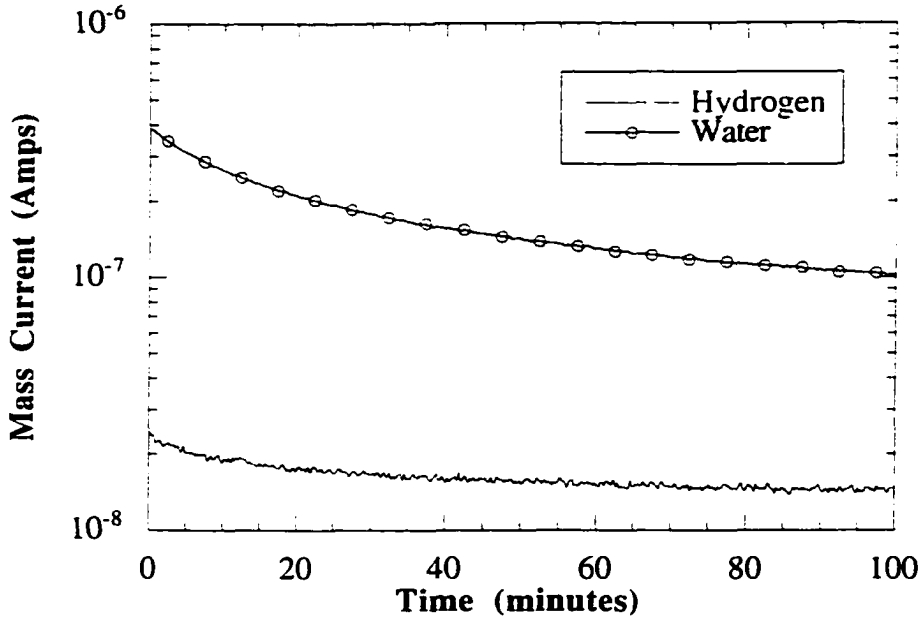

Figure 4.7. QMS plot illustrating the signal decrease of the water and hydrogen during the two hour UHV ambient temperature degassing procedure.

the water or the hydrogen profiles. For a given gas species, the normalized mass current is the measured mass current intensity, I, divided by an averaged initial mass current intensity, I_0. I_0 is the average of eight intensity measurements after the two hour UHV ambient temperature degassing procedure (Figure 4.7) and before starting the furnace for a QMS analysis under continuous heating conditions.

Figure 4.8 and Figure 4.9 are the relative water and hydrogen profiles of the "empty" crucible and the Alcoa aluminum ingot, respectively. The "empty" crucible results show there were no contributions from system dependent water to the QMS results of all the samples tested. The same may be said about the hydrogen profile of the empty crucible, other than an insignificant quantity of hydrogen, relative to the powder samples tested, evolved at temperatures greater than 550°C. One possible source for this residual hydrogen is outgassing of the stainless steel sheathed thermocouple.

The Alcoa aluminum ingot QMS results (Figure 4.9) indicate hydrogen evolution

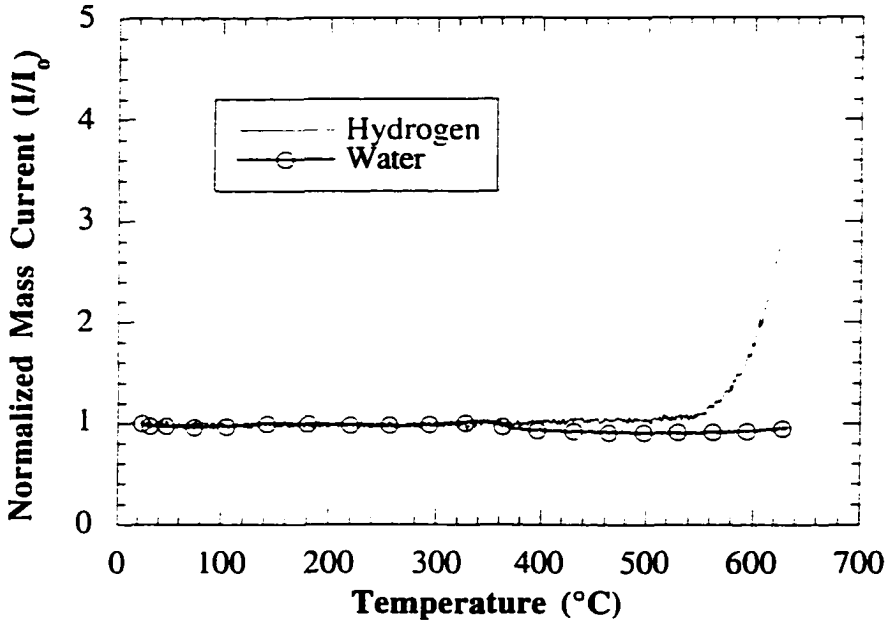

Figure 4.8. QMS water and hydrogen spectra for the empty furnace crucible heated at 5°C/min.

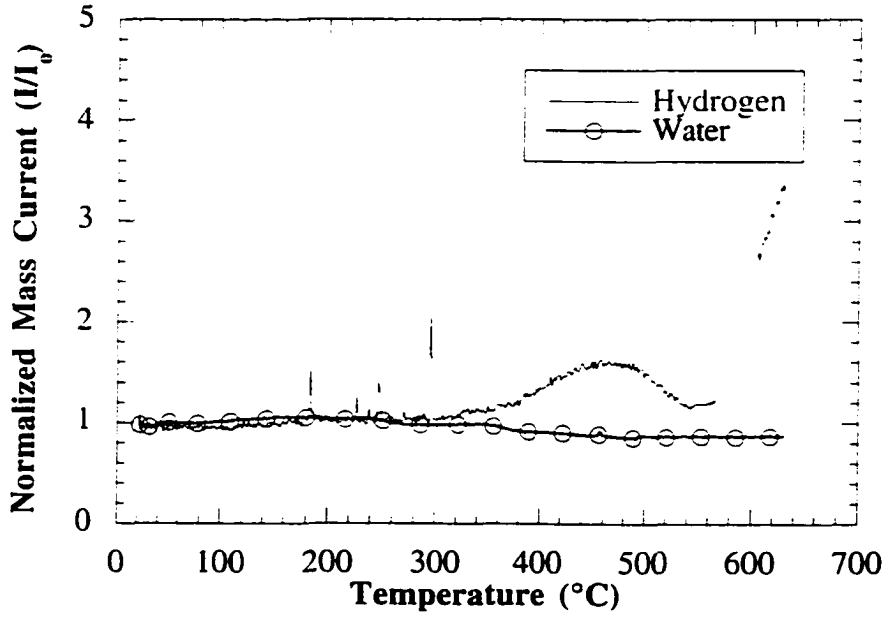

Figure 4.9. QMS results of 99.999% Alcoa aluminum ingot heated at 5°C/min.

throughout the continuous heating of the sample. The spikes in the hydrogen profile are characteristic of hydrogen trapped inside the volume of the ingot. Similar "pulses" were observed by Outlaw et al. [79]. The temperature of the last broad peak, between 320°C and 540°C, also seems to be characteristic of hydrogen evolving from the bulk volume. This last observation is important to keep in mind for the QMS characterization of the consolidated aluminum powders by CIP-VHD-HIP and CIP-VCD-HIP.

The hydrated alumina sample, shown in Figures 4.10a and 4.10b, shows the relative water peak positions as a function of temperature. These water peaks are characteristic of the type of chemisorbed water present in the surface oxide films of aluminum powder particles. The following QMS spectra will be described with an inferred reference to the thermal decomposition sequence shown in equation 2.11 of Chapter 2. The first relative maximum of the water signal corresponds to the thermal decomposition of the trihydrate oxide to the monohydrate oxide. The signal begins to rise at about 100°C to a relative maximum at about 235°C. The signal then decreases to a local minimum at about 400°C. A second local maximum (Figure 4.10b) observed to occur at 520°C, indicates the decomposition of the monohydrate oxide to an anhydrous oxide. The observed hydrogen signal is identified as part of the cracking spectra of water in a QMS system [80].

Figures 4.11, 4.12, 4.13, and 4.14 are QMS plots of the CAA, CIGA-ATA, CIGA-VAL, and GARS pure aluminum powders, respectively. For the CAA powder, the water signal increases to a maximum at about 150°C. This intensity rise is due to physiosorbed water being removed for the powder surfaces. As the physiosorbed water content diminishes, the mass current ratio of the water signal returns to the base line level. In the same profile, a small bump occurs at about 205°C, which may indicate chemisorbed water being removed from within the oxide film. The hydrogen curve starts its climb to a local maximum at 150°C. This peak corresponds to the QMS cracking spectra of water in the QMS system. As the temperature

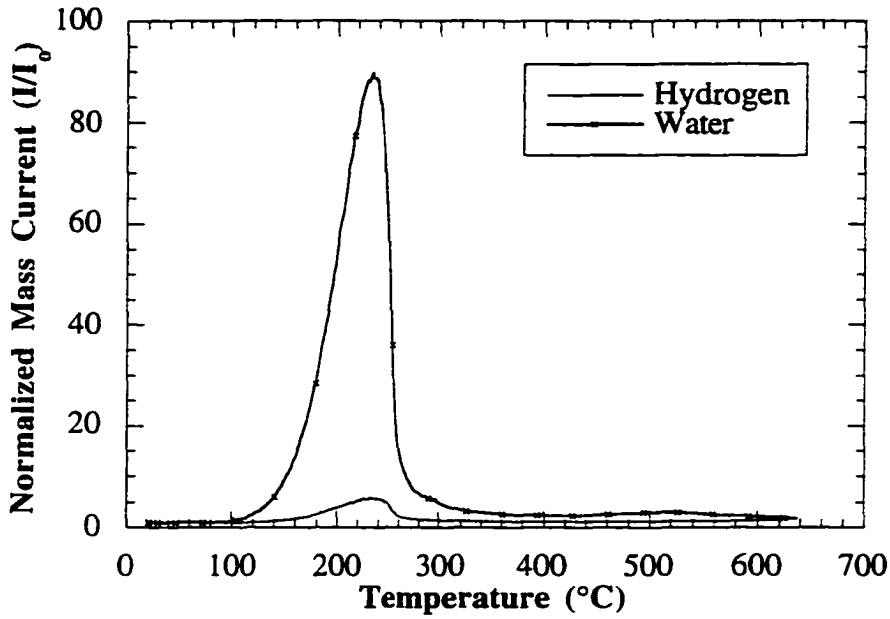

a. Overall QMS water and hydrogen scan of the trihydrate alumina.

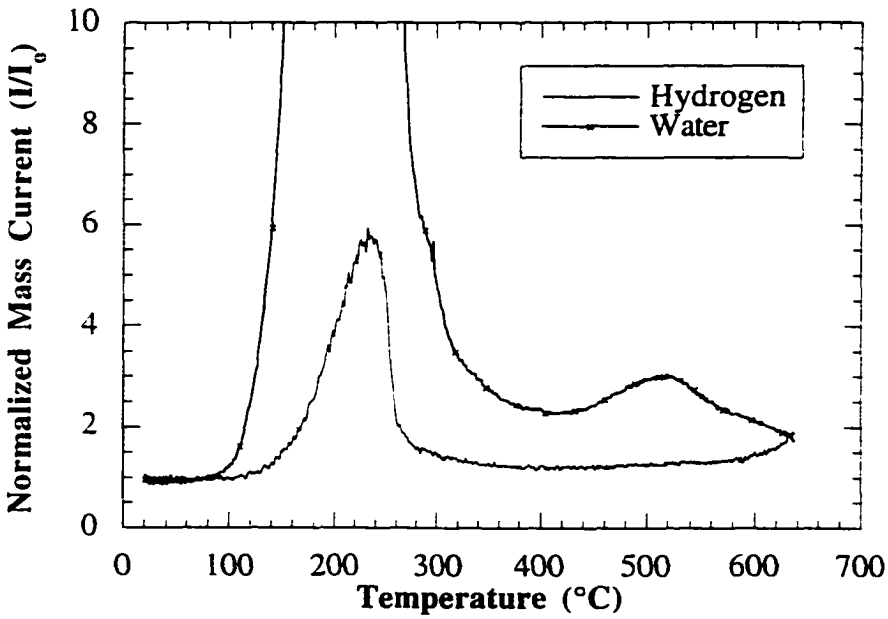

b. Expanded view of QMS scan to highlight the water peak at about 520°C.

Figure 4.10. QMS water and hydrogen spectra of the trihydrate alumina, ($Al_2O_3 \cdot 3H_2O$) heated at 5°C per minute.

increases, the signal decreases slightly, but then rises sharply to another local maximum in the range of 370°C to 440°C. This peak is characteristic of the trihydrate decomposing to the monohydrate and results from the reaction between the water in the oxide film and the aluminum diffusing through the oxide film. Above 440°C, the trihydrate has nearly completed its transformation to the monohydrate and, as a result, the hydrogen intensity decreases to a local minimum at 500°C. Continued heating of the sample begins the decomposition of the monohydrate to the anhydrous oxide, as indicated by the rise of the hydrogen intensity from 500°C to near 550°C. Again, the hydrogen being detected is a product of the reaction between the water and aluminum in the oxide film. The hydrogen profile decreases above 550°C due to the near completion of the transformation from the monohydrate oxide to the anhydrous oxide.

A similar detailed analysis was made of the CIGA-ATA, CIGA-VAL, and GARS aluminum powders. In the case of the CIGA-ATA aluminum powders (Figure 4.12) the water signal intensity is nearly three times higher than the CAA aluminum powders. The large increase would seem to indicate the presence of a significant quantity of physiosorbed water on the CIGA-ATA aluminum powder surfaces. The hydrogen profile of the CIGA-ATA aluminum powder is similar in shape and intensity as the CAA aluminum powder. The previous description of the CAA aluminum powder hydrogen profile could be restated for the hydrogen profile of the CIGA-ATA aluminum powder. The position of the last peak in the hydrogen profile is about 600°C.

The CIGA-VAL aluminum powder has a water signal intensity that is similar to the CAA, although the peak of the water signal has shifted to about 100°C. Above 100°C, the water signal decreases in a similar manner as the water signals of the CAA and CIGA-ATA aluminum powders. The hydrogen profile of the CIGA-VAL powder sample is similar to the hydrogen profile of the CIGA-ATA powder sample. The last peak of the hydrogen profile is at about 580°C.

The GARS aluminum powder has a similar QMS water profile as the CAA and both CIGA aluminum powders, with a reduced intensity. The hydrogen profile is initially different from the commercial aluminum powders. There is no apparent or distinct local maximum around 150°C, related to the cracking spectra of the water, which was observed in the QMS results of the commercial aluminum powders. No explanation is available for the absence of this hydrogen peak. However, a close analysis of the hydrogen profile does show a significant change of slope at 125°C, which may indicate the onset of the thermal decomposition of the alumina trihydrate phase. The slope change also corresponds to the local minimum in the water profile at 125°C. Continued heating above 125°C of the GARS powder sample shows the hydrogen profile to have similar features as the commercial aluminum powders with about half the intensity.

Direct comparisons of the water spectra for the CAA, CIGA-ATA, CIGA-VAL, and GARS powders (Figure 4.15) shows the water signal intensities vary due to the level of physiosorbed water on the powder surfaces. A composite plot of the hydrogen profiles for the pure aluminum powder investigated (Figure 4.16) shows the distinguishable differences.

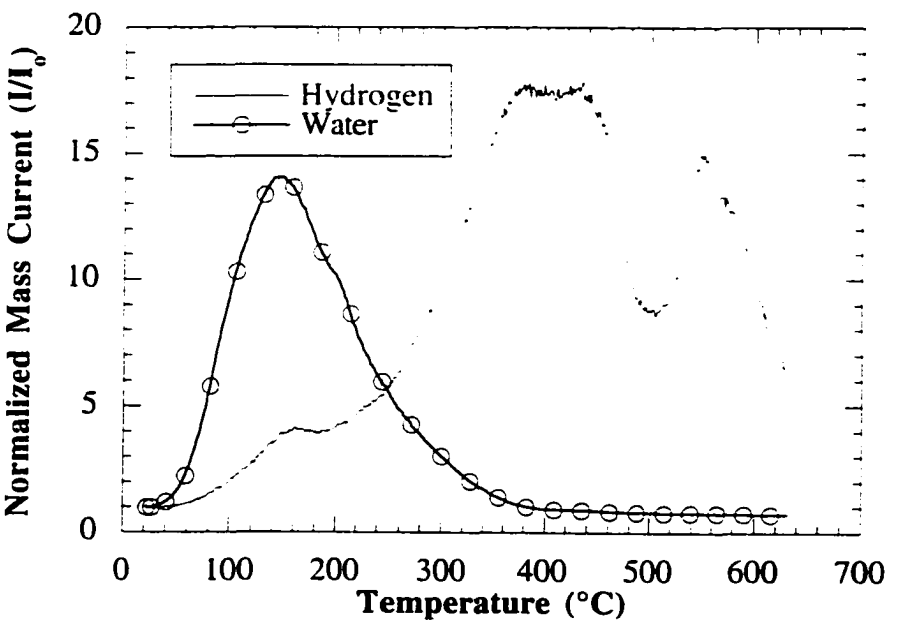

Figure 4.11. Representative QMS plot of the CAA aluminum powder heated at 5°C/min.

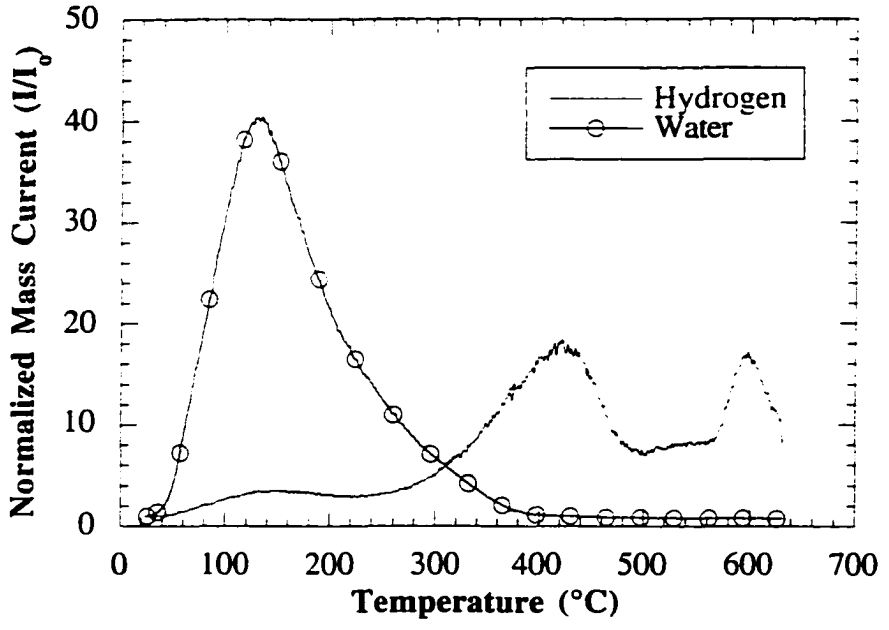

Figure 4.12. Representative QMS plot of CIGA-ATA aluminum powder heated at 5°C/min.

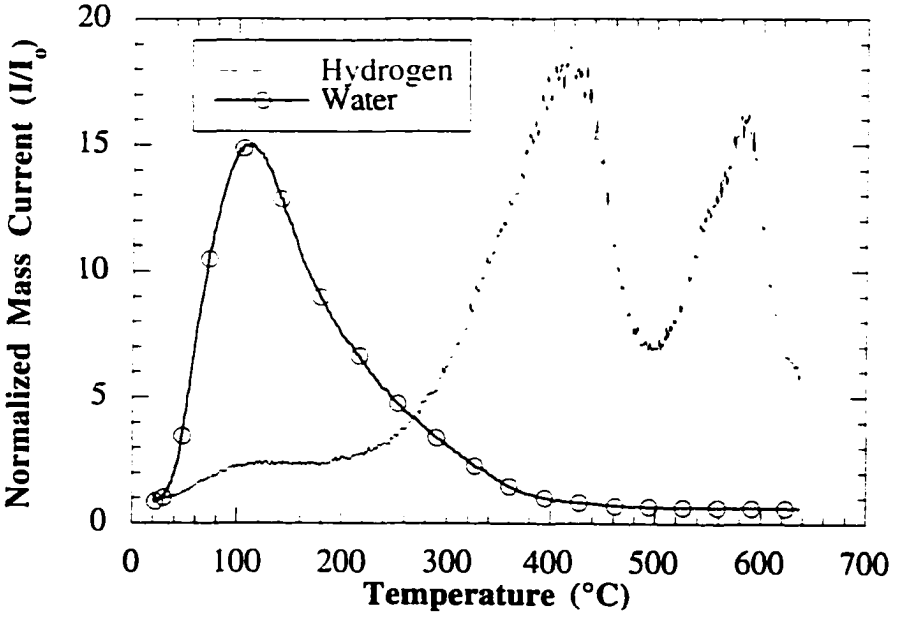

Figure 4.13. Representative QMS plot of CIGA-VAL aluminum powder heated at 5°C/min.

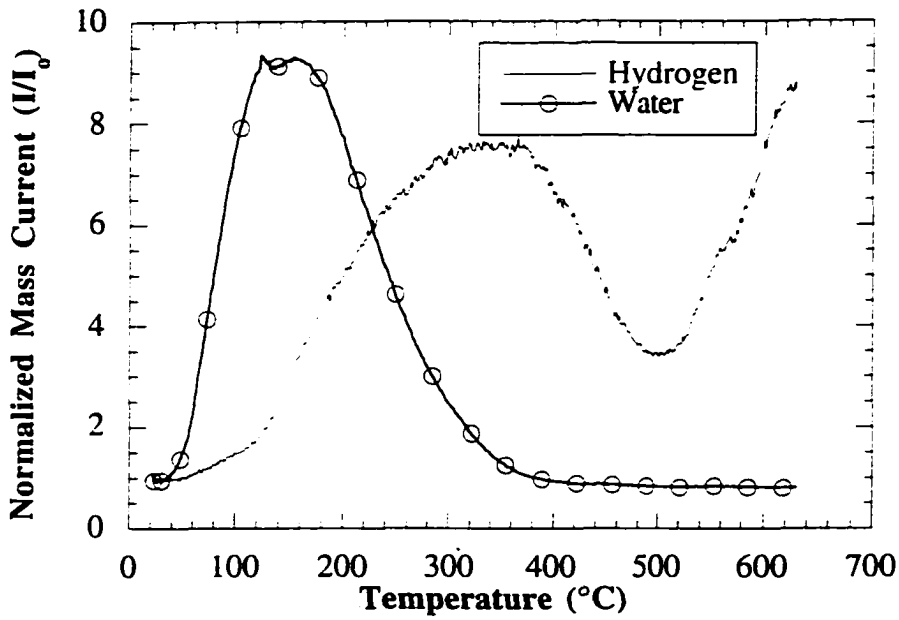

Figure 4.14. Representative QMS plot of GARS-4 aluminum powder heated at 5°C/min.

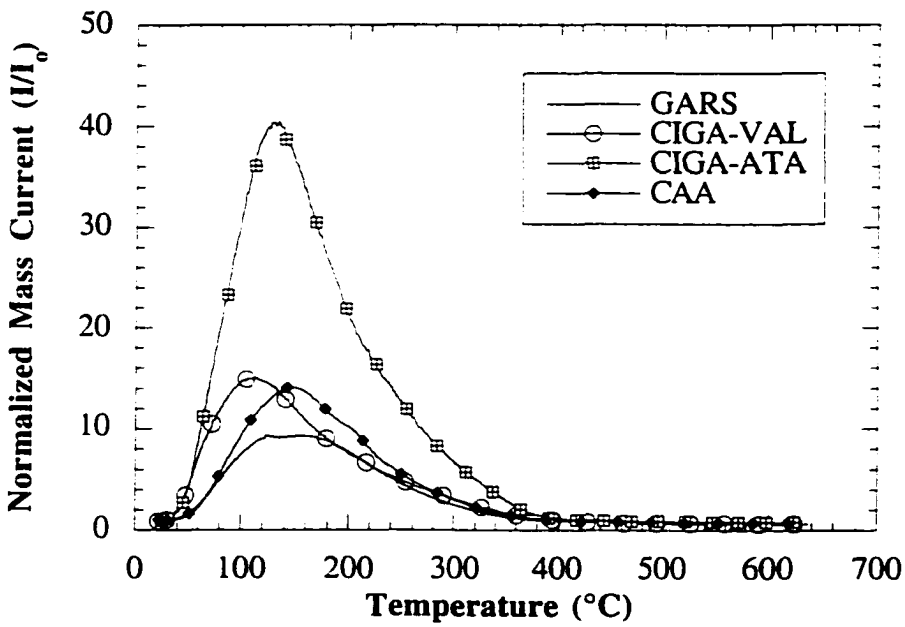

Figure 4.15. Comparison of the water evolution from the GARS, CIGA-VAL, CIGA-ATA and CAA pure aluminum powders during the QMS experiments.

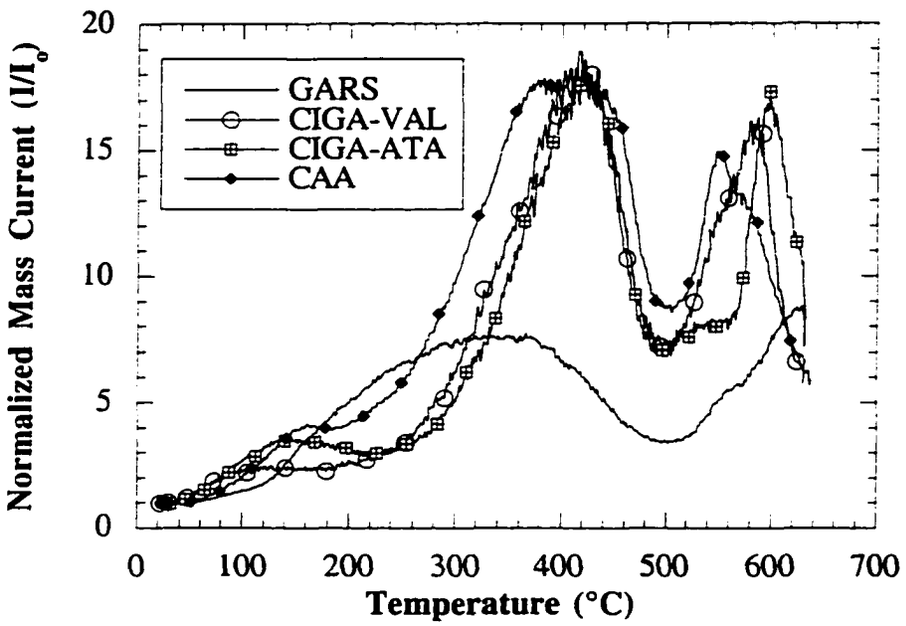

Figure 4.16. Comparison of the hydrogen evolution from the GARS, CIGA-VAL, CIGA-ATA, and CAA pure aluminum powders during the QMS experiments.

previously noted, of the hydrogen signals. The area under a hydrogen curve, at constant heating rate and compact density, is a relative measure of the quantity of hydrogen evolving from the aluminum powder surfaces, and in turn, could be directly related to the amount of chemisorbed water in the oxide film. The perimeter of the area under a hydrogen profile is defined by the start and stop temperatures of the experiment, the hydrogen curve, and a normalized mass current value of one. An examination of the areas under the curves for the various aluminum powders (Table 4.6) shows the GARS-4 aluminum powder to have the least amount of evolved hydrogen and the CAA aluminum powder to have the most evolved hydrogen. Both CIGA aluminum powders are intermediate of the GARS-4 and CAA aluminum powders. Again, the hydrogen measured is a product of the water chemisorbed into the oxide film during gas atomization.

Changes in heating rate of powder samples with the same green density (Figure 4.17) may affect the QMS results significantly. One observation is a change of the on-set

Table 4.6. Relative areas under the water and hydrogen profiles for the powder samples.

Sample and Figure Number	Area Under Water Profile	Area Under Hydrogen Profile
Empty Crucible / Figure 4.8	-28	63
Alcoa Al Ingot / Figure 4.9	-30	170
GARS-4 Powder / Figure 4.11	1335	2399
CIGA-ATA Powder / Figure 4.12	5429	3920
CIGA-VAL Powder / Figure 4.13	1977	4055
CAA Powder / Figure 4.14	1836	4835

temperature of the last peak in each signal profile, which increases with increasing heating rate, and is probably associated with an activation energy of some kinetic process. Increasing the heating rate also increases both the signal intensity and the relative area under the hydrogen curves. The signal increases are due to a state of equilibrium between the rate of hydrogen evolution from the sample and the pumping speed of the turbo-pump. In other words, higher heating rates stimulate faster hydrogen evolution form the sample, and because the turbo-pump does not change speed, more hydrogen is detected by the QMS instrumentation. Another contribution to the increased hydrogen is due to the fact that hydrogen gas is difficult to remove from a vacuum chamber. Changes in the QMS data may also occur for samples with different densities at the same heating rate (Figure 4.18). Samples with higher densities and similar masses tend to show higher signal intensities and larger relative areas under the hydrogen profiles, particularly with respect to the first peak of each hydrogen profile at about 425°C.

AES Oxide thickness

The AES data was collected to determine the relative oxide thickness of the CAA, CIGA-ATA, and GARS aluminum powders and attempt to relate the thickness measurements to the respective atomization process. Table 4.7 shows the AES oxide thicknesses of all the GARS pure aluminum powders, the CAA pure aluminum powder and the both CIGA pure aluminum powders. Representative AES concentration depth profiles for the GARS and CAA aluminum powders are shown in Figure 4.19 and Figure 4.20, respectively. The

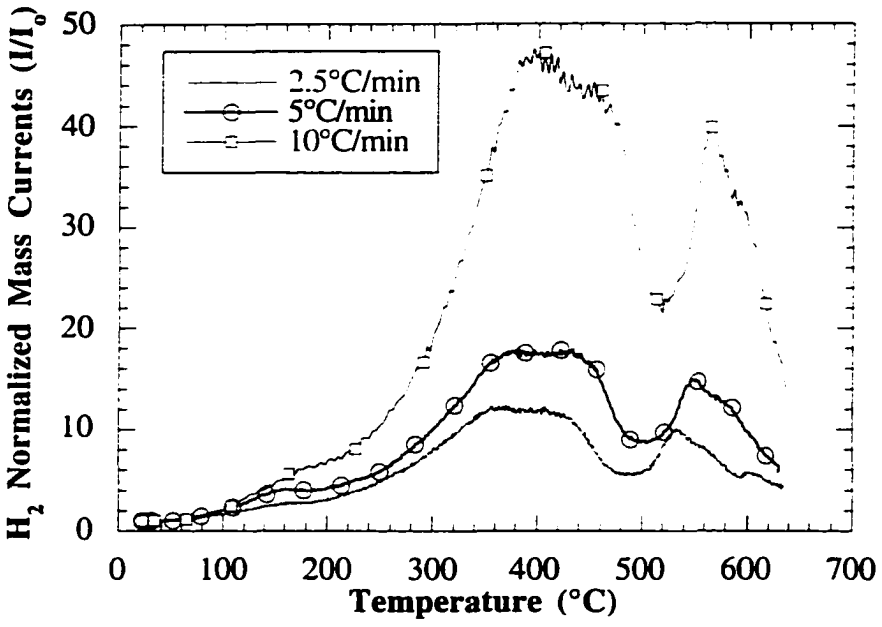

Figure 4.17. The effect of different heating rates during a QMS examination of CAA aluminum powder at a constant sample density of 92.3%.

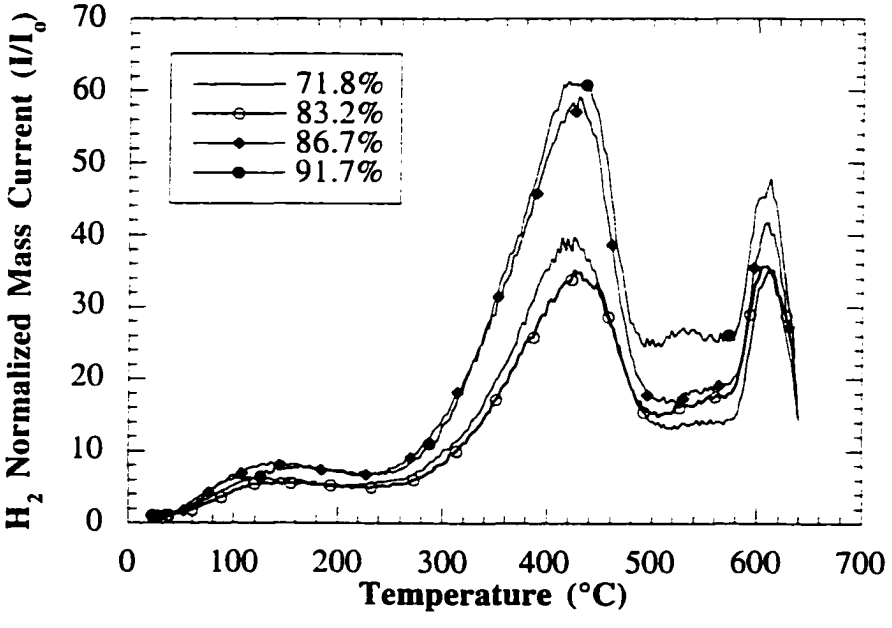

Figure 4.18. The effect of sample density variations during QMS analyses of CIGA powder at constant heating rate of 10°C per minute.

thickness measurements recorded in Table 4.7 were made according to the method defined by Norell et al. [81] and is schematically shown in Figure 4.21. The oxide thickness is measured at the fifty percent level of the maximum oxygen content at the surface of the powder and the apparent minimum or baseline oxygen content inside the powder. The AES values for the GARS-7, GARS-8 and GARS-9 aluminum powders are representative of the unexposed oxide film thickness. The GARS aluminum powders generally have a thinner oxide film than the CAA aluminum powders. The oxide thickness of the CIGA-ATA aluminum powder is

Table 4.7. AES oxide thickness measurements of as-atomized aluminum powder particles.

Powder Type	Oxide Thickness (Å)
GARS-2[a]	80.7 ± 11.2
GARS-3	68.7 ± 37.6
GARS-4	30.2 ± 7.8
GARS-5	82.2 ± 58.1
GARS-6	46.2 ± 18.7
GARS-7	30.0 ± 4.8
GARS-8	16.6 ± 4.7
GARS-9	26.9 ± 4.4
CIGA-ATA	41.1 ± 23.0
CIGA-VAL	159.0 ± 28.7
CAA	124.5 ± 9.3

[a] AES data collected with GARS-2 aluminum powder pressed into indium foil.

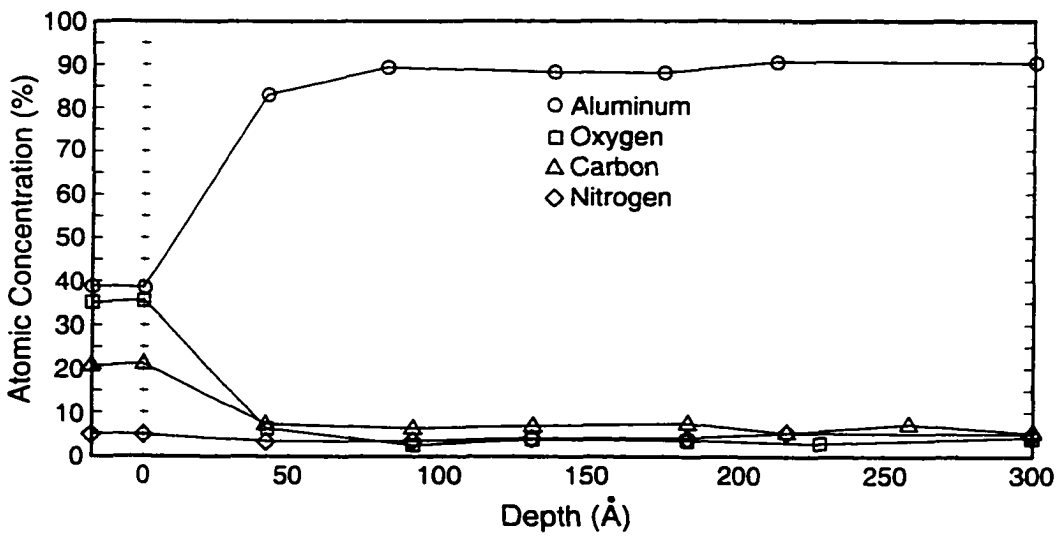

Figure 4.19. Representative AES concentration depth profile for GARS aluminum powders.

comparable to the GARS aluminum powders while the CIGA-VAL aluminum powder has the thickest oxide film. In general, inert gas atomized aluminum powders have thinner oxide films seemly due to less oxygen exposure during the inert gas atomization process than during the CAA process.

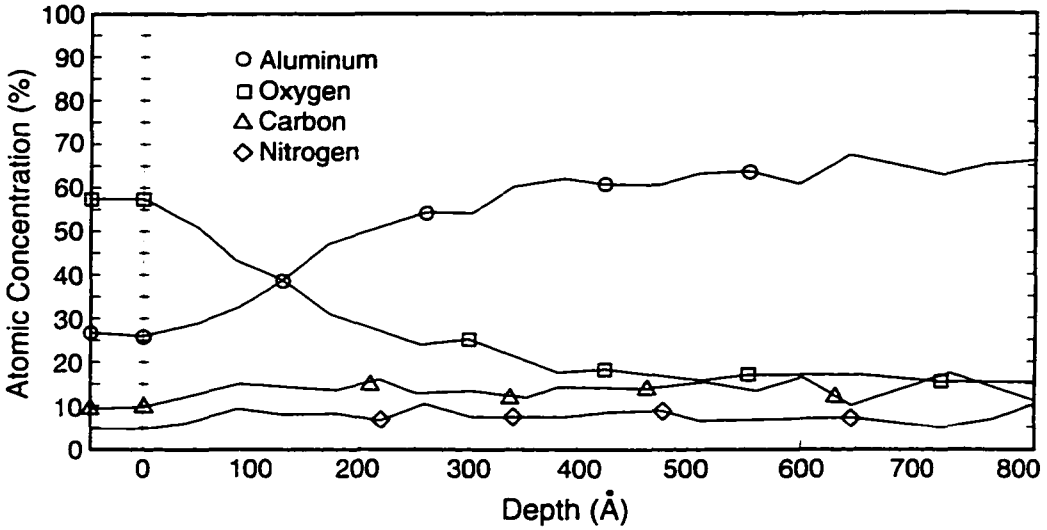

Figure 4.20. Representative AES concentration depth profile for CAA aluminum powders.

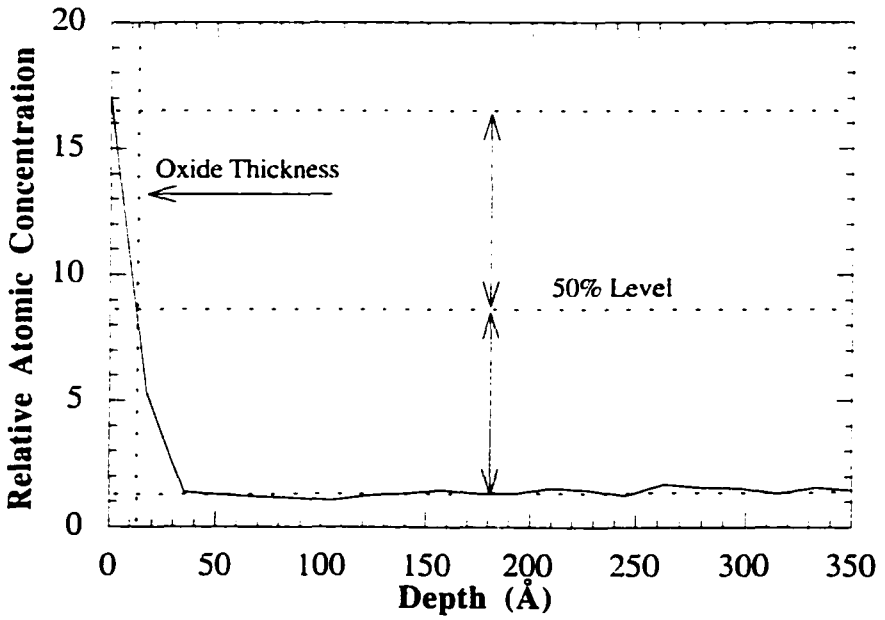

Figure 4.21 Example AES oxygen depth profile for the measurement method used to determine the oxide thickness of aluminum powders.

The variance of the AES oxide film thickness data has two possible sources of error. In some cases, a high carbon content was noted by the AES operator during sputtering of the powder surfaces. The carbon has the potential to mask the oxygen signal from the detector, reducing the measured oxygen content of the initial layers. The outcome is a measured oxide thickness that is thinner than the actual thickness. Another possible reason for the oxide thickness variances is due to a non-uniform oxide thickness on aluminum powders of the same size. The non-uniform thickness argument was presented by Norell et al., however, the AES results used in this research show no apparent dependence of oxide thickness on similar powder particle sizes.

One process variable that may influence the AES oxide thickness is the pouring temperature of the molten aluminum. Figure 4.22 is a plot of the GARS oxide thickness data, presented in Table 4.7, as a function of the pouring temperature of the aluminum melt. The GARS-2 AES data is not included in this figure, because of different atomization conditions and a different AES analysis than that used for the later GARS powders. For reference, the AES oxide thicknesses of the CAA, CIGA-ATA, and CIGA-VAL aluminum powders are also plotted in Figure 4.22, as well as the range of the expected atomization pouring temperature.

The outcome of the GARS aluminum powders is an expanding range of the measured oxide thickness with increasing pouring temperature. The AES samples of the GARS powders, labeled with the closed symbols, were not collected under an inert atmosphere during post-atomization handling of the powder. The exposure of these powders to the ambient air allowed the oxide to grow to varying degrees before AES samples were prepared, and hence, the wide variances of the oxide thickness measurements. On the other hand, the GARS powders collected under an inert atmosphere during post-atomization handling, labeled with the open symbols, show significantly less scatter of the oxide thickness measurements, indicating the pouring temperature of the molten aluminum is not a strong

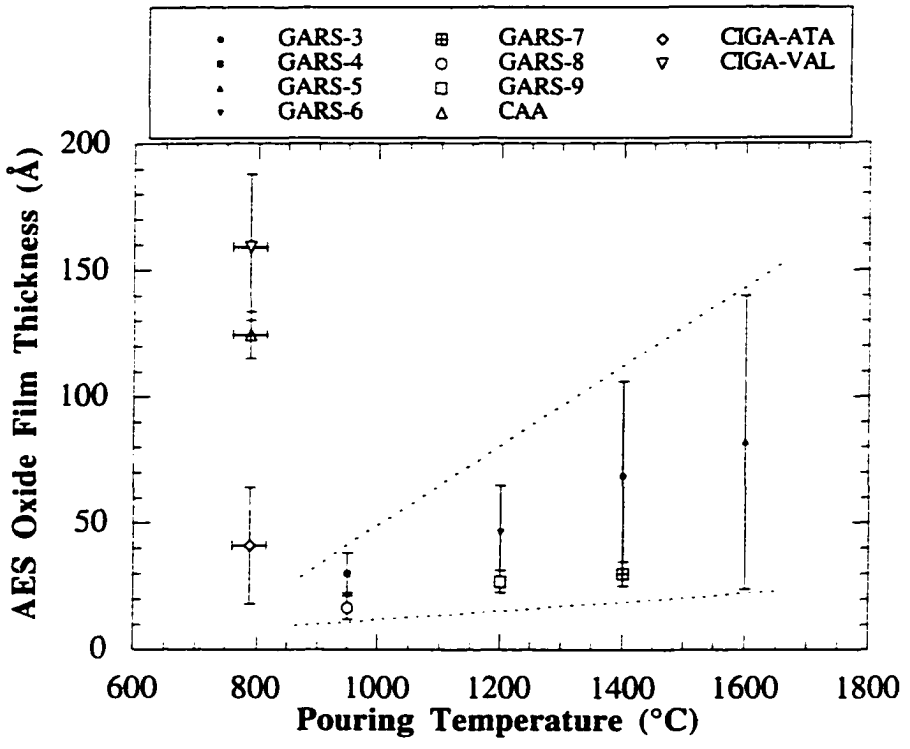

Figure 4.22. AES oxide film thickness as a function of pouring temperature.

variable in determining the oxide thickness. Also, the small variances seem to be a good measure of the initial oxide thickness which develops during a GARS atomization process.

Transmission electron microscopy (TEM)

TEM of the CAA and GARS-8 aluminum powders, shown in Figure 4.23 and Figure 4.24, respectively, was conducted to directly measure the oxide film thickness of aluminum powders, measure the oxide film chemistry with EDS, and determine if the oxide film structure is amorphous or crystalline. The thickness of the oxide films were measured with an image analysis software package. The average oxide film thickness of the GARS-8 sample was 107±37 Å and the average oxide film thickness of the CAA aluminum powders was 116±33 Å (Figure 4.25). The measurements were made on other brightfield micrographs of the same sample in the areas similar to those indicated by arrow markers on Figure 4.23 and Figure 4.24.

Figure 4.23. TEM micrograph and SAD pattern of the oxide film on CAA aluminum powder. The arrows indicate the oxide thickness measurements.

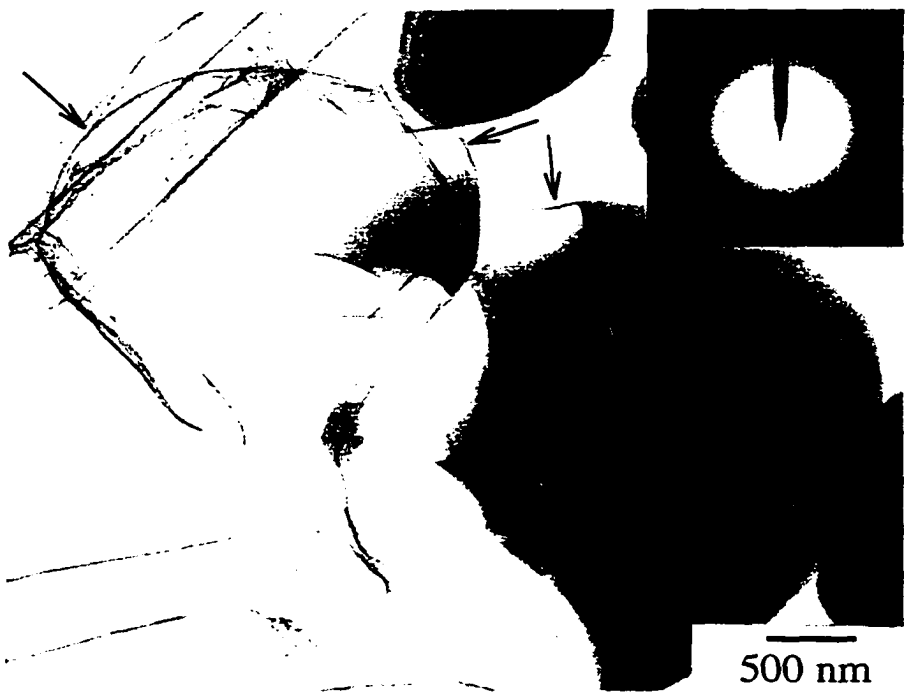

Figure 4.24. TEM micrograph and SAD pattern of the oxide film on GARS aluminum powder. The arrows indicate oxide thickness measurements.

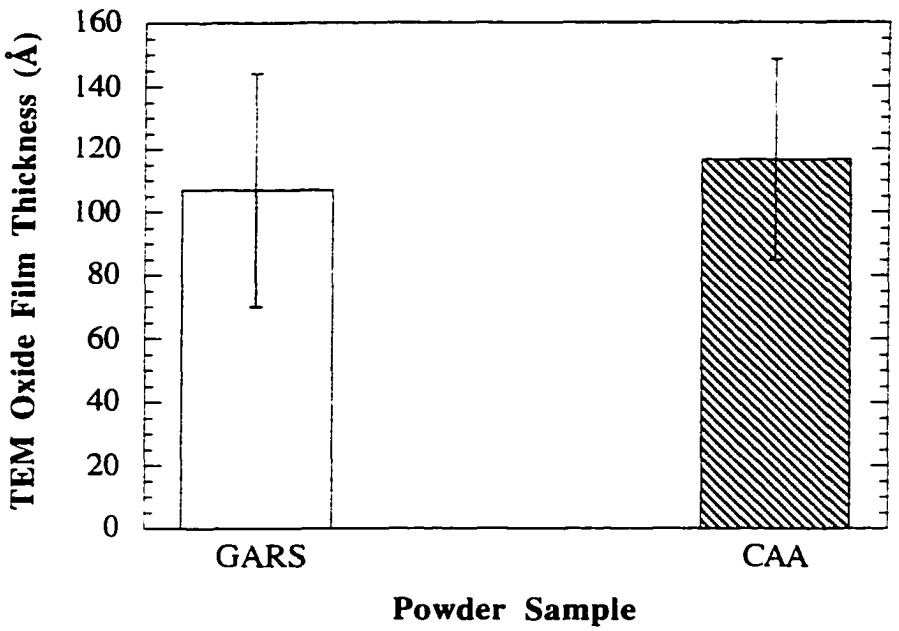

Figure 4.25. TEM measurements of the oxide film thickness on the GARS-8 and CAA pure aluminum powders

The measured points were selected at the thinnest, darkest, linear features of the oxide film in the microstructure. The GARS-8 oxide thickness measurements were made on the powder particles. The CAA sample did not have individual powder particle features that were observed on the GARS-8 aluminum powders. In the case of the CAA microstructure, the oxide thickness measurements were made at the boundaries between two adjacent prior powder particles. The boundary measurements were then divided by two for the oxide film thickness measurements, assuming the oxide film thickness of each powder particle contributed equally to the boundary thickness.

The TEM oxide thickness results agree reasonably well with the AES data of the CAA aluminum powders and the GARS-8 aluminum powders after being exposed to ambient air for 300 hours. The TEM oxide thickness measurements are physical measurements, made with some degree of subjectivity, which indicate the thickest oxide film to exist on aluminum powders. The AES oxide thickness measurements are made at the fifty percent level of the

oxygen concentration depth profile (Figure 4.21) and could be considered the thinnest oxide film thickness to be present on an aluminum powder particle.

The EDS oxide film chemistry of the CAA aluminum powder, (Figure 4.26) was less pure than the EDS oxide film chemistry of the GARS-8 aluminum powder (Figure 4.27) most likely due to the bulk chemistry measurements in Table 4.4. A closer look at the physical appearance of the TEM oxide microstructures shows a similar trend. The CAA aluminum powder oxide film (Figure 4.23) appears "dirtier" than the GARS-8 aluminum powder oxide film (Figure 4.24). SEM images of the same TEM samples, shown in Figure 4.28 and Figure 4.29, shows more residual oxide present on the CAA sample than on the GARS sample, possibly due to the larger surface area of the CAA aluminum powders compared to the GARS aluminum powders.

The structure of the oxide film on aluminum powders is amorphous, as indicated by the diffuse diffraction rings on the SAD patterns inset on Figure 4.23 and Figure 4.24. The amorphous structure was also indicated by the lack of contrast changes in the microstructure of the CAA aluminum powder during a tilt of the foil in a dual tilting sample holder. The amorphous structure appears to be independent of the atomization method.

Aluminum alloy powder characterization

Al-Ti-Y aluminum alloy powder

The Al-Ti-Y powder was initially produced to observe if the addition of other elements with strong nitride formation thermodynamics would stimulate a GARS type reaction between the UHP nitrogen atomization gas and the molten aluminum alloy droplets. The bulk chemistry of the Al-Ti-Y alloy aluminum powder (Tables 4.8) shows a low bulk nitrogen content, which seemingly indicates no nitride formation during the nitrogen gas atomization experiment. Similarly, an XRD scan (Figure 4.30) reveals no apparent nitride phase. The XRD data does not conclusively rule out the possibility of a nitride phase being

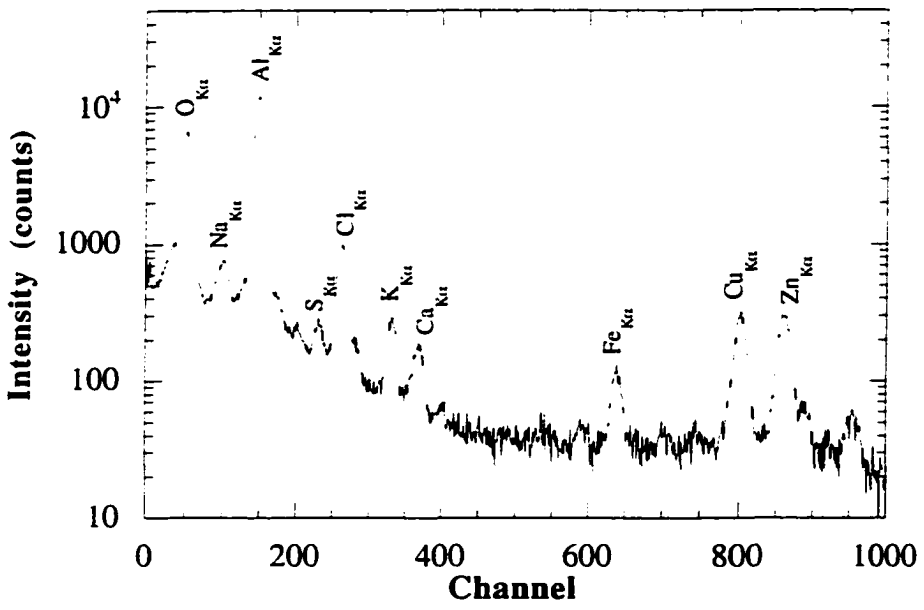

Figure 4.26. EDS spectra of the oxide film on CAA aluminum powder.

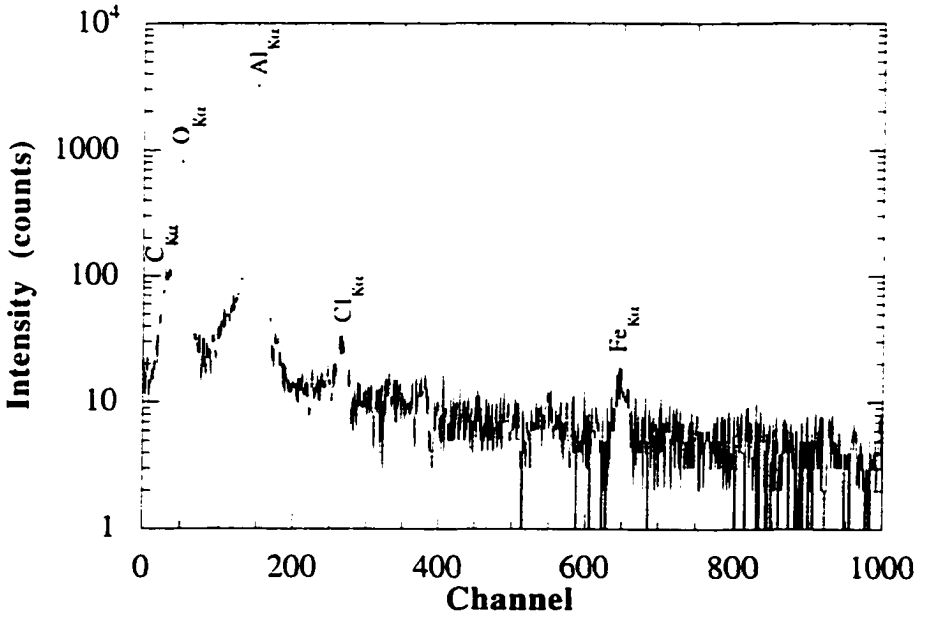

Figure 4.27. EDS spectra of the oxide film on GARS-8 aluminum powder.

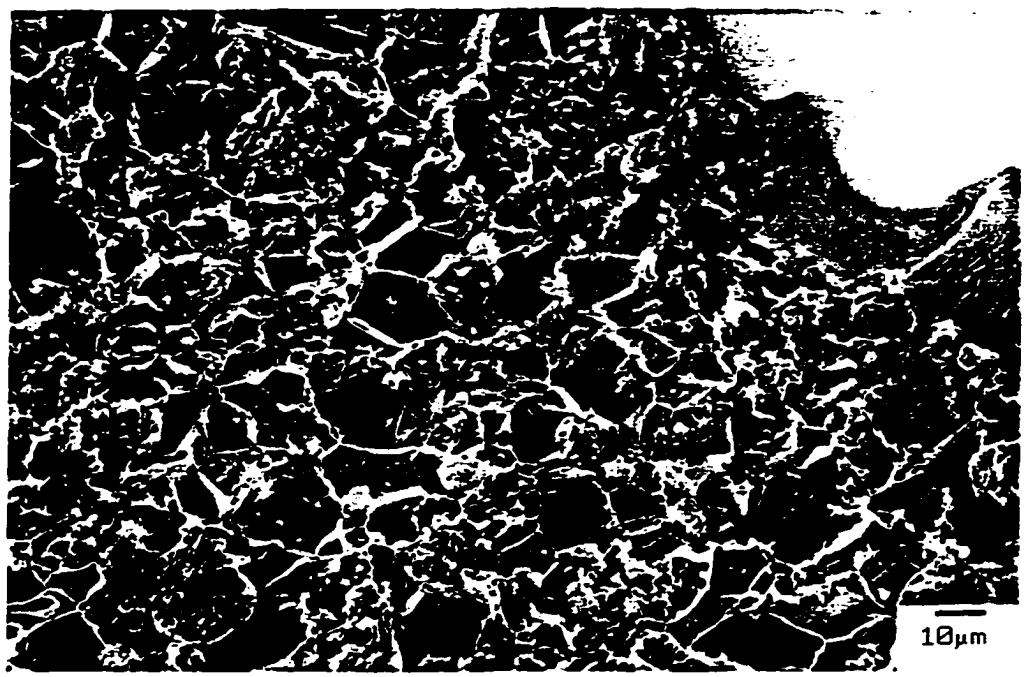

Figure 4.28. SEM micrograph of CAA aluminum powder TEM sample in Figure 4.23.

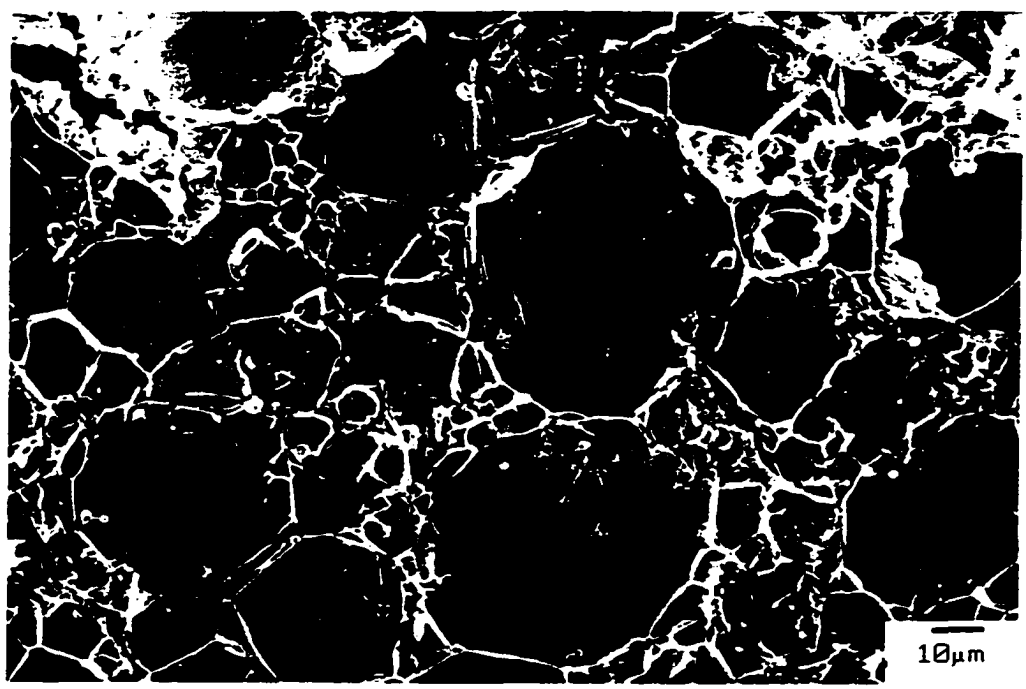

Figure 4.29. SEM micrograph of GARS-8 aluminum powder TEM sample in Figure 4.24.

present, because the volume fraction of the nitride phase could be below the detectability limit of XRD instrumentation. The DTA scan (Figure 4.31) also provides no evidence of a nitride phase reaction. The detectable transformations are associated with the aluminum-yttrium and aluminum-titanium phase diagrams shownn in Figure 4.32 and Figure 4.33.

Table 4.8. ICP-AES and IGF measurements of as-atomized Al-Ti-Y aluminum alloy powder.

Element	Chemical Content	Units
Aluminum	Balance	wt. %
Titanium	3.49	wt. %
Yttrium	6.93	wt. %
Oxygen	2	ppmw
Nitrogen	634	ppmw
Carbon	40	ppmw

The XRD scan shows the phases present in the as-atomized powder, namely, Al, β-Al_3Y, Al_2Y, Al_3Ti, AlO_3Y, and $Al_5O_{12}Y_3$. The Al_3Ti identification is weak, because its calculated volume fraction, 5.6 volume percent, is near the detectability limits of XRD. The other phases, though, have several identifiable peaks indicating their presence in the powder. The calculated volume fraction of the β-Al_3Y is 8.7 volume percent.

Looking closely at the heating curve in Figure 4.31 the exotherm marked as point 1 has an on-set temperature of 640°C which corresponds to the aluminum-yttrium eutectic at nine weight percent yttrium. According to the phase diagram the eutectic could be the equilibrium reaction between aluminum and β-Al_3Y or the metastable reaction between aluminum and Al_2Y. The second exotherm, point 2 on the heating curve, has an on-set temperature of 866.4°C believed to correspond with the liquidus line rising from the aluminum-yttrium eutectic at nine weight percent yttrium. There is no apparent exotherm for the Al_3Ti phase transformation at higher temperatures.

The cooling curve, though, does indicate a reaction at point 3 with an on-set temperature of 1053.8°C. The intersection of this temperature and the concentration of titanium listed in Table 4.8 above, corresponds well the liquidus line on the aluminum rich

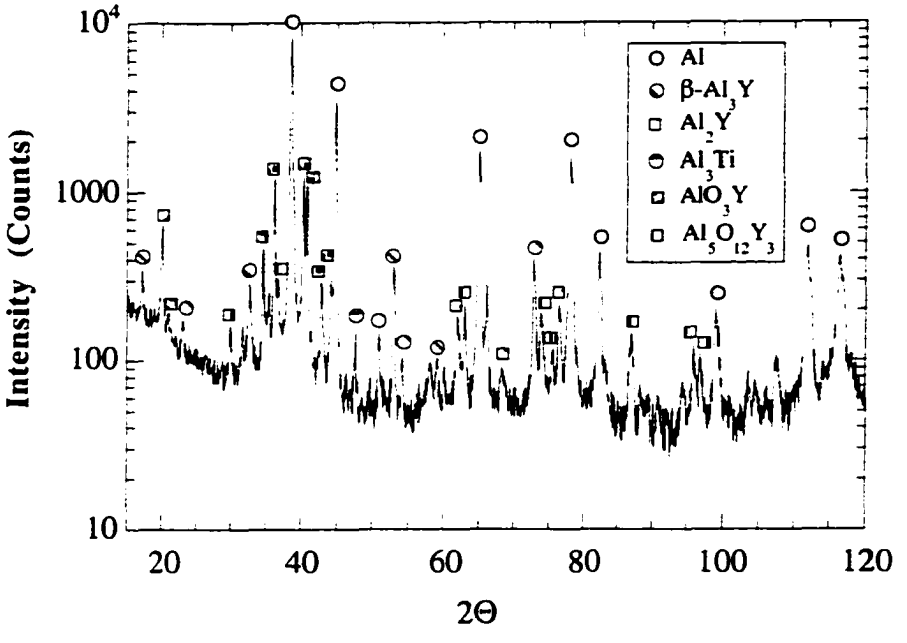

Figure 4.30. XRD scan of Al-Ti-Y powder in the as-atomized state.

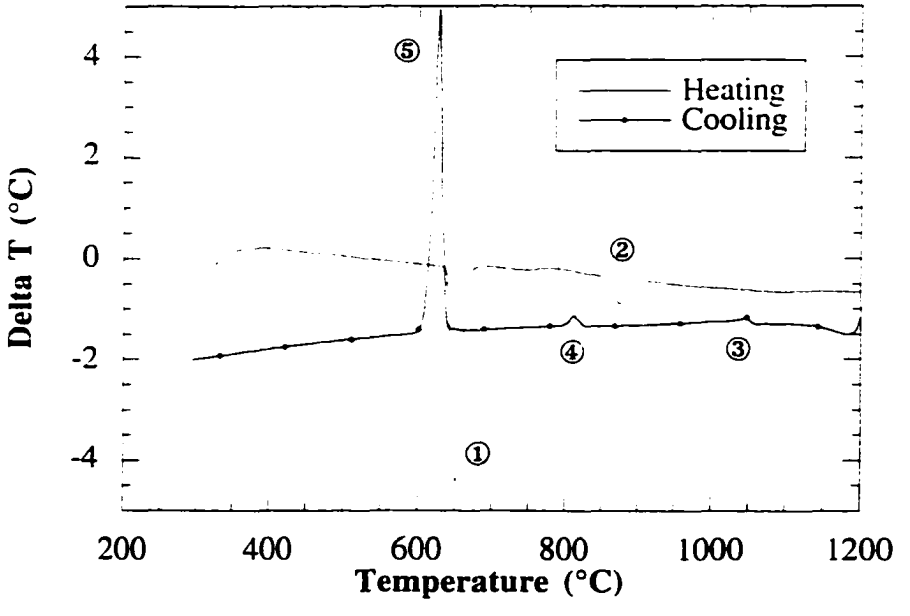

Figure 4.31. DTA of Al-Ti-Y alloy powder in the as-atomized condition.

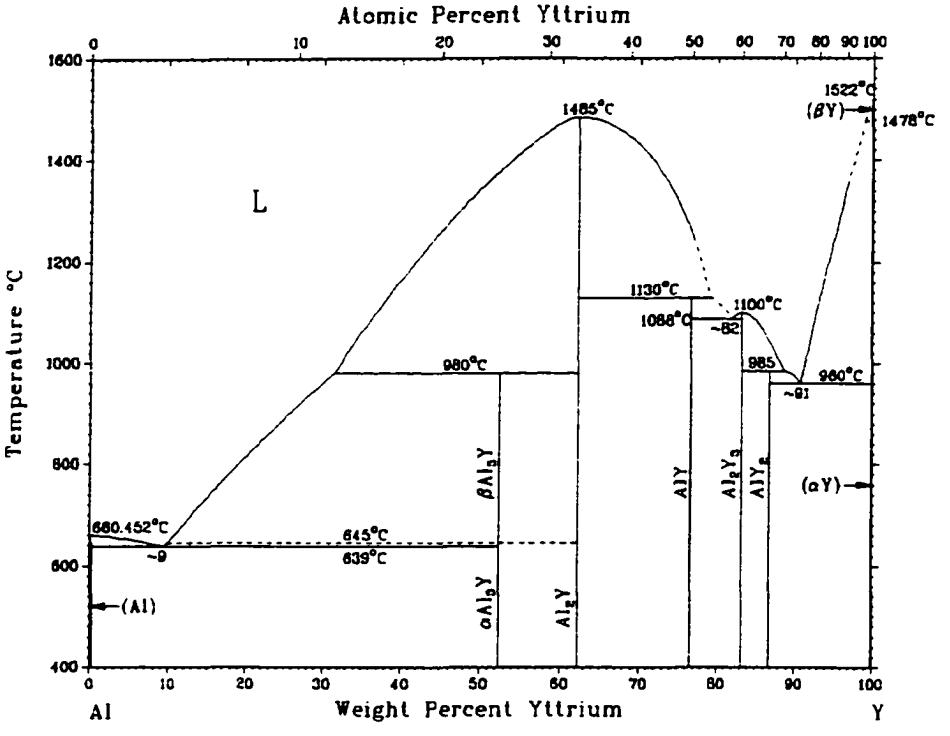

Figure 4.32. Aluminum-yttrium phase diagram [82].

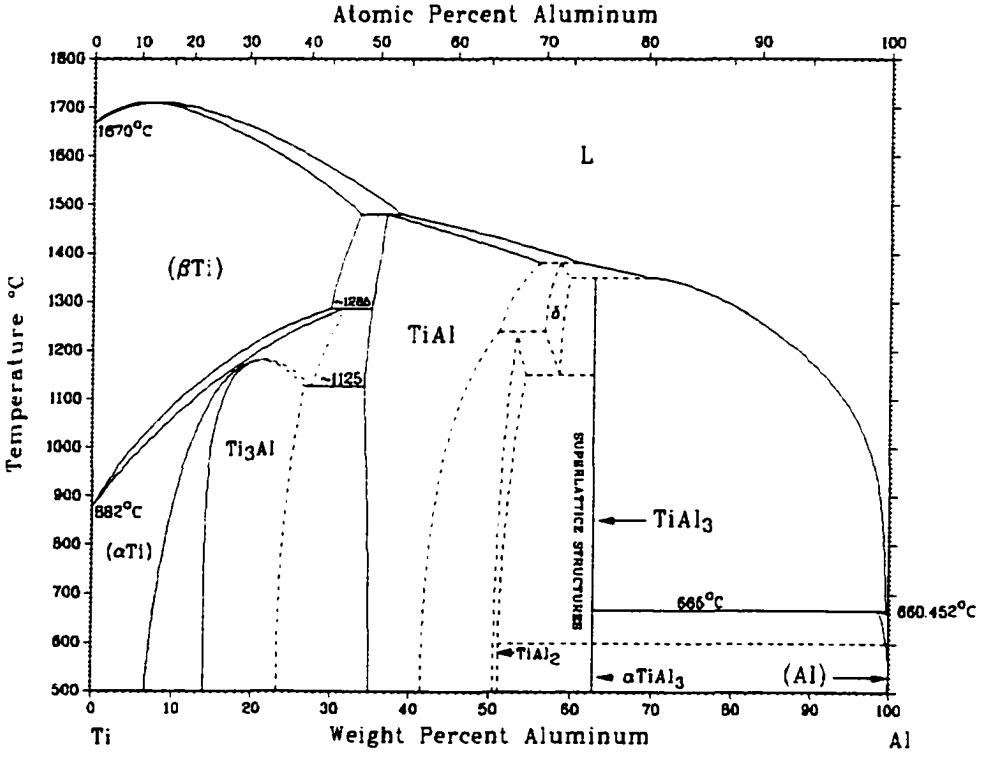

Figure 4.33. Aluminum-titanium phase diagram [83].

side of the aluminum-titanium phase diagram in Figure 4.33, indicating the formation of Al_3Ti. Another possible reaction is the formation of the Al_2Y phase, but there is no reaction indicated at about 980°C that would be associated with the formation of Al_2Y or the subsequent formation of β-Al_3Y. The next transformations do not occur until points 4 and 5 on the cooling curve, far below the 980°C formation temperature for β-Al_3Y. These last two reactions on the cooling curve relate to the transformations previously described as point 2 and point 1, respectively, on the heating curve.

Al-Cu-Mg alloy powder

The Al-Cu-Mg aluminum alloy powder, a CIGA-VAL type powder produced by Valimet Inc., was selected for evaluation in the QMS experiments to compare the differences that might occur between VHD of a pure aluminum powder and an aluminum alloy powder with magnesium, produced at the Valimet atomization facility using the SSA gas atomization method. The alloy QMS results are compared with other published data on similar aluminum-magnesium alloys. The Al-Mg-Cu alloy powder chemistry is listed in Table 4.9 and the QMS results for the Al-Mg-Cu powder alloy are shown in Figure 4.34.

Figure 4.34 shows the water signal intensity rising to a maximum intensity at 110°C, which is indicative of physiosorbed water being removed from the powder surfaces. As the signal decreases, a local maximum occurs at 170°C characteristic of the start of the decomposition of the alumina trihydrate to the monohydrate oxide. The water intensity continues its decline slowly at first, but at about 420°C the signal drops rapidly. Meanwhile,

Table 4.9. ICP-AES and IGF measurements of as-atomized Al-Cu-Mg CIGA-VAL type aluminum alloy powder.

Element	Chemical Content	Units
Aluminum	Balance	wt. %
Copper	4.0	wt. %
Magnesium	1.28	wt. %
Oxygen	1377	ppmw
Nitrogen	4	ppmw

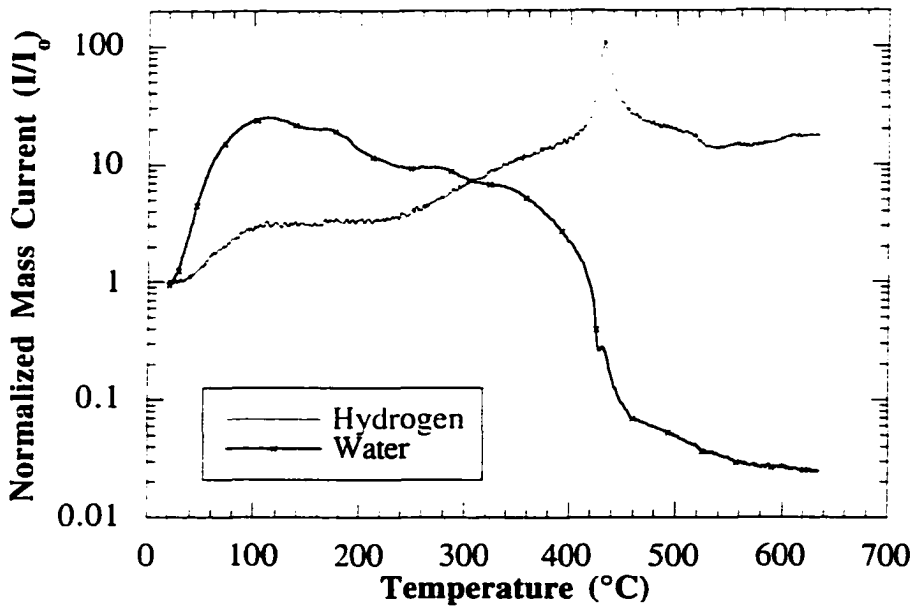

Figure 4.34. QMS water and hydrogen spectra of Al-Cu-Mg aluminum alloy powder at 5°C per minute.

the hydrogen signal intensity, which had been increasing slowly, spikes at the same time reaching a maximum at 432.3°C in short order. The hydrogen intensity decreases to a nearly constant level.

A comparison the CIGA-VAL SSA pure aluminum powder with the CIGA-VAL SSA Al-Cu-Mg alloy powder does show slight differences in the water evolution, but significant differences in the hydrogen evolution (Figures 4.35 and 4.36). The hydrogen QMS data of the pure aluminum powder indicates peak related to the decomposition of the trihydrate and monohydrate. As mentioned previously, hydrogen QMS results of the Al-Cu-Mg alloy powder has only one prominent hydrogen peak. There is no indication of decomposition reactions from the trihydrate to the monohydrate and the monohydrate to the anhydrous alumina. The QMS experiments of aluminum-magnesium alloys conducted by other researchers [25] have shown a reaction to occur above 400°C. Davis et al. have attributed the observed reaction to be the formation of MgO, a product of the reaction between the water in

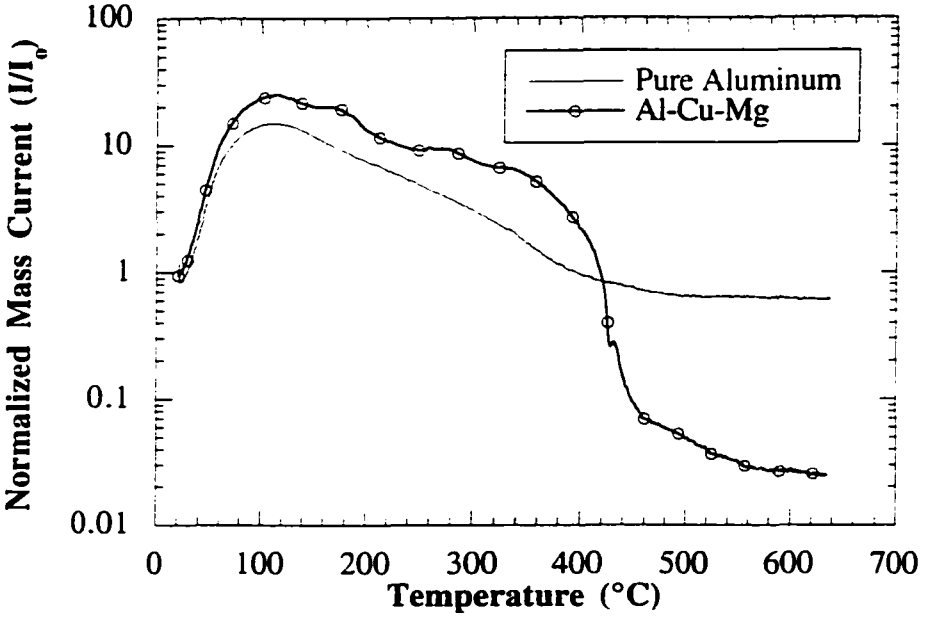

Figure 4.35. Comparison of the QMS water spectra of a SSA pure aluminum powder and a SSA Al-Cu-Mg aluminum alloy powder heated at 5°C per minute.

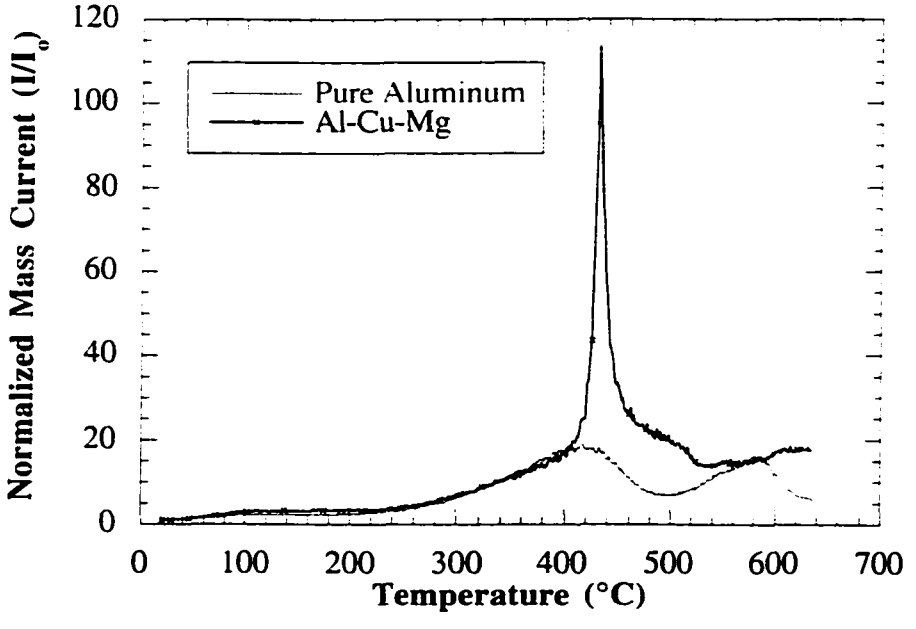

Figure 4.36. QMS hydrogen spectra of SSA pure aluminum powder and a Al-Cu-Mg aluminum alloy powder heated at 5°C per minute.

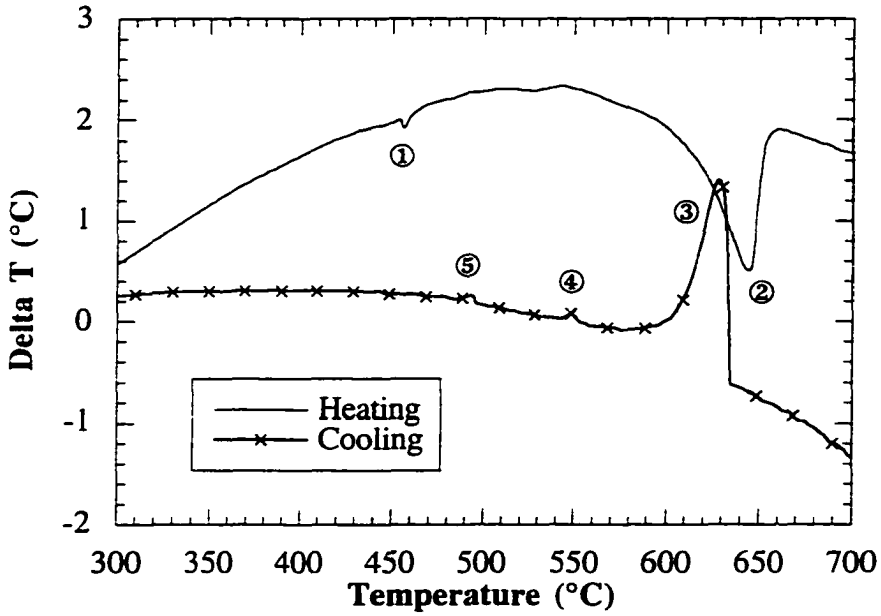

a. Overall DTA trace of Al-Cu-Mg aluminum alloy powder.

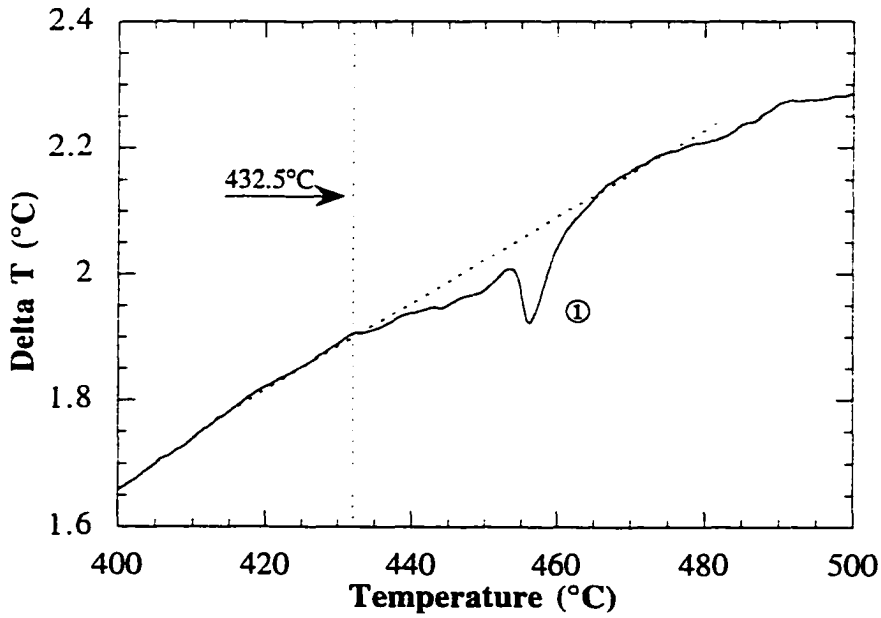

b. Expanded view of DTA trace to highlight peak one.

Figure 4.37. DTA trace of Al-Cu-Mg aluminum alloy powder at 5°C per minute.

the oxide film and the magnesium in the alloy powder.

A DTA scan of the Al-Cu-Mg alloy (Figure 4.37a) powder shows a deviation from the baseline at 432.5°C, indicating a chemical reaction (Figure 4.37b). The measurable DTA reaction temperature corresponds well with the temperature of the hydrogen peak in QMS data (Figure 4.34). The observable deviation immediately precedes an endothermic reaction at 453.2°C which correlates to the aluminum-magnesium solidus of the alloy.

Powder oxidation behavior

Aluminum powders continue to oxide after gas atomization and during post-atomization powder handling [29]. Figure 4.38 illustrates the oxidation that occurs during post-atomization oxidation of the GARS pure aluminum powders in atmospheres with varying levels of humidity. As the figure shows, decreasing the relative humidity appears to decreases the rate of oxidation, indicating the humidity level is a variable in the oxidation of aluminum powders in air [84]. For a given humidity level, the oxidation rate begins to slow after about 300 hours or 12.5 days. To complement the oxidation curves, QMS and AES were conducted on the GARS-9 unexposed and GARS-9 3000 hours exposure samples, exposed at the 15% to 25% humidity levels. For reference purposes in the QMS analysis, the GARS-4 QMS hydrogen was plotted along with the results of the GARS-9 specimens. The unexposed powder has a smaller area under its hydrogen profile than the area under the hydrogen profile of the exposed powder indicating the unexposed powder has less of a hydrated oxide than the exposed powder.

An exposure experiment showing extreme oxidation results is shown in Figure 4.40. Note the significant scale difference between Figure 4.38 and Figure 4.40. The experiment exposed a sample of the GARS-9 pure aluminum powder in a controlled air atmosphere with 85% relative humidity at 29.4°C. The bulk oxygen content of the powder, as measured by IGF, after one day of exposure increases slightly from the unexposed state. After the first

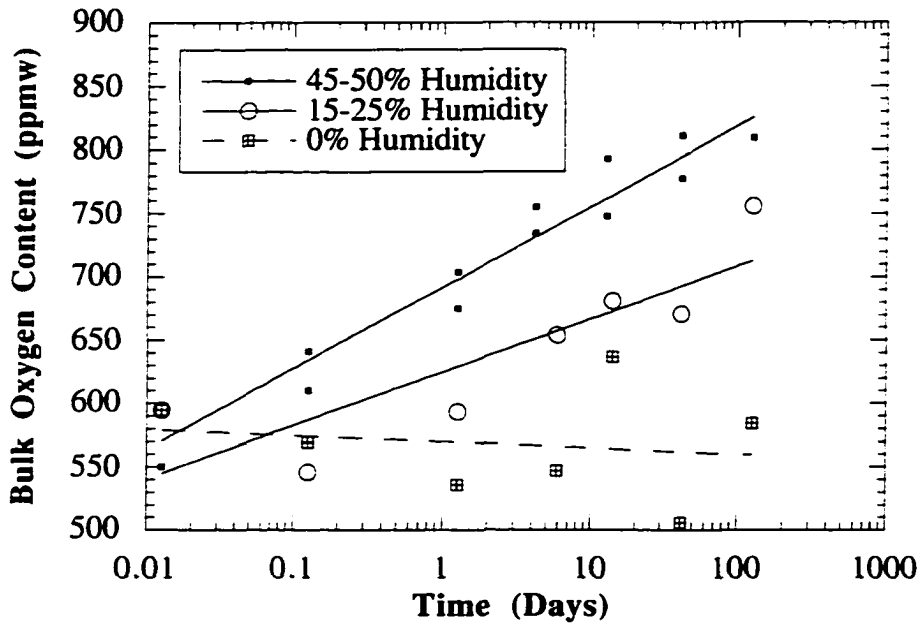

Figure 4.38. Oxidation behavior of GARS pure aluminum powders exposed to air atmosphere with various levels of humidity. The lines are drawn only to guide the eye.

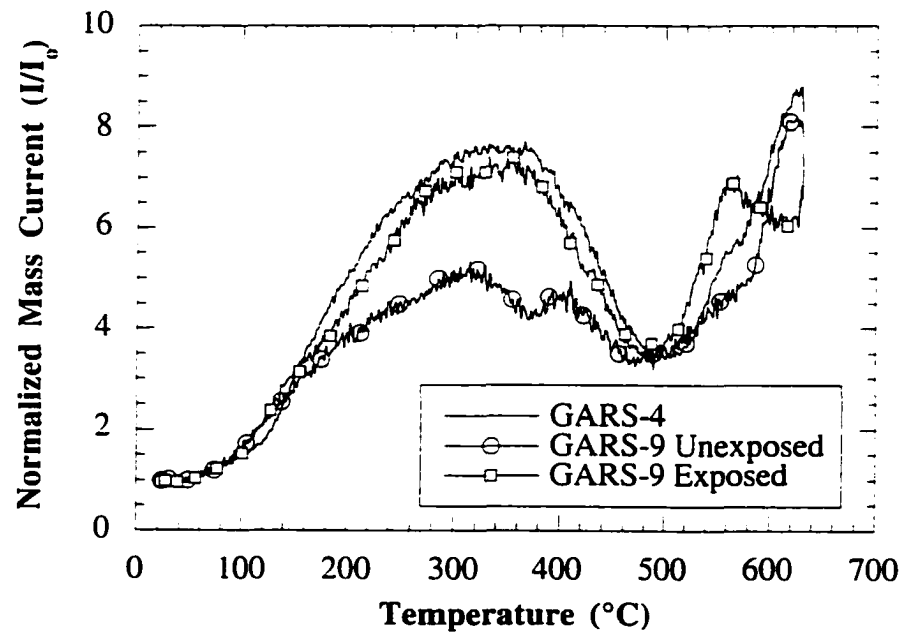

Figure 4.39. QMS hydrogen spectra of GARS-9 aluminum in the unexposed state and exposed for greater than 3000 hours.

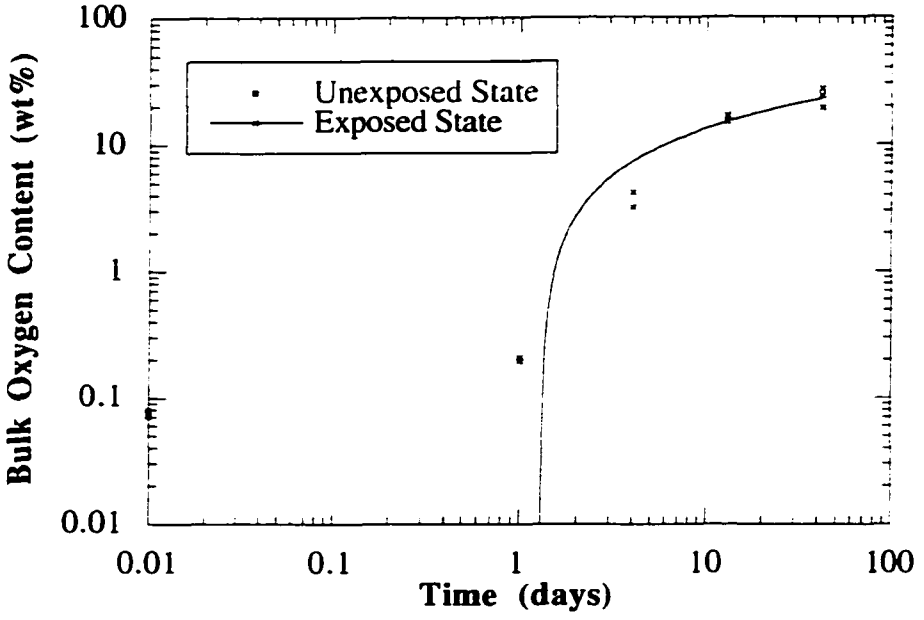

Figure 4.40. Controlled air exposure of aluminum powder in 85% relative humidity at 29.4°C. The line is drawn only to guide the eye.

day of exposure, the bulk oxygen content of the aluminum powder increases at a decreasing rate. The primary source of oxygen from this exposure experiment is from water that is hydrating the oxide film on the aluminum powder particle surfaces.

Since no nitrides were apparently formed in the Al-Ti-Y alloy powder, exposure experiments of the Al-Ti-Y alloy powder were designed to demonstrate the influence of alloying elements on the oxidation behavior of aluminum alloy powders. The exposure experiments were conducted in ambient air at various temperatures over the course of 1000 hours or 41.7 days. Figure 4.41 shows the experimental results of the Al-Ti-Y alloy powder oxidation behavior during various thermal oxidation conditions. The powder samples exposed at 25°C and 162°C have similar oxidation characteristics, i.e., even though the temperature was increased, the oxidation curves are nearly indistinguishable. The oxidation rate of these samples is similar to the GARS-7 and GARS-8 pure aluminum powders exposed to air with 45% to 50% relative humidity. The powders exposed at 300°C start with a greater

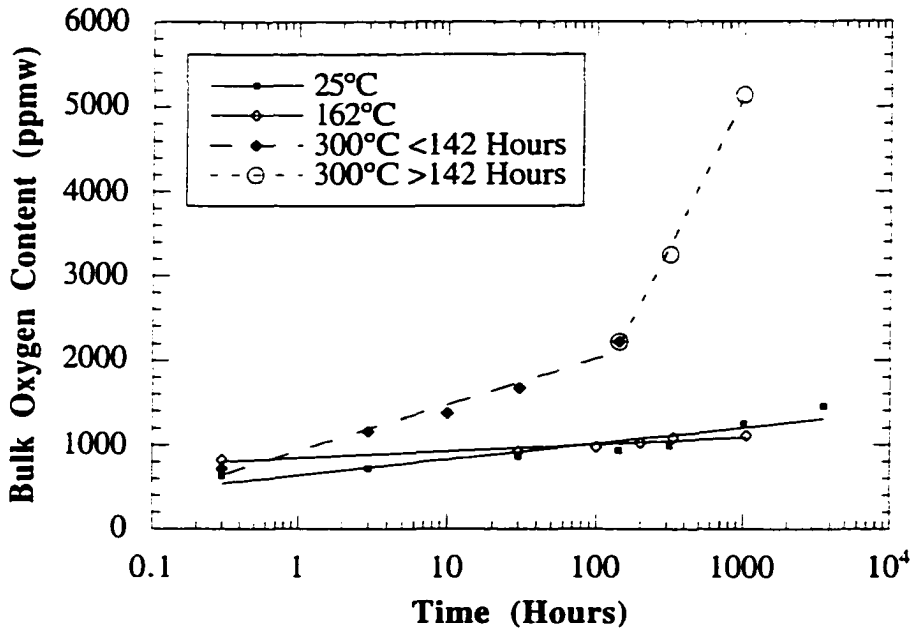

Figure 4.41. Oxidation behavior of Al-Ti-Y alloy powder as exposed to ambient air and different thermal conditions.

oxidation rate than the samples exposed at lower temperatures, which becomes significantly faster at exposure times greater than 142 hours. The rate change is shown as a bend or "knee" in the oxidation curve, indicating a breakaway oxidation mechanism [85].

Figure 4.42 depicts changes of the AES oxide thickness measurements, as a function of exposure time, for the GARS-8 pure aluminum powder and two different thermal oxidation conditions of the Al-Ti-Y alloy powder. As previously mentioned, the GARS-8 and the Al-Ti-Y alloy powder exposed at 25°C have similar oxidation rates. In Figure 4.42, both powder types have similar oxide thicknesses. The oxide film thickness of the Al-Ti-Y alloy powder exposured at 300°C is four to tens times thicker than the same powder exposed at 25°C.

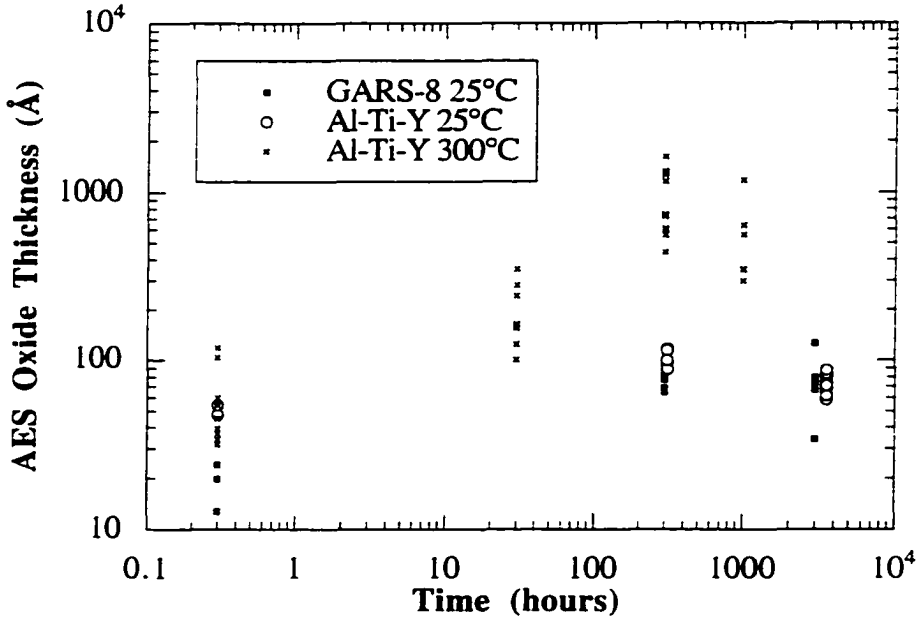

Figure 4.42. AES oxide thickness measurements for aluminum based powders exposed to ambient air at room temperature, nominally 25°C, and 300°C.

Powder explosibility

An evaluation of aluminum powder explosibility indicates the powders susceptibility to an explosion under certain conditions. Figure 4.43 describes the minimum explosibility concentration (MEC) for the GARS, CIGA-ATA, CIGA-VAL, and CAA aluminum powders. All the MEC results shown are to be referenced as "preliminary results" as mentioned on the explosibility report sheets prepared by the Alcoa Specialty Metals Division. The other explosibility tests mentioned in the Chapter 2 are necessary to fully index the explosibility of aluminum powders. The GARS aluminum powders have MEC values greater than 0.06 ounces per cubic foot, but less that 0.120 ounces per cubic foot, which means the powders are in the strong category for explosibility [34]. The commercial powders have MEC values less than 0.06 ounces per cubic foot, implying these powders are in the severe category for explosibility [34].

Figure 4.44 and Table 4.10 shows the MEC results for two different size

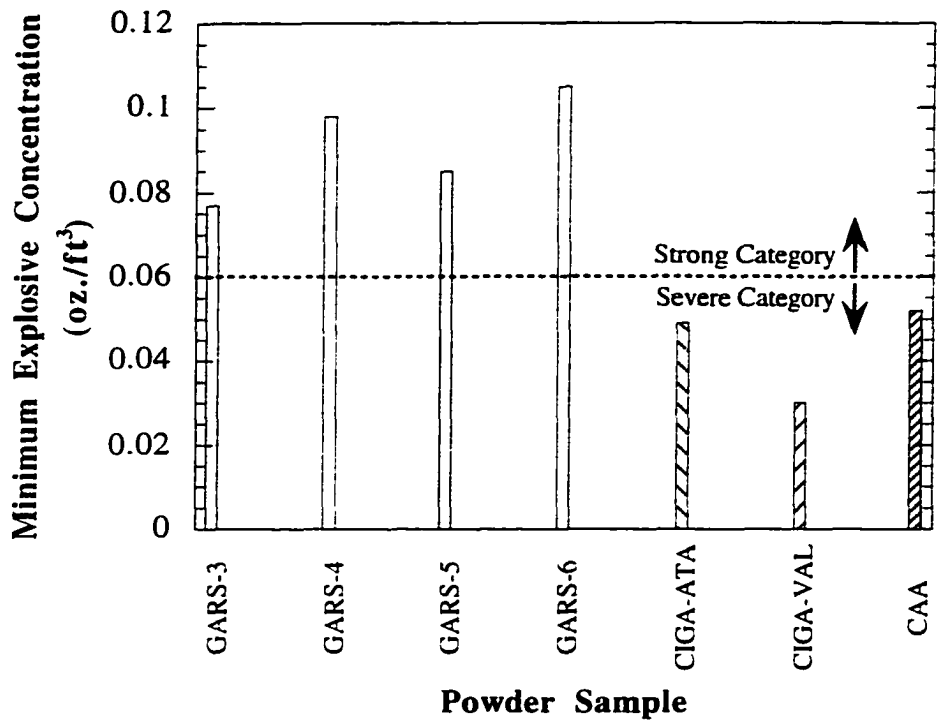

Figure 4.43. MEC data of pure aluminum powders.

classifications of the GARS-9 aluminum powder oxidized in ambient air at 25°C and 300°C. For a given size classification, the powders have similar size distribution percentile points. The experimental designations are explained in Chapter 3. For a given particle size distribution and exposure time, no significant difference of the MEC values was observed between a sample exposed at 25°C and 300°C. The normalized bulk oxygen content as a function of exposure time (Figure 4.45) shows that the rate of oxidation for a specific powder size increases as the exposure temperature rises.

The increasing oxygen content with time would indicate the oxide film thickness also increases with exposure time and temperature. As may be noted in Table 4.11, the oxide thickness measured by AES does increase. After ten hours of air exposure at 25°C, the -38/10/25 powder sample had an average AES oxide thickness of 50.4±11.1 Å. With increasing exposure time and temperature, the average AES oxide thickness for the -38/100/300 powder sample increased to 81.4±8.4 Å. After 1000 hours of air exposure at

300°C, the average AES oxide film thickness for the -38/1000/300 powder sample increased significantly to 225.4±21.0 Å. All oxide thicknesses resulted in an unchanged MEC.

The attempt to show how oxide thickness differences may influence the explosibility of a GARS powder were inconclusive. The MEC test may not be sensitive to changes in the oxide film thickness. However, the tests did confirm that a reduced surface area decreased the explosibility of GARS aluminum powder. In fact, the MEC values of the coarse GARS powder were in non-explosive category [34].

Table 4.10. Powder size characteristics of GARS-9 aluminum powder used for MEC testing.

MEC Powder Sample	Specific Surface Area of Powder (m^2/g)	Size Distribution Percentile Points		
		d_{16} (μm)	d_{50} (μm)	d_{84} (μm)
-38/10/25	0.136	11.33	22.12	37.00
-38/10/300	0.133	11.32	22.42	37.45
-106+75/10/25	0.046	32.86	70.63	110.69
-106+75/10/300	0.051	29.37	64.57	112.17
-38/100/25	0.133	11.33	22.22	37.60
-38/100/300	0.122	12.44	24.05	39.67
-106+75/100/25	0.045	32.52	68.84	111.50
-106+75/100/300	0.043	35.46	71.41	111.71
-38/1000/25	0.129	11.82	22.81	37.66
-38/1000/300	0.137	11.05	21.62	36.81
-106+75/1000/300	0.047	32.07	67.89	111.15
-106+75/1000/300	0.043	35.01	71.77	114.82

Table 4.11. MEC, specific surface area, and average AES oxide film thickness values for powders shown in Figure 4.44.

MEC Powder Sample	Specific Surface Area of Powder (m^2/g)	Average AES Oxide Film Thickness (Å)	MEC value ($oz./ft^3$)
-38/10/25	0.136	50.4±11.1	0.105
-38/10/300	0.133	Indeterminate	0.090
-106+75/10/25	0.046	Not Measured	0.813
-106+75/10/300	0.051	Not Measured	0.813
-38/100/25	0.133	Not Measured	0.105
-38/100/300	0.122	81.4±8.4	0.105
-106+75/100/25	0.045	Not Measured	0.813
-106+75/100/300	0.043	Not Measured	0.813
-38/1000/25	0.129	Not Measured	Not Measured
-38/1000/300	0.137	225.4±21.0	0.107
-106+75/1000/300	0.047	Not Measured	Not Measured
-106+75/1000/300	0.043	Not Measured	Not Measured

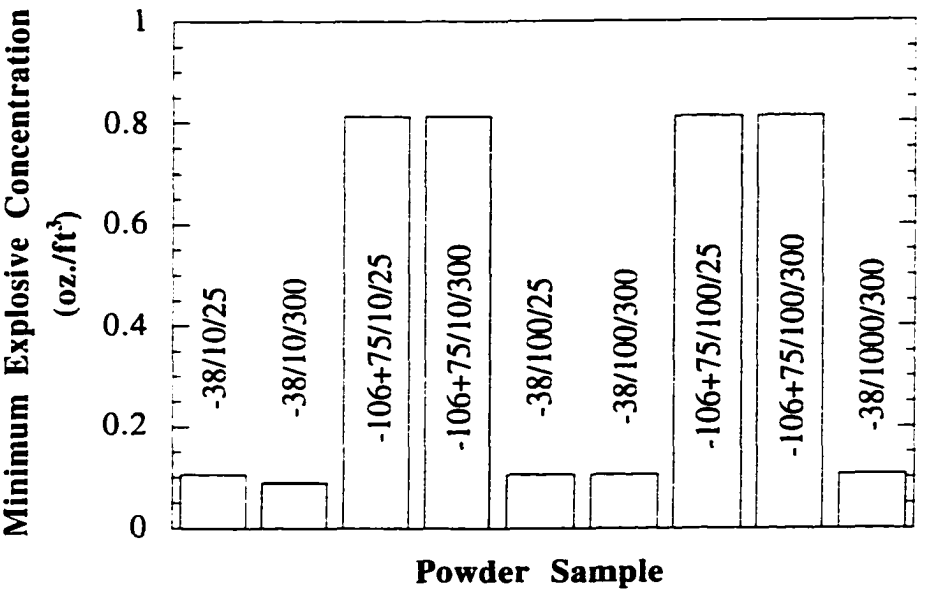

Figure 4.44. MEC data of GARS-9 aluminum powder.

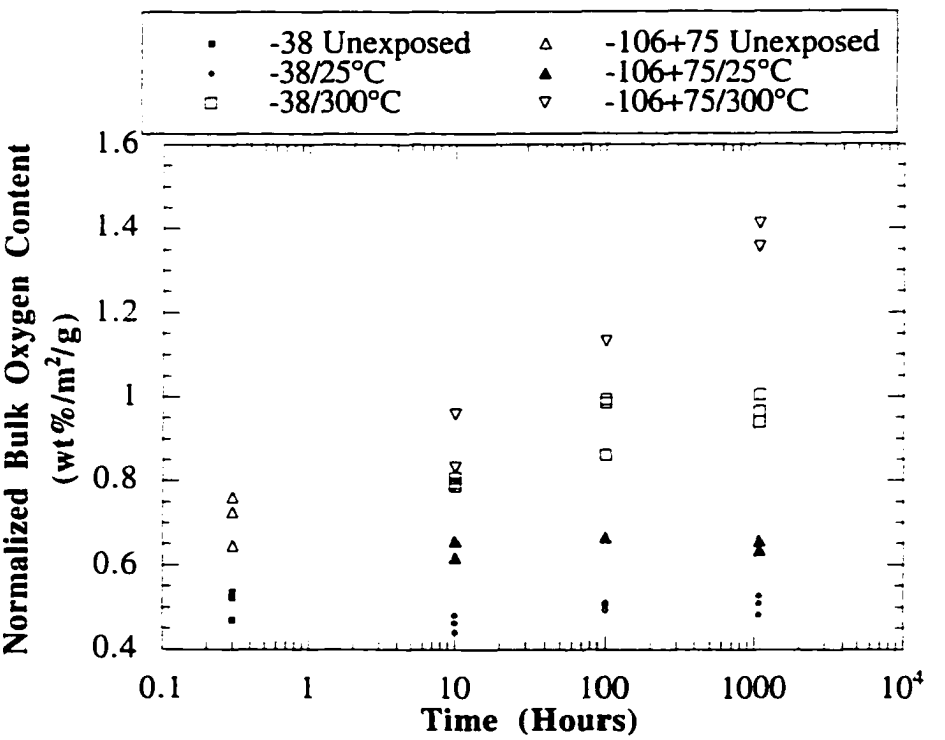

Figure 4.45. Normalized oxygen content of GARS-9 aluminum powders used for MEC experiment.

Powder Consolidation

Air sintering of aluminum powders

Samples of the GARS-9 and CAA aluminum powders were sintered in air to demonstrate the dependence of oxide film thickness on sintering behavior of aluminum powders. This experiment was conceived after observing indications of solid state sintering with the heat treated, GARS-9, aluminum powder samples tested for MEC. After air sintering for twenty-four hours at 300°C, the GARS-9 aluminum powder qualitatively had better green strength than the CAA aluminum powder. The green strength of the CAA aluminum powder is wholly due to mechanical interlocking of the irregular shaped powder particles. Macroscopic photographs show the as-sintered cakes (Figure 4.46 and Figure 4.47). The reason for the improved green strength of the GARS-9 aluminum powder, over the CAA aluminum powder, is due to sintered neck formations between the GARS-9 aluminum powder particles, as shown in Figure 4.49. The CAA powder had no observable sintered neck formations between the powder particles (Figure 4.48).

CIP-VHD-HIP and CIP-VCD-HIP consolidation

The GARS-4 and CAA aluminum powders were consolidated by the CIP-VHD-HIP and CIP-VCD-HIP consolidation paths to observe the microstructural developments of each powder type during the different consolidation routes. The progression of densification from the CIP consolidation through the HIP consolidation of the GARS-4 and CAA aluminum powders is apparent by the bulk densities listed in Table 4.12. The CIP green densities of the GARS-4 and the CAA aluminum powders, at the same CIP pressure, are 93.34% and 89.66%, respectively, of the pycnometry density of each aluminum powder. Figure 4.50

Table 4.12. Bulk densities of GARS-4 and CAA aluminum powders during different stages of powder consolidation.

Powder Sample	CIP (%)	CIP-VHD-HIP (%)	CIP-VCD-HIP (%)
GARS-4	93.34	96.89	99.19
CAA	89.66	97.56	99.07

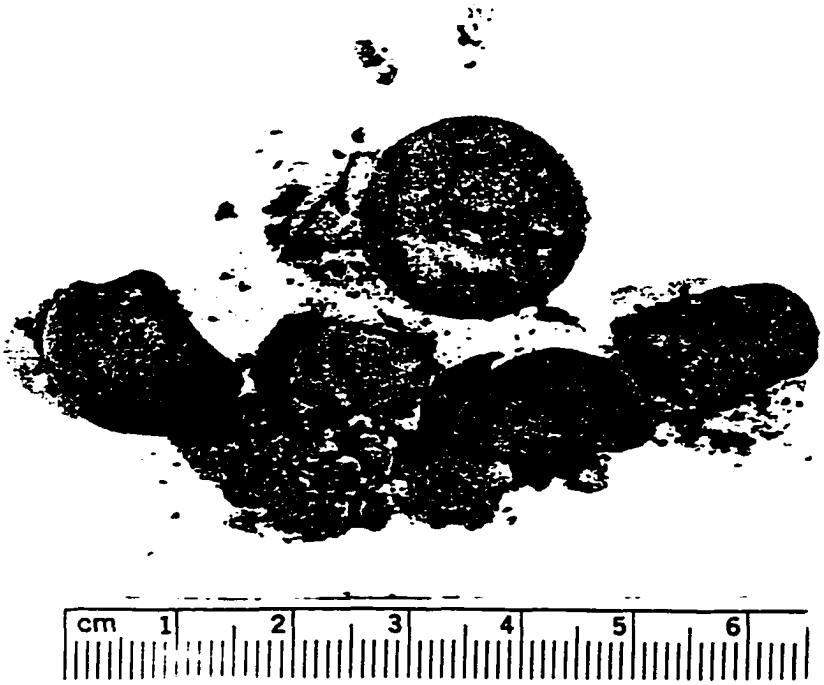

Figure 4.46. Photograph of CAA aluminum powder air sintered at 300°C for 24 hours.

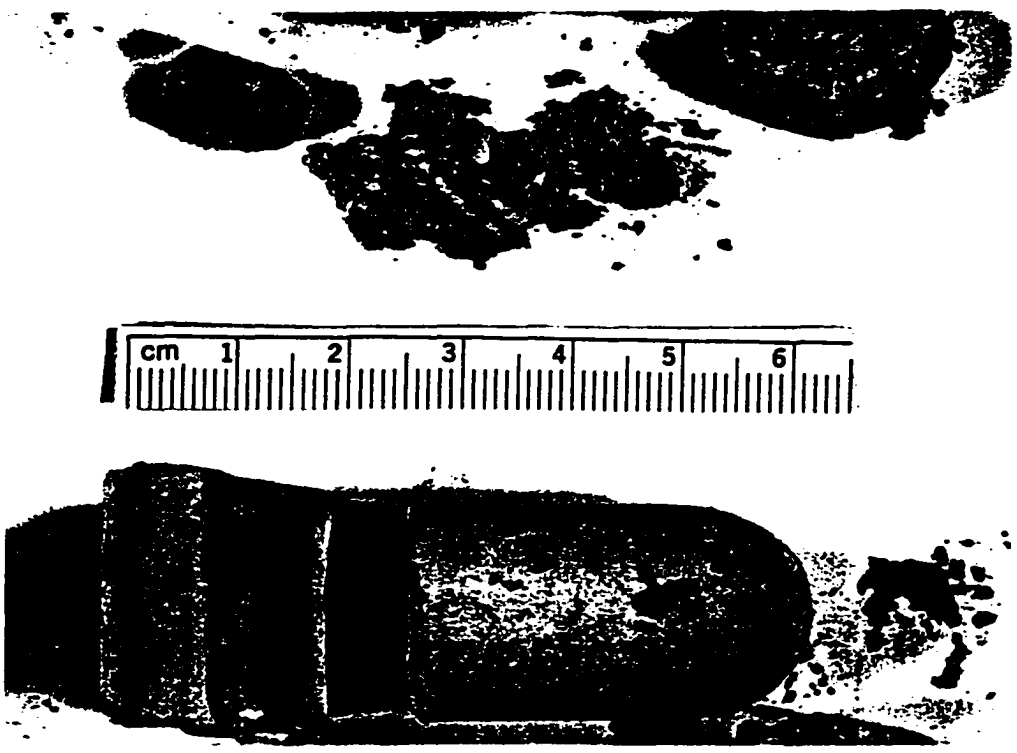

Figure 4.47. Photograph of GARS aluminum powder air sintered at 300°C for 24 hours.

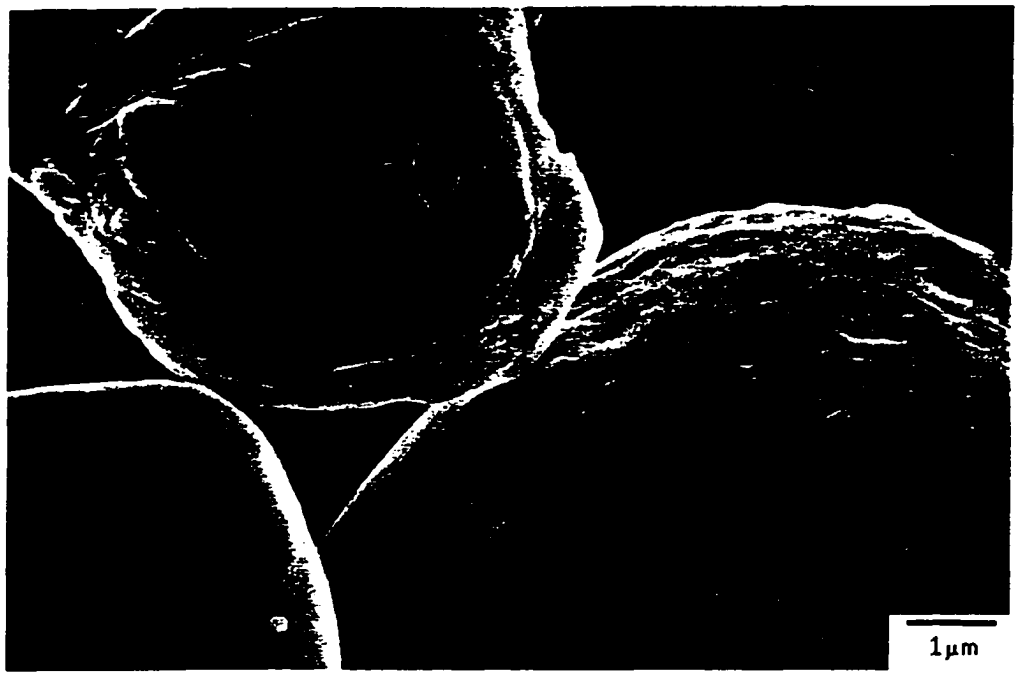

Figure 4.48. SEM micrograph of the CAA aluminum powder air sintered at 300°C for 24 hours.

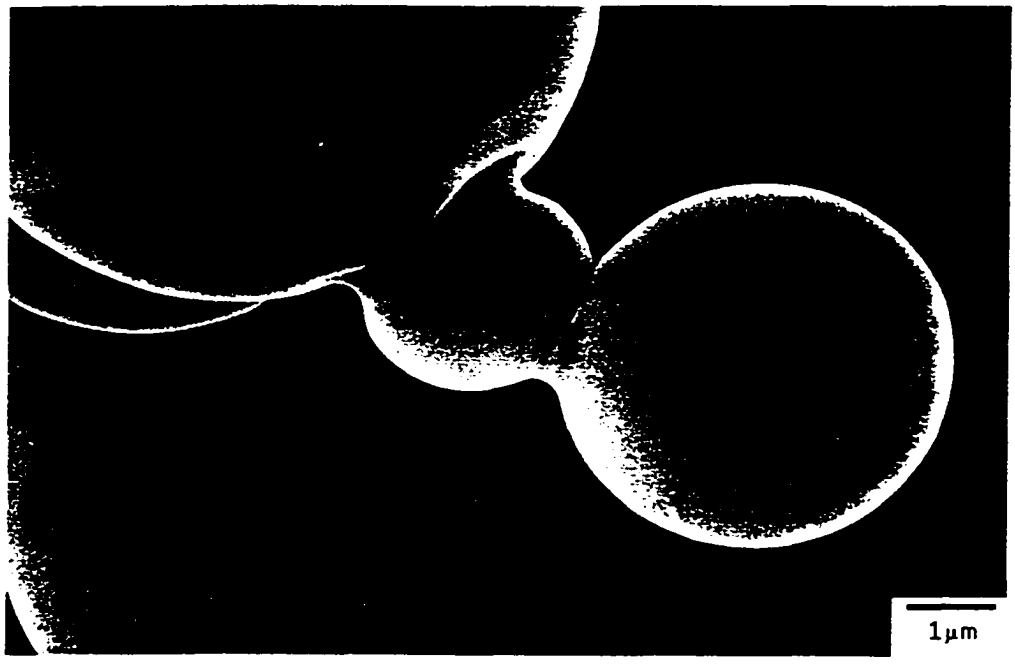

Figure 4.49. SEM micrograph of the GARS aluminum powder air sintered at 300°C for 24 hours.

and Figure 4.51 show the CIP microstructures of the CAA and GARS-4 aluminum powders in the as-polished, unetched condition . The density differences are apparently due to compressibility differences of the aluminum powders, which may occur because of oxide film thickness differences [46]. Recall, the AES oxide film thickness of the CAA aluminum powder is about four to five times greater than the GARS-4 AES oxide film thickness, refer to Figure 4.22.

Figures 4.52 and 4.54 record the CIP-VCD-HIP microstructure of the GARS-4 and CAA aluminum powders, respectively. Figures 4.53 and 4.55 document the microstructures of the same powders processed by the CIP-VHD-HIP consolidation sequence. The CIP-VHD-HIP microstructures qualitatively have more apparent porosity than the CIP-VCD-HIP microstructures, note the arrows pointing to the points of porosity on the CIP-VHD-HIP microphotographs. A similar trend is observed with the measured bulk densities of the consolidated samples after the HIP cycle. The CIP-VCD-HIP samples are more dense than the CIP-VHD-HIP samples.

Pieces of the consolidated samples were analyzed with QMS at 5°C per minute. Table 4.13 lists the relative areas under the hydrogen profiles for each sample tested. For these experiments, the area under the hydrogen curve is proportional to the relative amount of hydrated oxide remaining after each consolidation procedure. For a given consolidated powder sample, the relative quantity of hydrogen evolution from as-atomized powder is greater than the VCD sample, which is greater than the amount of hydrogen evolving from the VHD sample (Figure 4.56 and Figure 4.57).

Table 4.13. Relative areas under the hydrogen profiles of the CAA and GARS-4 powder samples in Figure 4.56 and Figure 4.57, respectively.

QMS Sample	Relative Area
GARS-4 (Powder)	2399
GARS-4 (VCD-HIP)	2246
GARS-4 (VHD-HIP)	995
CAA (Powder)	4835
CAA (VCD-HIP)	3055
CAA (VHD-HIP	838

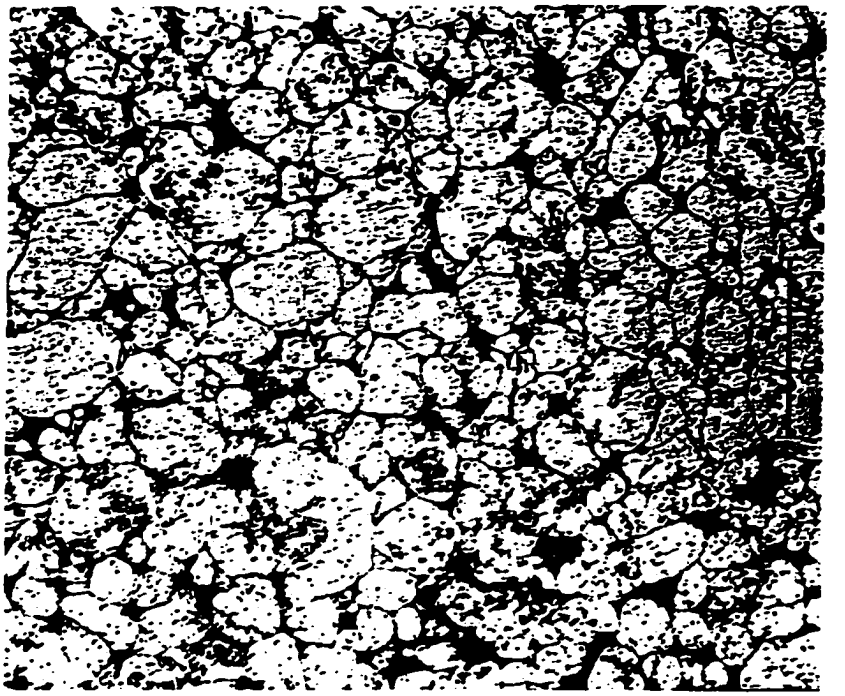

Figure 4.50. Optical micrograph of the as-polished, unetched, CIP microstructure of CAA aluminum powder.

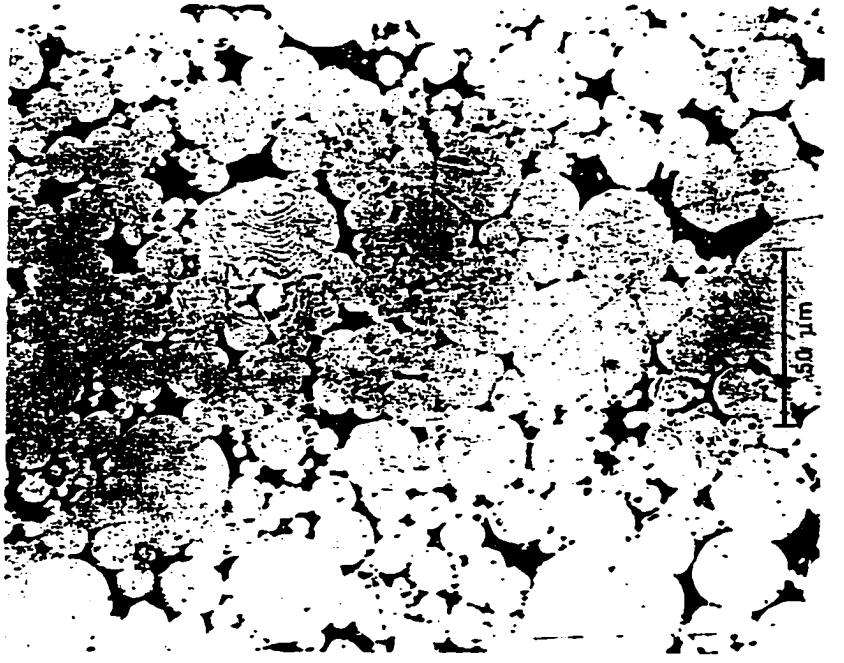

Figure 4.51. Optical micrograph of the as-polished, unetched, CIP microstructure of the GARS aluminum powder.

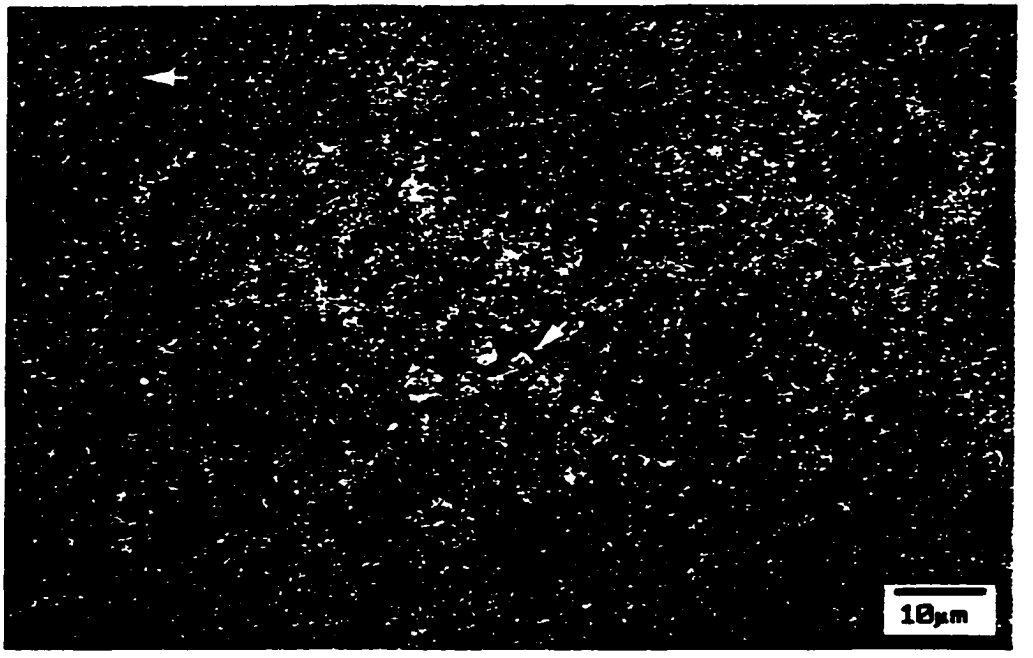

Figure 4.52. SEM micrograph showing the CIP-VCD-HIP microstructure of the CAA aluminum powder. The white arrows indicate the residual porosity in the sample.

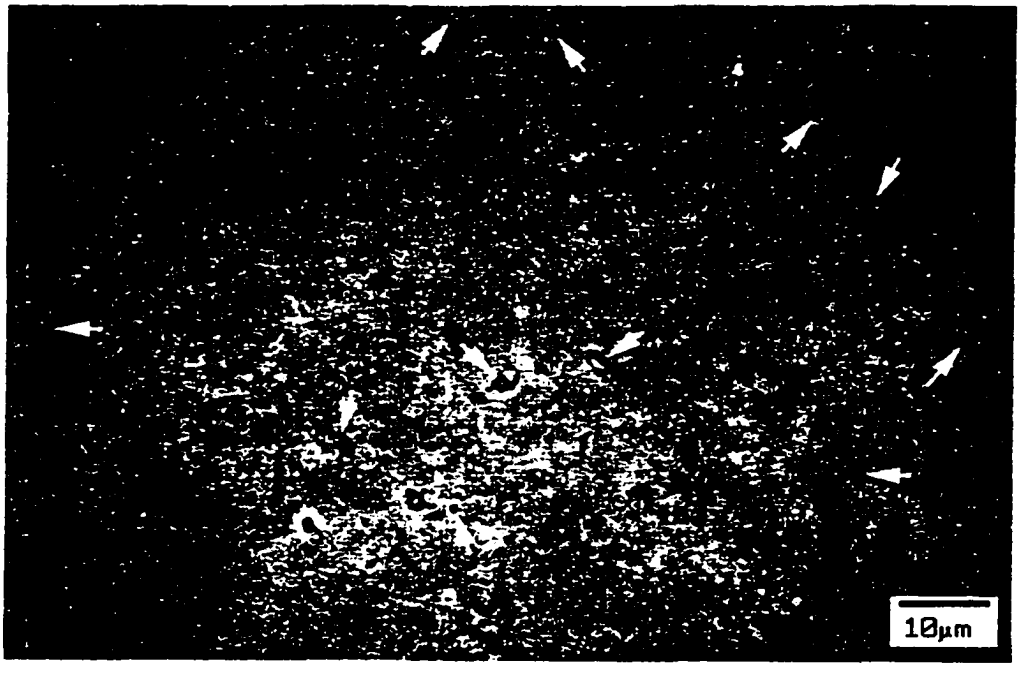

Figure 4.53. SEM micrograph showing the CIP-VHD-HIP microstructure of the CAA aluminum powder. The white arrows indicate the residual porosity in the sample.

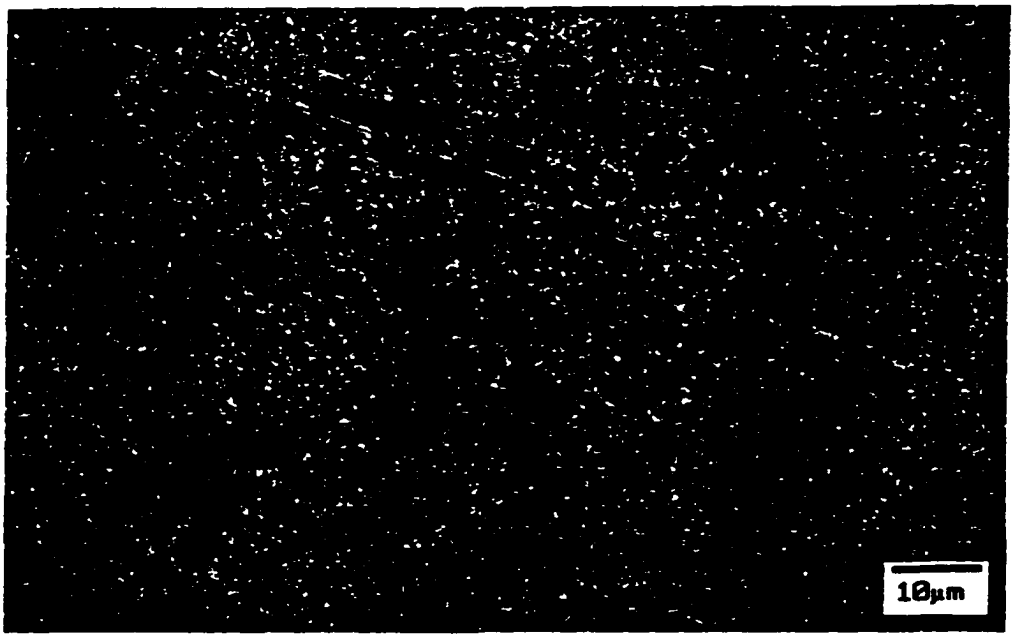

Figure 4.54. SEM micrograph showing the CIP-VCD-HIP microstructure of the GARS aluminum powder. No residual porosity is observed in the sample.

Figure 4.55. SEM micrograph showing the CIP-VHD-HIP microstructure of GARS aluminum powder. The white arrows indicate the residual porosity in the sample.

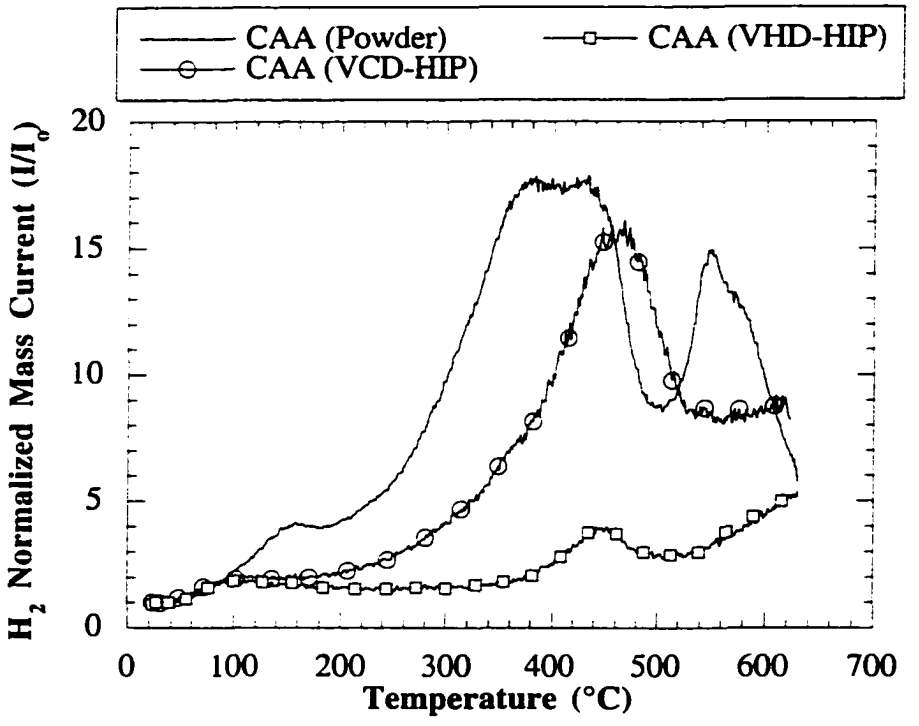

Figure 4.56. QMS results of the CAA powder samples comparing the as-atomized powder to the CIP-VHD-HIP and CIP-VCD-HIP consolidated samples.

To complement the QMS evaluations of the GARS-4 and CAA powders and consolidated samples, the hydrogen content of the samples (Table 4.14) was measured using a vacuum extraction technique developed by Peterson et al. [33]. Two reference points are given for comparison with the measured hydrogen results of the powder and consolidation samples, the equilibrium solubility of hydrogen gas in molten aluminum at 950°C, 2.45 ppmw [86], and the measured hydrogen content of the Alcoa pure aluminum ingot. For each powder type, the same trend observed in the QMS data, with respect to the areas under the hydrogen profiles, is confirmed by the hydrogen chemistry. The hydrogen content of the as-atomized powder state is greater than the CIP-VCD-HIP sample, which is greater than the CIP-VHD-HIP sample. The change in the hydrogen content from the Alcoa ingot to the GARS-4 powder is due to melting of the ingot in the atomization melt chamber, i.e., the diffusion of hydrogen out of the melt to achieve an equilibrium hydrogen content in the aluminum melt.

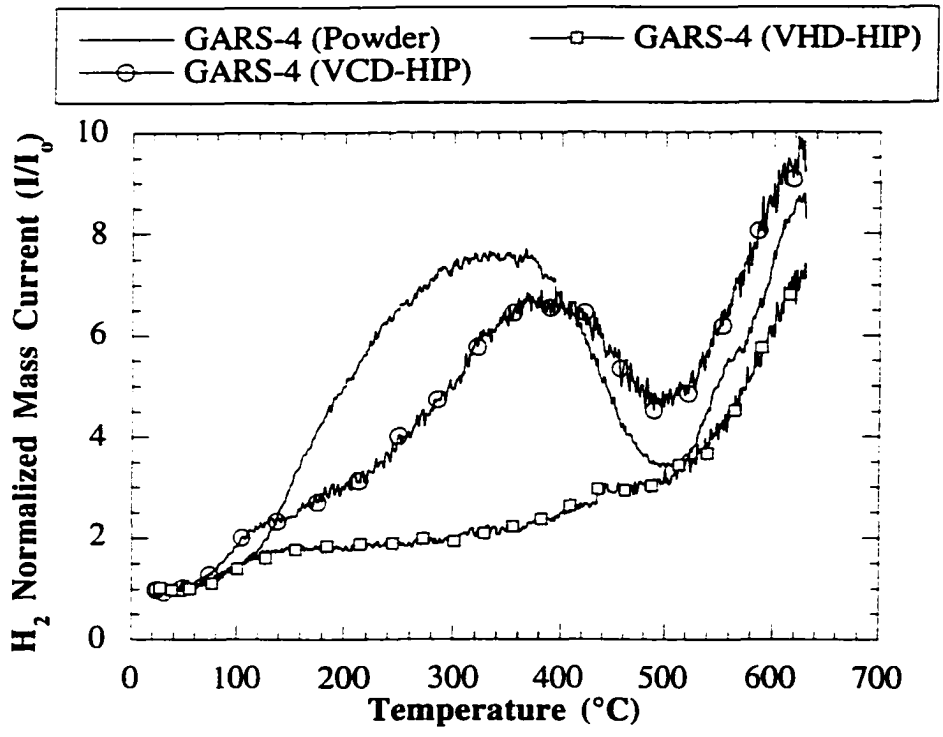

Figure 4.57. QMS results of the GARS-4 powder samples comparing the as-atomized powder to the CIP-VHD-HIP and CIP-VCD-HIP consolidated samples.

The hydrogen values, though, may be artificially high, particularly for the as-atomized powder samples, because water vapor may have been extracted from the samples, in addition to hydrogen, during the hydrogen vacuum extraction analyses. A review of the water signals from the QMS analyses of the as-atomized powders and the consolidated samples (Figure 4.58 and Figure 4.59) does show water vapor evolving from the samples under vacuum conditions. In view of the QMS results, water vapor does contribute to the gas volume collected in the collection volume during the vacuum extraction analysis. Depending on the sample, i.e., degassed powder versus non-degassed powders, the contribution of the

Table 4.14. Hydrogen content of pure aluminum samples as measured by vacuum extraction.

Sample	99.999% Al Ingot	GARS-4 Powder	GARS-4 VCD-HIP	GARS-4 VHD-HIP	CAA Powder	CAA VCD-HIP	CAA VHD-HIP
H (ppmw)	30.5	20.7	13.9	9.1	94.8	17.6	10.3

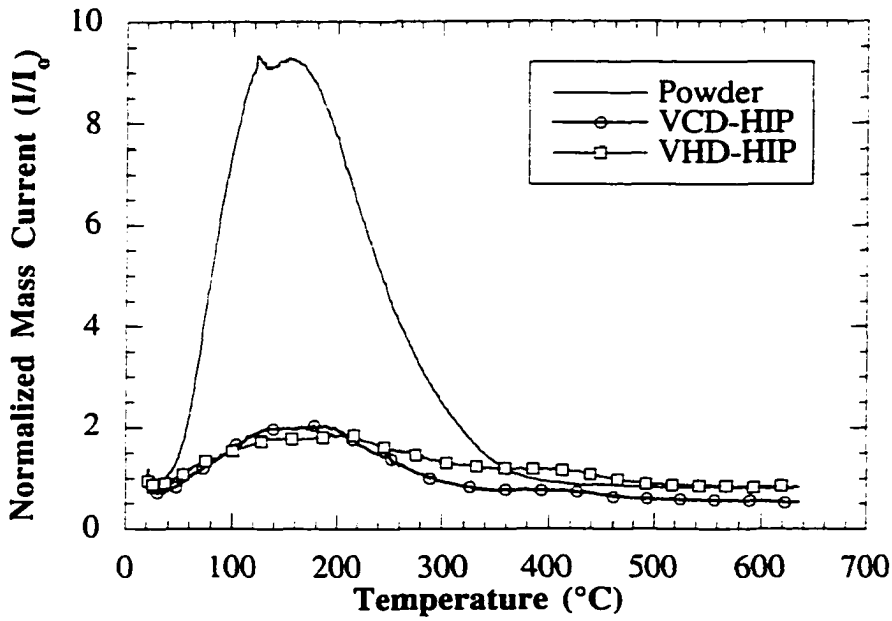

Figure 4.58. QMS results of water evolution from GARS-4 powder samples in the as-atomized powder state and consolidated states.

water vapor partial pressure to the total pressure measured would probably decrease for powder samples degassed prior to the hydrogen vacuum extraction analysis. After degassing the powder, the measured hydrogen values would better reflect the amount of hydrogen in the consolidated sample.

Heat treatment of CAA consolidated samples

The porosity differences between the non-heat treated and heat-treated CAA CIP-VCD-HIP samples was not readily apparent from microstructure, i.e., there was no means to physically distinguish between any pores created before and after heat treating at 300°C and 550°C. With the aid of QMS, though, a distinction between the different heat treatments did occur, Table 4.15 lists the relative areas under the hydrogen profiles shown in Figure 4.60. The as-atomized CAA powder sample is given for reference purposes.

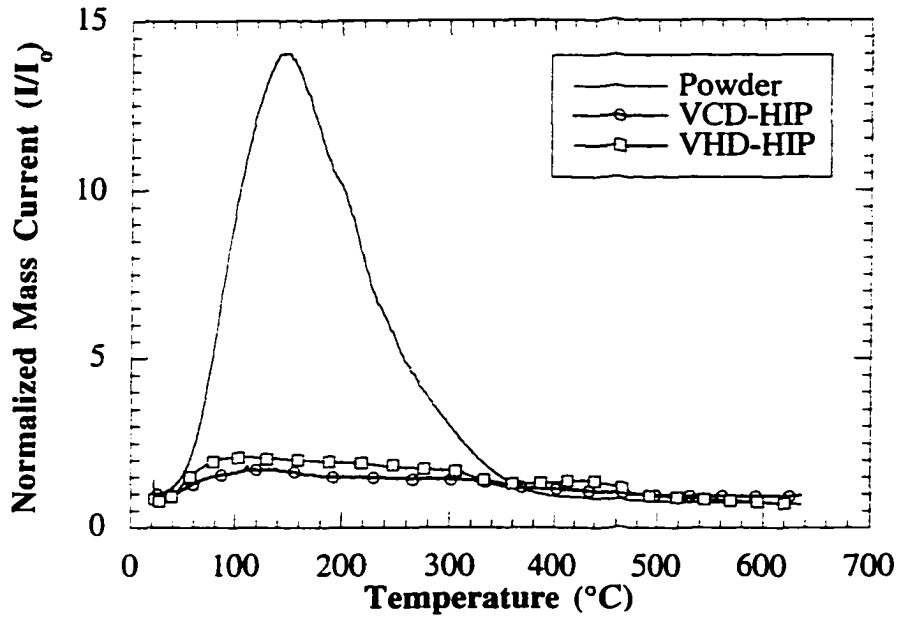

Figure 4.59. QMS results of water evolution from CAA powder samples in the as-atomized powder state and consolidated states.

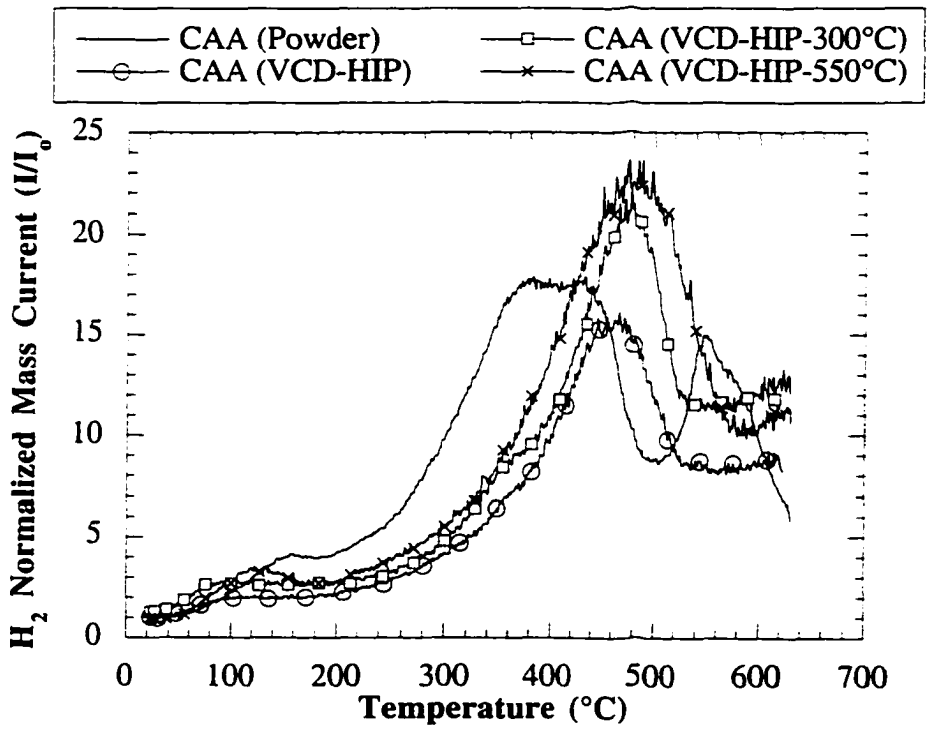

Figure 4.60. Effect of heat treating temperature on CIP-VCD-HIP CAA powder samples.

Table 4.15. Relative areas under the hydrogen profiles for the samples shown in Figure 4.60.

QMS Sample	Relative Area
CAA Powder	4835
CAA VCD-HIP	3055
CAA VCD-HIP-300°C	4317
CAA VCD-HIP-550°C	4888

Punch Test

The punch test provides structure-property relationships for the CIP-VHD-HIP and CIP-VCD-HIP consolidated samples. Before mechanically loading a punch test coupon, it has the shape of a flat disk. After punch testing a ductile material, such as the aluminum specimens tested for this research, the geometry of the coupon has a "hat" shape (Figure 4.62). The observed cracks are due to an overloading condition of the sample, i.e., the region of negative slope on the load-deflection curve in Figure 4.61, corresponding to a decrease of the applied load on the punch test curve at deflection values greater than δ_f. The fracture surface of the cracks shows microstructural tearing or shear mode of failure (Figure 4.63).

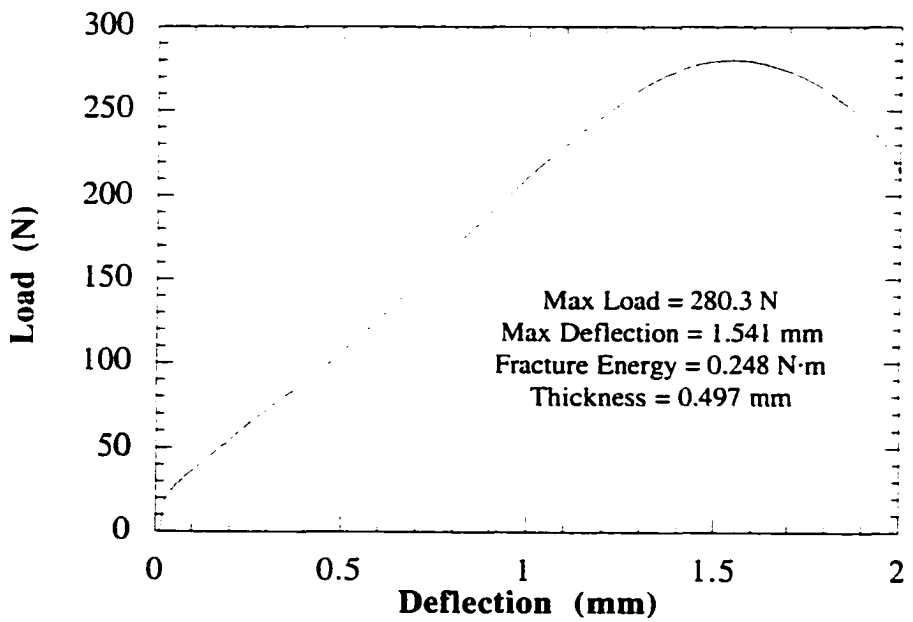

Figure 4.61. An example punch test plot of a consolidated CAA aluminum powder, illustrating the nearly ideal behavior of the consolidated powders samples during the punch test.

A summary of the measurable mechanical properties of the CIP-VCD-HIP and CIP-VCD-HIP samples is in Figures 4.64, 4.65, and 4.66. The results shown in these figures only provide a comparative analysis of the CIP-VCD-HIP and CIP-VCD-HIP consolidation sequences for a given powder type. In each figure, the corresponding punch test value of the Alcoa pure aluminum ingot is provided for a point of reference. The punch test results would be expected to depend on the prior particle size, pore structure, pore volume, and bulk chemistry of the coupon tested.

For a given powder type, the yield stress results statistically show little or no difference between the CIP-VHD-HIP and CIP-VCD-HIP consolidation methods . However, the yield stress variances between the GARS, CIGA-ATA and CAA aluminum powders are due to differences in the powder particle size and bulk chemistry of each aluminum powder. In general, the yield stress of a metal is directly dependent on the reciprocal square root of the grain size and directly proportional to increases in the alloy chemistry of the metal [87]. For the consolidated microstructures evaluated in this portion of the research, the grain size of each consolidated powder sample is assumed to equal the d_{84} powder size for each powder type.

The GARS consolidated samples have the lowest yield stress of all three powder types, because of a larger d_{84} powder size (Table 4.1) and a more pure bulk chemistry (Table 4.4) than the CIGA-ATA and CAA aluminum powders. The yield stress of the CAA powder is slightly greater than the GARS aluminum powder, because of the slightly smaller d_{84} powder size (Table 4.1) and less pure bulk chemistry (Table 4.4). The CIGA-ATA consolidated samples have the largest yield stress values of all three powder types, because these samples have the smallest d_{84} powder size (Table 4.1) and relatively impure chemistry (Table 4.4). The fracture strain values of all the aluminum powder samples are nearly the same, irregardless of powder type and processing conditions. However, the fracture energy values closely follow the rises and falls of the yield stress data, implying that the fracture

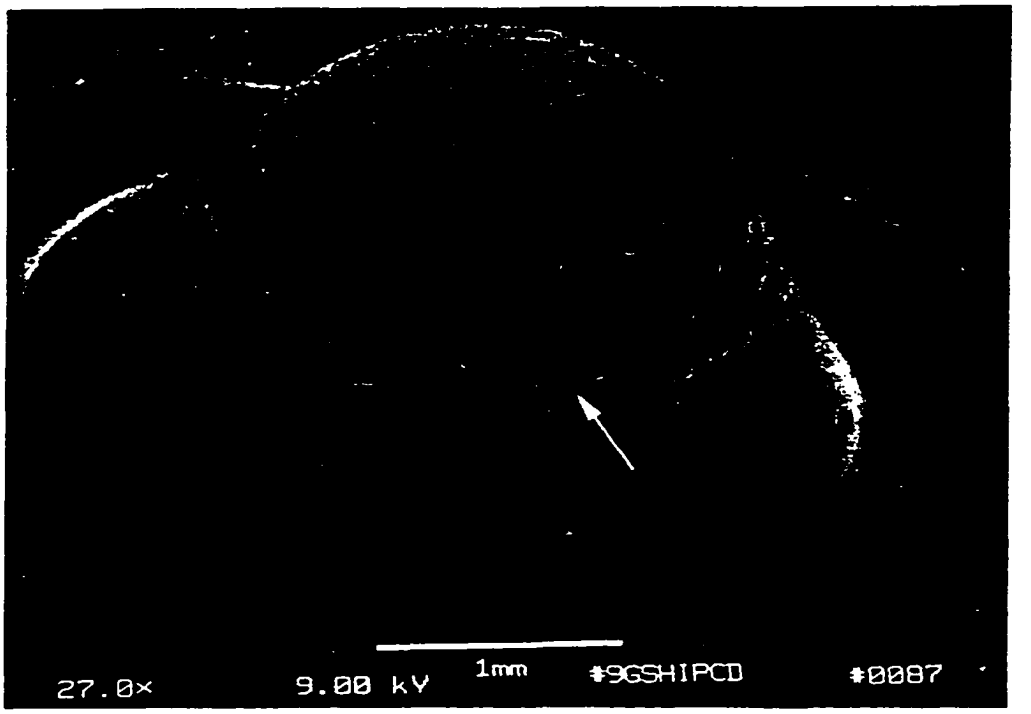

Figure 4.62. SEM micrograph of a punch test coupon after testing. The white arrow indicates the area shown in Figure 4.62, below.

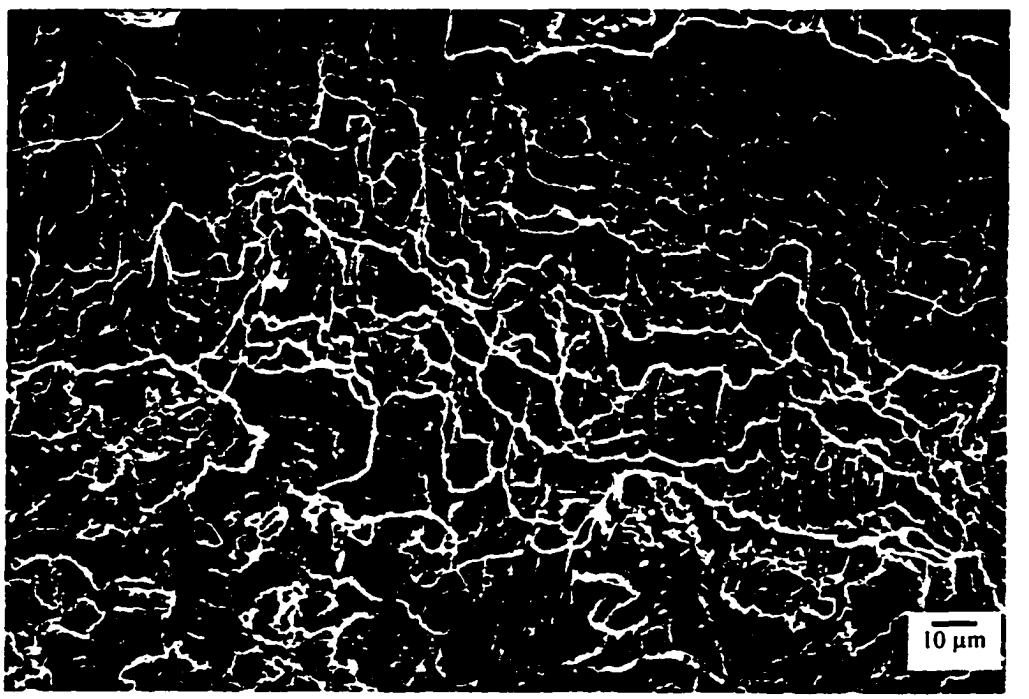

Figure 4.63. SEM micrograph showing the typical fracture surface formed during punch testing of the aluminum powder punch test coupons.

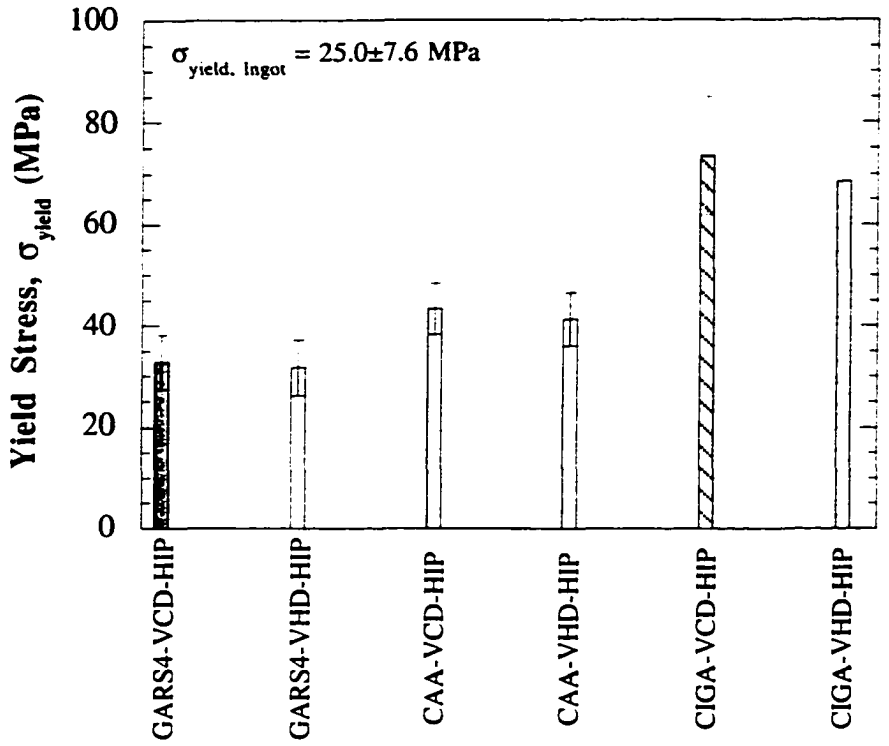

Figure 4.64. Yield stress results from punch testing the GARS-4, CAA, and CIGA-ATA aluminum powders consolidated by CIP-VCD-HIP and CIP-VHD-HIP routes.

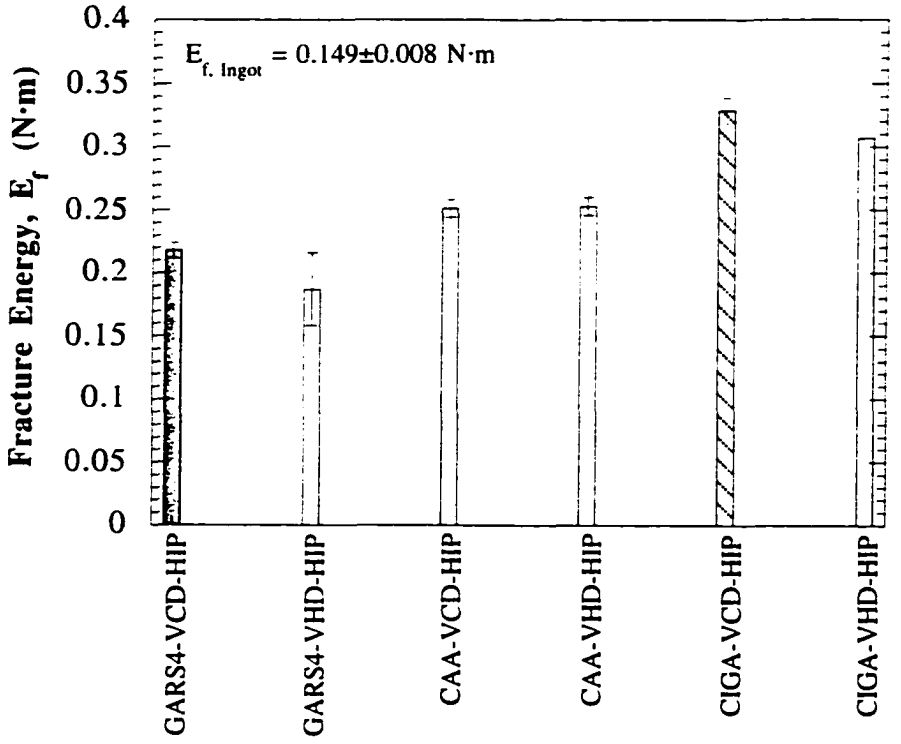

Figure 4.65. Fracture energy results from punch testing the GARS-4, CAA, and CIGA-ATA aluminum powders consolidated by CIP-VCD-HIP and CIP-VHD-HIP routes.

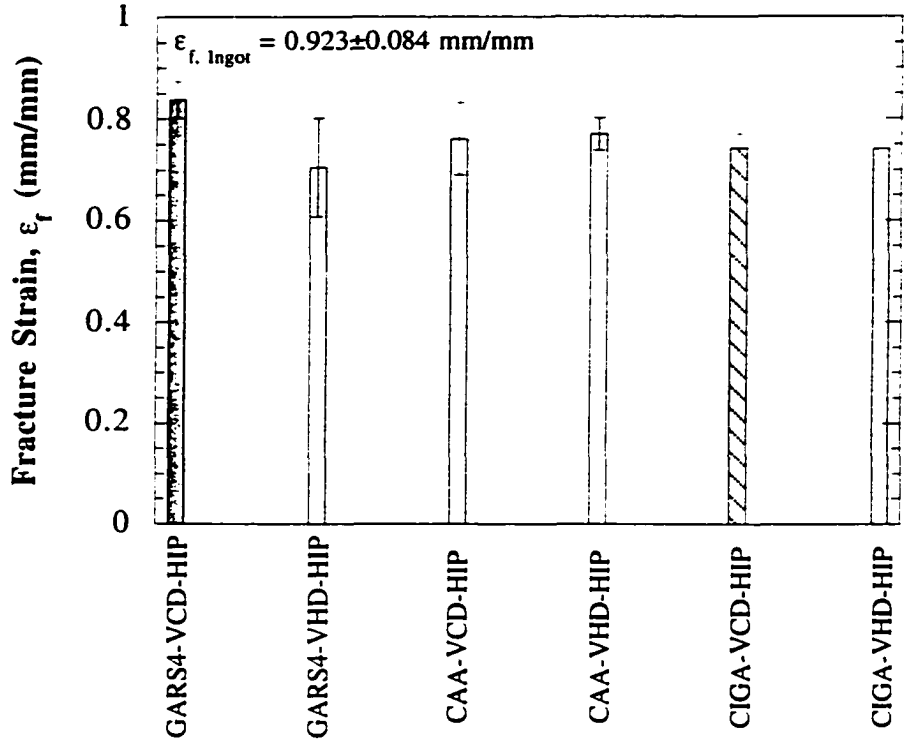

Figure 4.66. Fracture strain results from punch testing the GARS-4, CAA, and CIGA-ATA aluminum powders consolidated by CIP-VCD-HIP and CIP-VHD-HIP routes.

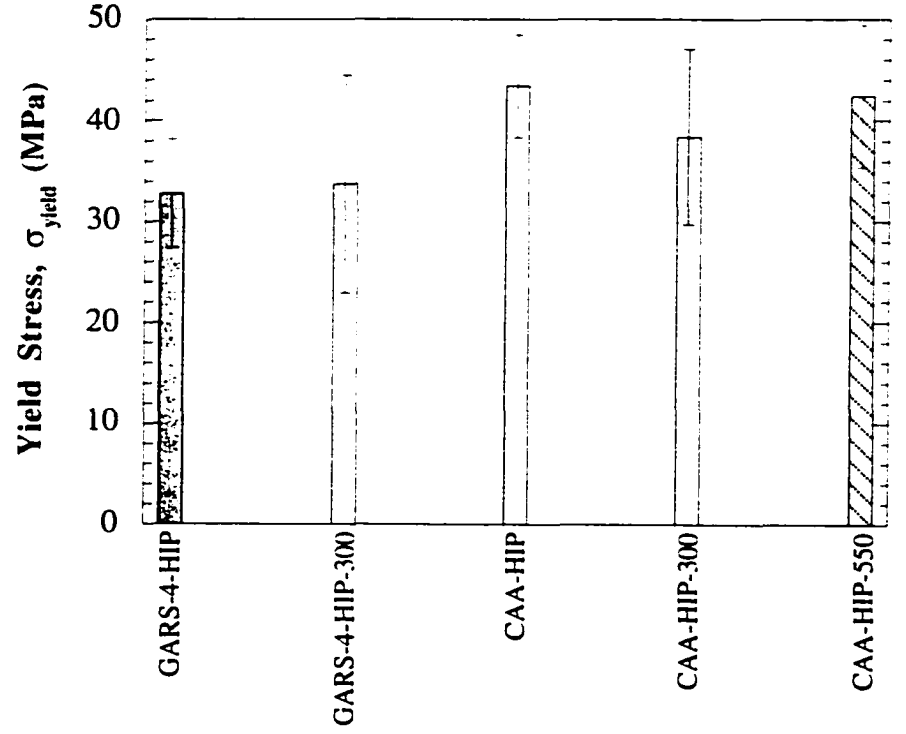

Figure 4.67. The effect of heat treatment on the yield stress properties of the GARS-4 and CAA aluminum powders consolidated by the CIP-VCD-HIP route.

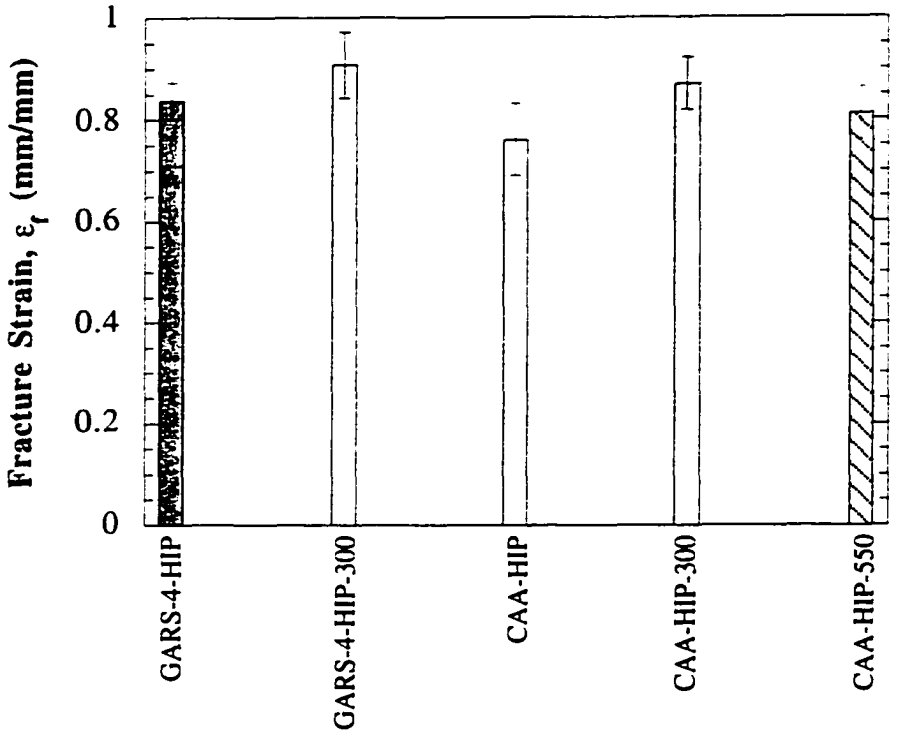

Figure 4.68. The effect of heat treatment on the fracture energy properties of the GARS-4 and CAA aluminum powders consolidated by the CIP-VCD-HIP route.

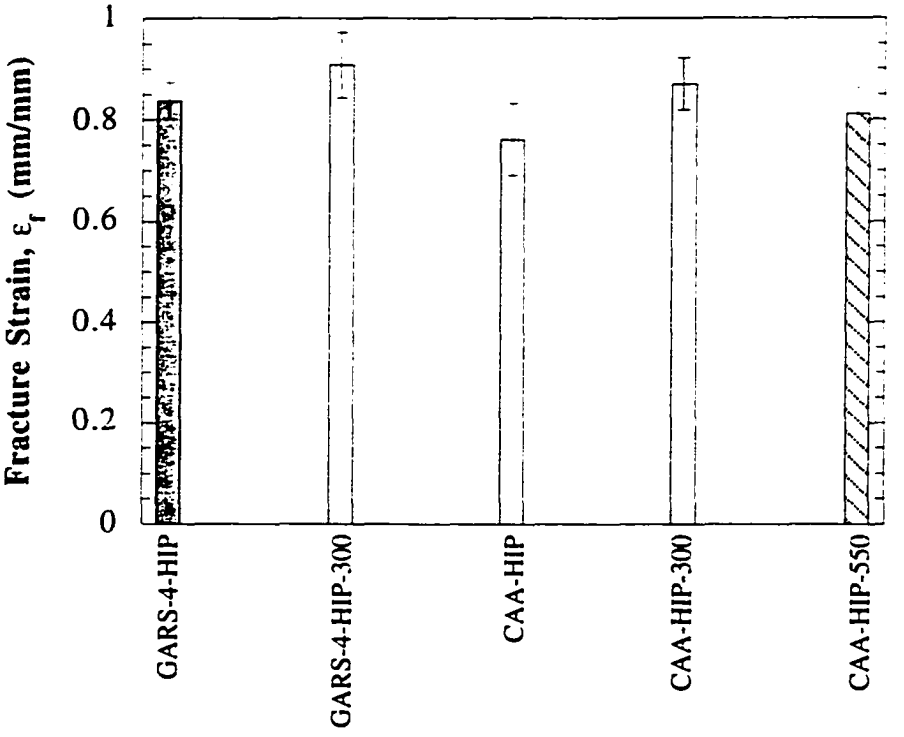

Figure 4.69. The effect of heat treatment on the fracture strain properties of the GARS-4 and CAA aluminum powders consolidated by the CIP-VCD-HIP route.

energy is related to the yield properties of the consolidated aluminum powder sample tested.

Sections of the heat treated GARS-4 and CAA CIP-VCD-HIP consolidated samples were punch tested. The punch test results, for the various states of heat treatment, are in Figures 4.67, 4.68, and 4.69. For a given powder type, the measured mechanical properties show no statistical difference between the non-heat treated and each of the heat treated conditions.

CHAPTER 5. DISCUSSION

The fabrication of aluminum P/M parts for aerospace applications by conventional aluminum powder processing [1] is expensive, perhaps ten to 1000 times the cost, compared to the press and sinter operations used for ferrous base P/M automotive components. The substitution of aluminum based P/M components for ferrous base P/M parts, for instance, in automotive drive train components, necessitates reducing the costs of processing aluminum powder. Lower manufacturing costs, though, need to be balanced against the requirement for good to superior mechanical properties of the aluminum P/M components necessary for automotive drive train applications.

Cost reduction of aluminum P/M components begins with an aluminum powder production method, such as inert gas atomization, that produces an aluminum powder that is safe to handle and has excellent consolidation properties. The costs for inert gas atomized aluminum powders are higher than for air atomized aluminum powders. However, the better characteristics of the inert gas atomized aluminum powder, compared to air atomized aluminum powder have the potential to reduce the high consolidation processing costs resulting from less advantageous powder characteristics of the air atomized aluminum powder. Consequently, for aluminum P/M components, the use of inert gas atomized aluminum powder may result in manufacturing costs that are equal to or less than the current manufacturing costs associated with air atomized aluminum powders.

Gas Atomization

During any gas atomization of aluminum powder, the aluminum droplets oxide in-flight as they solidify and pass through the spray chamber. The surface oxidation continues in the powder collection bins and during post-atomization handling. Commercial aluminum powder producers purposely oxidize the aluminum powders during gas atomization to

passivate the nascent aluminum powder surfaces to inhibit a powder explosion during post-atomization handling of aluminum powders.

The partial pressure of oxygen, or other gaseous oxidizing agent, in the atomization gas and in the spray chamber may influence the final shape of the aluminum powder particles. As the oxygen partial pressure increases, the aluminum powder particles become less spherical and more irregular, as noted by Özbilen et al. [13]. In the case of CAA, the pure aluminum powders shown in Figure 4.3 have a ligmental or irregular shape, due to the large volume percent of oxygen in the air atmosphere, about twenty-one volume percent causing immediate formation of an oxide film on the molten droplets' surfaces and preventing droplet spheroidization. In the case of the GARS aluminum powders, the atomization system and operation have been designed to minimize the oxygen content in the atomization gas and spray chamber. The resulting GARS pure aluminum powders (Figure 4.1) have a spherical shape. The CIGA-ATA pure aluminum powders have an irregular shape due to the presence of oxidizing agents in the atomization gas, i.e., carbon dioxide, a combustion product from the reaction of methane in air. An Ellingham diagram for oxides [65] shows carbon dioxide will readily oxide aluminum.

The times for oxidation, spheroidization, and solidification of aluminum droplets can be quantitatively compared and correlated to the qualitative observations made about the GARS and CAA pure aluminum powders. The interactive, quantitative model can also be used as a predictive tool to determine how much oxygen is permissible during gas atomization of aluminum powders to maintain spherical and near spherical powder geometries. In general, the results are plotted showing the atomization time scale dependency as a function of powder particle diameter.

The oxidation time for a metal droplet during gas atomization (equation 2.2a) has been shown by Nylund and Olefjord [11] to be inversely proportional to the partial pressure of oxygen in the atomization gas for an assumed oxide film thickness on the molten metal

droplet. The time for droplet spheroidization, equation 2.3, has been determined by Nichiporenko and Naida [12] to be inversely proportional to the liquid surface tension of the molten metal and directly dependent on the liquid metal viscosity.

The time for solidification of a gas atomized metal droplet is shown in equation 5.1 [12, 88]. The equation describes the time, t_{sol} (seconds) required for a liquid metal droplet of diameter, d_m (m) to cool to the melting point of the metal or solidus of the alloy, and lose its latent hear of fusion. Because equation 5.1 assumes no undercooling, the calculated time for solidification of a given droplet diameter is the shortest time for the droplet to solidify. The

$$t_{sol} = \frac{d_m * \rho_m}{6h_c}\left[\left(C_p\right)_m \ln\left(\frac{T_i - T_g}{T_m - T_g}\right) + \left(\frac{\Delta H_m}{T_m - T_g}\right)\right] \tag{5.1}$$

other terms are the convective heat transfer coefficient of the gas, h_c, the metal density, ρ_m (kg/m^3), the heat capacity of the liquid metal, $C_{p,\,m}$ (J/kg·K), the initial particle temperature, T_i (K), the gas temperature, T_g (K), the melting temperature of the metal, T_m (K), and the latent heat of fusion of the metal, ΔH_m (J/kg).

The research results of Özbilen et al. [13], shown in Figures 5.1 through 5.4, are used to assess the applicability of the atomization time scale equations to aluminum powder production. The aluminum powders were produced by a gas atomization method using gas mixtures of oxygen in nitrogen gas, ranging from zero to twenty-one volume percent oxygen. The atomization system was purged with a gas having the same oxygen content as the atomization gas. The pouring temperature of the commercial pure aluminum was 875°C.

The atomization time scales are first compared with the limiting gas atomization conditions used by Özbilen et al., twenty-one volume percent oxygen and zero volume percent oxygen in the nitrogen atomization gas in Figure 5.1 and Figure 5.2, respectively. The material parameters used for each comparison are listed in Table 5.1 and Table 5.2, respectively. Table 5.2 lists only changes of the initial droplet temperature and oxygen

Figure 5.1. SEM micrograph of aluminum powder produced by gas atomization with a mixture of 21.0 volume percent oxygen in nitrogen gas [13].

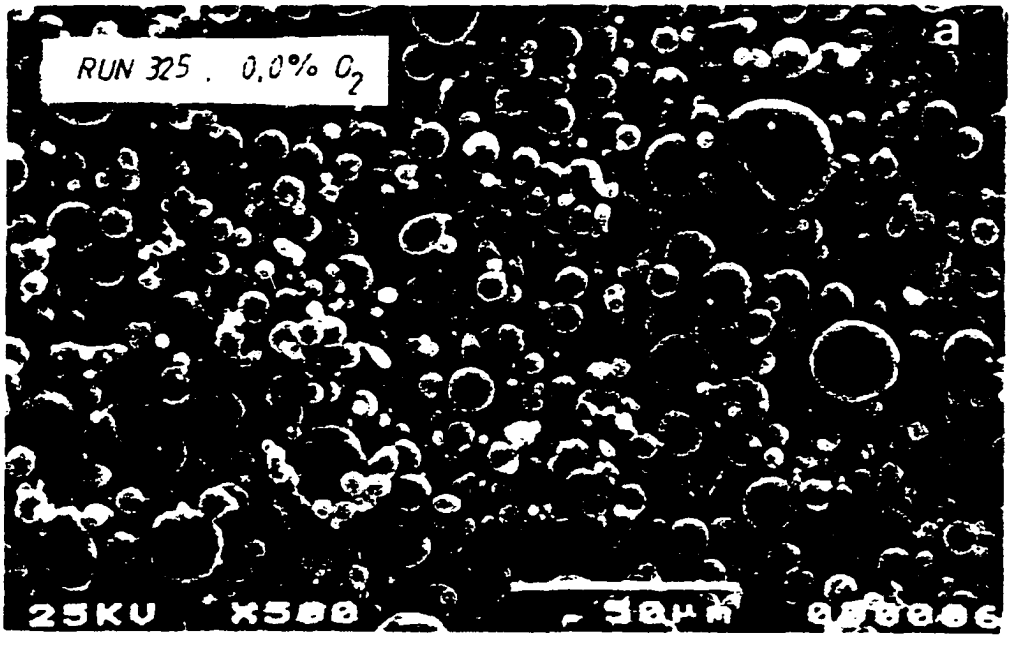

Figure 5.2. SEM micrograph of aluminum powder produced by gas atomization with a mixture of 0.0 volume percent oxygen in nitrogen gas [13].

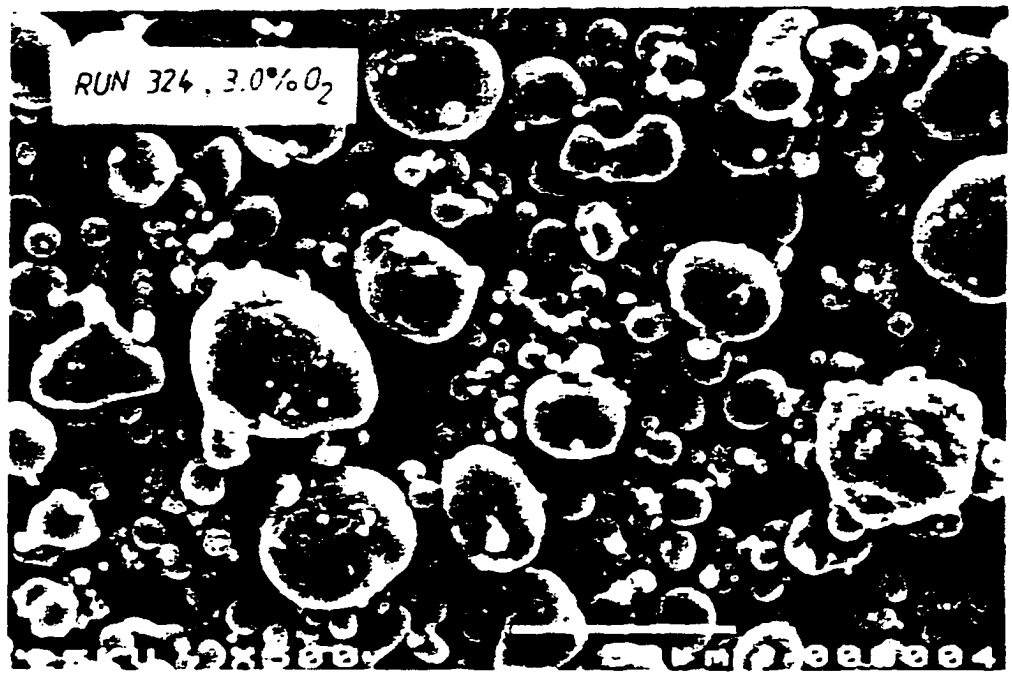

Figure 5.3. SEM micrograph of aluminum powder produced by gas atomization with a mixture of 3.0 volume percent oxygen in nitrogen gas [13].

Figure 5.4. SEM micrograph of aluminum powder produced by gas atomization with a mixture of 5.6 volume percent oxygen in nitrogen gas [13].

partial pressure of the atomization gas. Figure 5.5 and Figure 5.6 demonstrate the oxidation time necessary to form a 5 Å, 10 Å, and 15 Å thick oxide films on liquid aluminum droplets. The purpose for three different oxidation time scales is to illustrate the oxide film thickness sensitivity on the oxidation time. Another reason for three different oxidation time scales is to correlate any intersection of the oxidation time and the spheroidization time, at a specific droplet diameter, with the observed powder morphology. In other words, if an intersection of the atomization time scale lines occurs, the lowest portion of any time scale line is assumed to be the fastest occurring reaction.

For the case of atomizing with an oxygen partial pressure of 2.12×10^{4} Pa (21 volume percent oxygen) in nitrogen gas, or the equivalent gas composition of air (Figure 5.5) the calculated oxidation time for growing a 5 Å thick oxide film is less than the spheroidization time for all droplet diameters. The implication of this result is that no spherical powder particles will be produced during this gas atomization process. As the assumed oxide thickness increases to 10 Å and 15 Å, the oxidation time lines intersect the spheroidization time line at about 3.5 μm and 9.0 μm, respectively. The interpretation of these results is that spherical powders smaller the 3.5 μm and 9.0 μm, respectively, will be produced during this gas atomization process. Reviewing Figure 5.1 and noting the qualitative comments of Özbilen et al., there are no spherical powder particles produced during gas atomization of aluminum using the atomizing gas equivalent of air, cf. Figure 4.3. Therefore, one would assume that a 5 Å thick oxide film, or nearly one monolayer of oxide, on a molten aluminum droplet is sufficient to inhibit droplet spheroidization.

The other extreme is using a nitrogen atomization gas with a partial pressure of oxygen less than 4.04×10^{-1} Pa, essentially zero volume percent oxygen. In this case, the oxidation times for growing 5 Å, 10 Å, and 15 Å thick oxide films, for all droplet diameters, are about five orders of magnitude longer than the spheroidization time, indicating that all the powder particles should be spherical. A look at Figure 5.2 does show all the powder particles

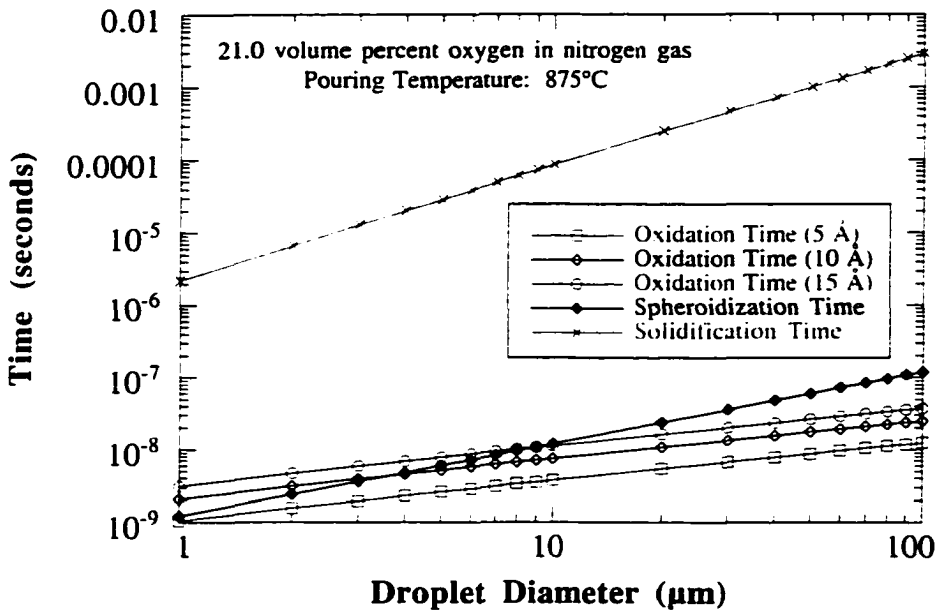

Figure 5.5. Atomization time scale comparison for molten aluminum gas atomized with a gas mixture of 21.0 volume percent oxygen in nitrogen gas.

Table 5.1. Material parameters used in equations 2.2a, 2.3, and 5.1 for the comparison of atomization time scales in Figure 5.5.

Parameters	Variables	Values	Units	References
Initial Temperature	T_i	1.148×10^3	K	
Oxide Thickness	t_{ox}	5.0×10^{-10}	m	
Oxygen Partial Pressure	$p(O_2)$	2.120×10^4	Pa	
Molar Mass of Oxygen	M(O)	1.6×10^{-2}	kg/mol	
Diffusivity of Oxygen in Nitrogen	$D(O_2)_{N_2}$	1.78×10^{-4}	m^2/s	[89]
Density of Oxide	ρ_{ox}	3.4×10^3	kg/m^3	
Oxygen Weight Fraction in Oxide	$X_{O,ox}$	4.7×10^{-1}		
Gas Constant	R	8.314×10^1	J/mol·K	
Nitrogen Gas Temperature	T_g	2.07×10^2	K	[90]
Density of Liquid Aluminum	$\rho_{Al(l)}$	2.34×10^3	kg/m^3	[91]
Relative Gas Velocity	v_g	1×10^3	m/s	[90]
Viscosity of Liquid Al	$\mu_{Al(l)}$	1.446×10^{-3}	Pa·s	[92]
Heat capacity of Nitrogen Gas	$C_{p,g}$	1.039×10^3	J/kg·K	[93]
Viscosity of Nitrogen Gas	μ_g	1.47×10^{-5}	Pa·s	[94]
Thermal Conductivity of Nitrogen Gas	λ_g	1.9×10^{-2}	W/m·K	[94]
Surface Tension of Liquid Al	$\sigma_{Al(l)}$	8.5×10^{-1}	N/m	[95]
Heat capacity of Liquid Al	$C_{p,Al(l)}$	1.177×10^3	J/kg·K	[93]
Density of Nitrogen Gas	ρ_g	1.46×10^1	kg/m^3	[94]

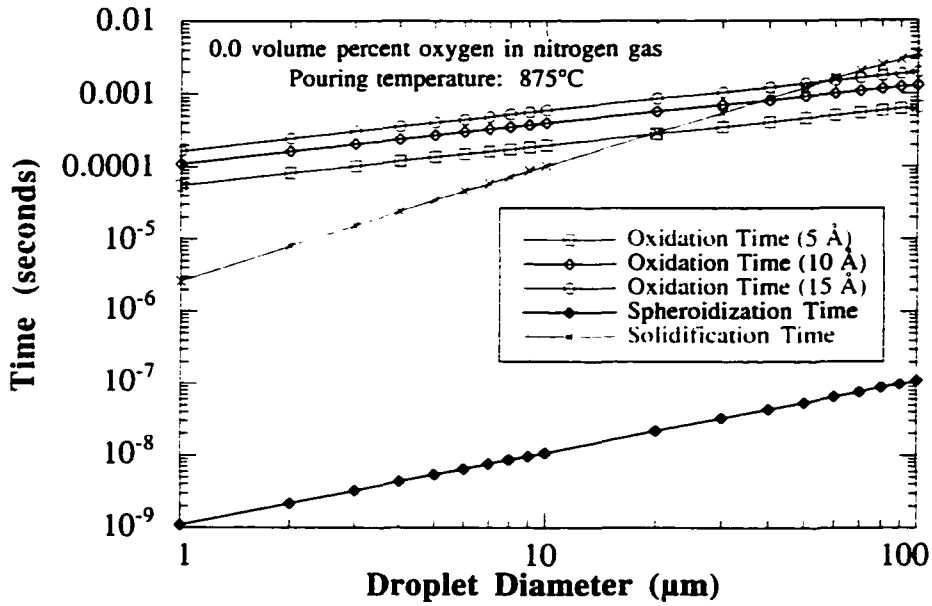

Figure 5.6. Atomization time scale comparison for molten aluminum gas atomized with a gas mixture of 0.0 volume percent oxygen in nitrogen gas.

Table 5.2. Material parameter changes of Figure 5.5 for the comparison of atomization time scales in Figure 5.6.

Parameters	Variables	Values	Units
Initial Temperature	T_i	1.223×10^3	K
Oxygen Partial Pressure	$p(O_2)$	4.04×10^{-1}	Pa

to be spherical. Similar powder morphologies occur during the GARS method of atomizing liquid aluminum (Figure 4.1). Some powder particles are deformed or have satellite powders due to dynamic droplet-droplet collisions during gas atomization.

With respect to the minimum solidification time indicated in Figure 5.5, the droplet spheroidization time of liquid aluminum droplets is three to four orders of magnitude faster. A prediction is also made that droplets smaller than 20 μm will solidify before they form a 5 Å thick oxide film. For the same assumed oxide thickness, spherical droplets larger than 20 μm are predicted to oxidize before solidification. Because the indicated solidification time is a minimum time scale, i.e., no droplet undercooling, there is uncertainty as to whether the spherical droplets solidify before oxidation or vice versa.

A comparison of the atomization time scales also appears to be valid for aluminum powder produced by gas atomization processes with intermediate oxygen levels in the atomization gas. With reference to the results of Özbilen et al. [13], they have shown intermediate partial pressures of oxygen in the atomization gas, 3.03×10^3 Pa (3 volume percent oxygen) and 5.66×10^3 Pa (5.6 volume percent oxygen) produce a mix of different shaped aluminum powder particles as shown in Figure 5.3 and Figure 5.4, respectively. For a given powder size, their experimental results show that as the oxygen partial pressure in the atomization gas increases above 3.03×10^3 Pa, the shape of the aluminum powder particles changes from globular to elongated to irregular. The transition from spherical powders to irregular powders, for a given powder size, would indicate that the oxidation time is becoming increasingly faster than the spheroidization with increasing oxygen content of the atomization gas.

The intersection of the oxidation and spheroidization time line for oxygen partial pressures of 3.03×10^3 Pa in the nitrogen atomization gas (Figure 5.7) indicates a transition from spherical to non-spherical droplets at diameters of about 60 μm for a 5 Å thick oxide film and greater than 100 μm for 10 Å and 15 Å thick oxide films. Figure 5.3 shows the aluminum particles gas atomized under the same conditions to be mostly spherical for all powder sizes. The larger powder particles, greater than about 35 μm, tend to be more globular than spherical. As the oxygen partial pressure in the atomization gas increases to 5.66×10^3 Pa, Figure 5.8 shows the transition from spherical to non-spherical powders to be about 16 μm for 5 Å thick oxide films, 70 μm for 10 Å thick oxide films, and greater than 100 μm for 15 Å thick oxide films. Figure 5.4 shows the aluminum powder particles are nearly all irregular shaped, except for a portion of particles smaller than about 10 μm, which are about spherical in shape. In both these cases, the intersection of the oxidation time line and spheroidization time line shows reasonable agreement for an assumed oxide film thickness of 5 Å on aluminum droplets, more so than with assumed oxide film thicknesses of

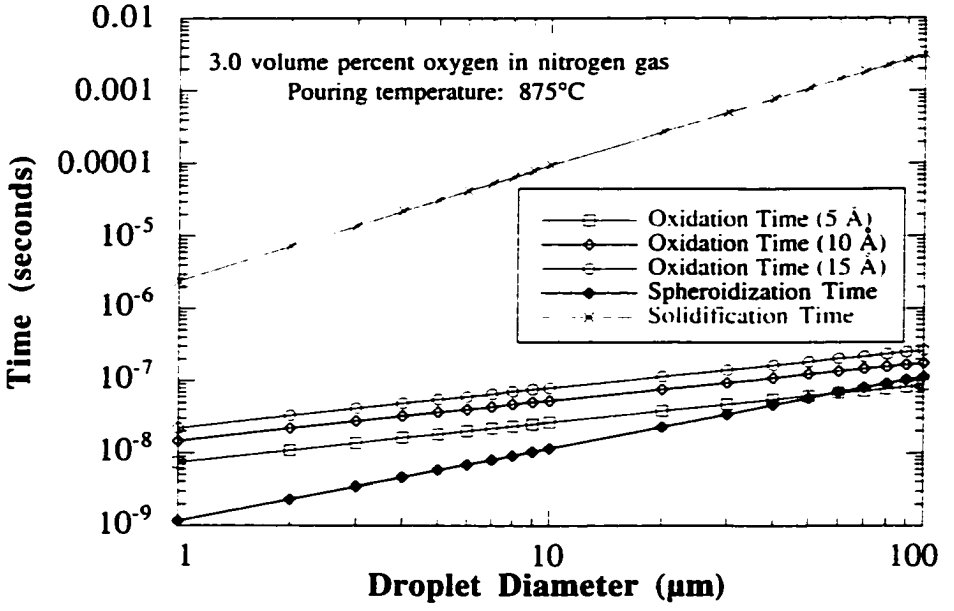

Figure 5.7. Comparison of atomization time scales for aluminum powder nitrogen gas atomized with 3.0 volume percent oxygen in the atomization gas.

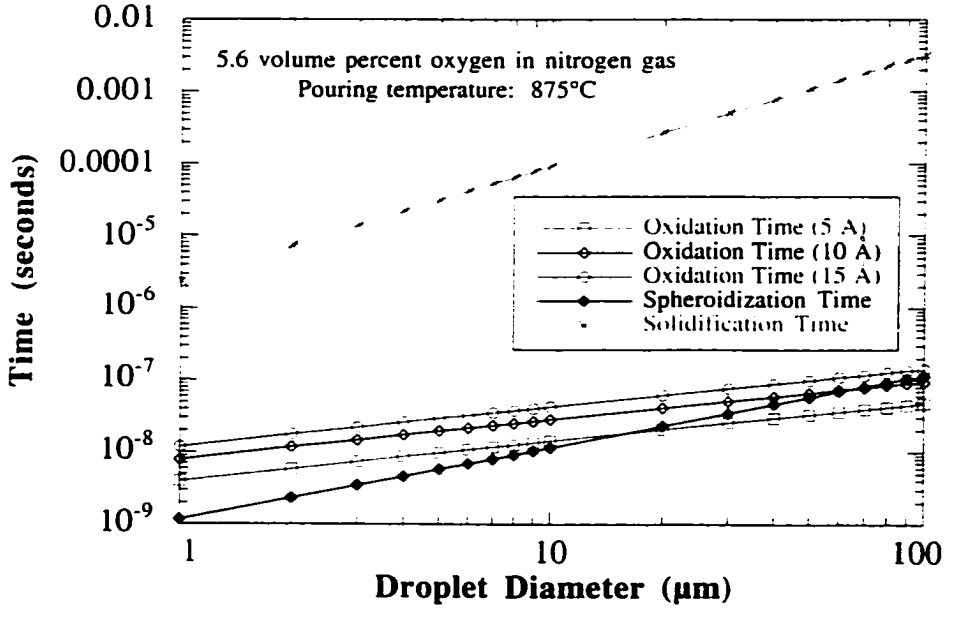

Figure 5.8. Comparison of atomization time scales for aluminum powder nitrogen gas atomized with 5.6 volume percent oxygen in the atomization gas.

10 Å and 15 Å.

If the atomization time scales accurately predict some of the kinetics of aluminum gas atomization, the design of a gas atomization process is possible. Consider two atomization gases, 2.0 volume percent oxygen in helium gas and 3.0 volume percent oxygen in nitrogen gas, and apply the atomization time scale equations to both conditions (Figure 5.9 and Figure 5.10). A comparison of the results shows the spheroidization time of aluminum droplets to be faster in the nitrogen-based atomization gas than in the helium-based atomization gas by about 0.5 nanoseconds. However, the oxidation times for the same assumed oxide film thickness are faster in the helium-based gas by about one to two nanoseconds, because of the higher diffusivity of oxygen in the helium-base gas than in the nitrogen-based gas. The intersection of the spheroidization time line and oxidation time line for a 5 Å thick oxide film for helium-based gas atomization conditions is near a droplet diameter of 60 μm. For nitrogen-based gas atomization, the intersection of the oxidation time line and solidification time line occurs at droplet diameters greater than 100 μm. The significance of these result,

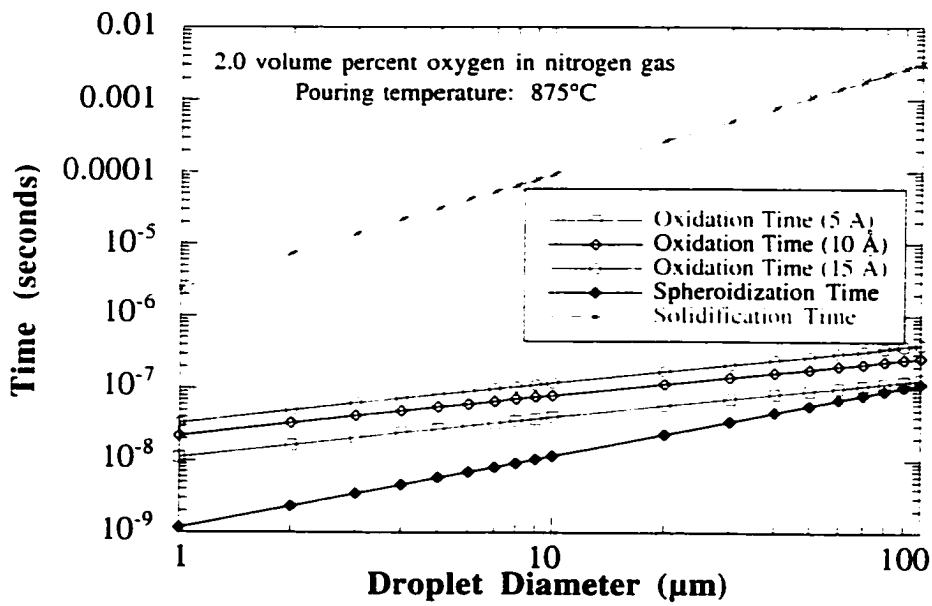

Figure 5.9. Comparison of atomization time scales for aluminum powder nitrogen gas atomized with 2.0 volume percent oxygen in the atomization gas.

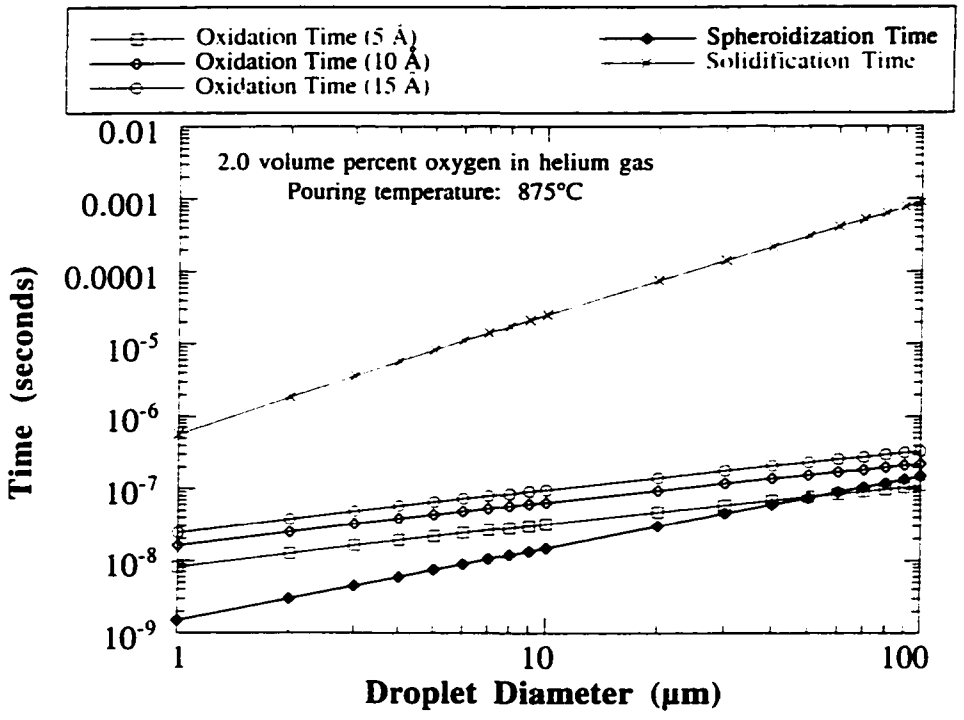

Figure 5.10. Comparison of atomization time scales for aluminum powder helium gas atomized with 2.0 volume percent oxygen in the atomization gas.

assuming a 5 Å thick oxide film on the molten droplets, is that the nitrogen-based gasatomization process may be operated at lower cost than the helium gas atomization process, while producing a wider size distribution of spherical aluminum powder particles.

Powder Characterization

Bulk oxygen measurements

Bulk oxygen measurements techniques, such as the IGF method, do not provide any information about the location of oxygen in the aluminum powder particle or the chemical compound(s) from which the oxygen originated. Complementary analyses are necessary to establish the location and chemical origin of the oxygen as measured by IGF. One such analysis is AES depth profiling analysis of the GARS (Figure 4.19), CIGA, and CAA (Figure 4.19) aluminum powders, which shows oxygen to be a part of a finite alumina layer on the powder particle surfaces. The presence of the alumina oxide film is further confirmed with

EDS conducted during the TEM analysis of the CAA and GARS-8 aluminum powders (Figure 4.25 and Figure 4.27) respectively. The presence of physiosorbed and chemisorbed water associated with the surface oxide film is established with the QMS experiments of the as-atomized aluminum powders (Figure 4.11, Figure 4.12, Figure 4.13, and Figure 4.14). All these complementary analyses show the oxygen to be located in an oxide surface film on the aluminum powder particles surfaces, combined with aluminum and hydrogen to form alumina oxide, hydrated alumina oxide, and water.

The oxygen content of aluminum powder particles is directly proportional to the powder surface area, oxide film thickness, and the oxide water content. According to Wefers [96], a reasonable correlation between oxide mass and thickness exists only for uniform, parallel films grown on non-alloyed metal at low temperatures. The oxygen dependence on the surface area and oxide film thickness is demonstrated with a simple geometrical argument. Assume the as-atomized aluminum powder particles are spheres with diameter, d (m), have a uniform oxide thickness, t_{ox} (m), and the oxygen is only combined with aluminum in the form of alumina (Figure 5.11). The hypothesis is that the oxide film thickness on aluminum powder particles can be predicted for a distribution of aluminum powder sizes from a bulk oxygen measurement of the powder and the powder size distribution data. The results of the model are compared with the AES oxide film thickness

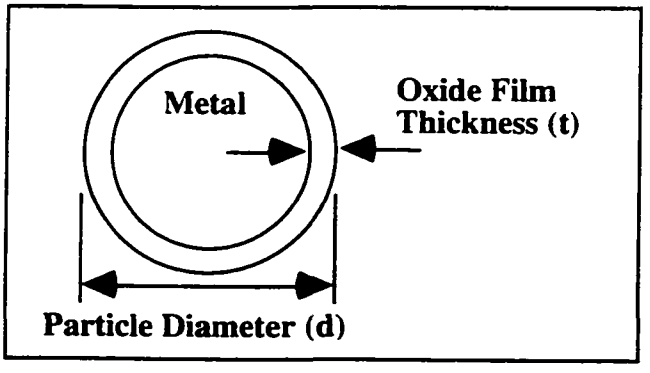

Figure 5.11. Schematic of powder particle used for predicting the oxide film thickness on aluminum powder particles.

measurements.

Before predicting the oxide thickness on a distribution of powder sizes, first consider a discrete powder particle as shown in Figure 5.11. The volume of the oxide shell, V_{Oxide} (m^3), on the aluminum powder particle surface is determined from equation 5.2 and is rewritten in terms of the particle diameter and assumed oxide thickness in equation 5.3. The calculated oxide volume of the shell is used in equation 5.4 to calculate the mass of oxygen, m_{Oxygen} (grams), in the film, where $\rho_{Al_2O_3}$ is the density of alumina (g/cm^3), MW_{Oxygen} is the molecular weight of oxygen (grams/mole), and $MW_{Al_2O_3}$ is the molecular weight of alumina (grams/mole). The calculated mass of oxygen in the oxide shell is divided by the mass of the powder particle to give the weight percent of oxygen on the surface of the aluminum powder particle.

A plot of the weight percent of oxygen as a function of particle diameter and oxide film thickness is shown in Figure 5.12. For a given oxide film thickness, the oxygen content of discrete aluminum powder sizes increases with decreasing powder diameters or increasing

$$V_{Oxide} = V_{Particle} - V_{Metal} \tag{5.2}$$

$$V_{Oxide} = \frac{\pi}{6}\left[d^3 - (d - 2t_{ox})^3\right] \tag{5.3}$$

$$m_{Oxygen} = V_{Oxide}\frac{3\rho_{Al_2O_3} MW_{Oxygen}}{MW_{Al_2O_3}} \tag{5.4}$$

surface area. Similarly, for a particular aluminum particle diameter or powder surface area, the oxygen content increases as the oxide film thickness on the aluminum powder particle increases.

To apply this model to a distribution of powder sizes, some modifications are necessary. Using the particle size distribution results and an assumed oxide film thickness, the oxygen content, in weight percent ($wt\%_{Oxygen}$), is determined for each particle size

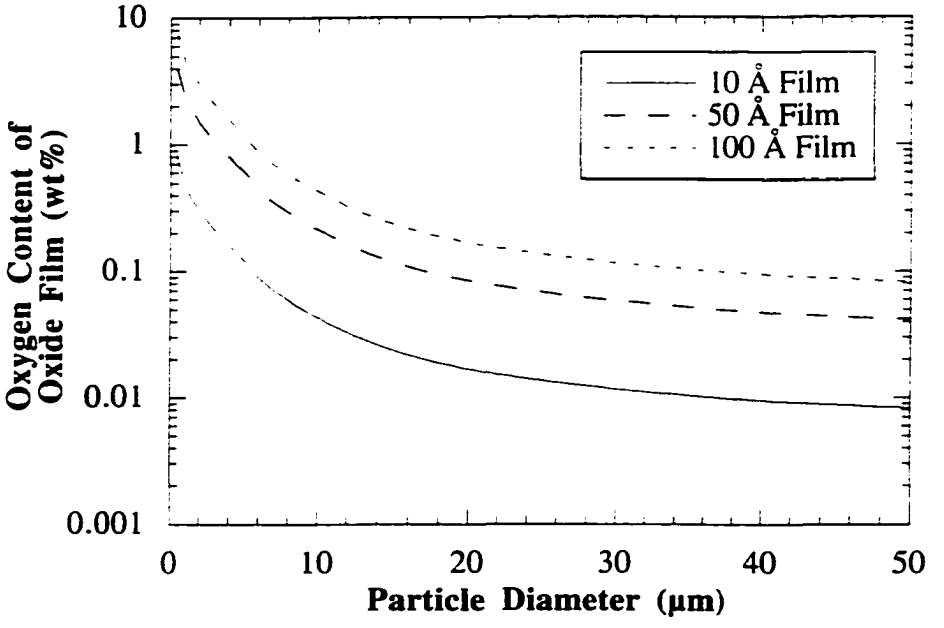

Figure 5.12. Plot of oxygen content of the oxide film on aluminum powder particle as a function of particle diameter and oxide film thickness.

channel (n) of the size distribution. The oxygen content of each particle size channel is multiplied by the volume fraction of particles in that particle size channel ($V_{n,\,fraction}$). The sum of all these products, equation 5.5, is a calculated bulk oxygen content for the aluminum powder size distribution. The sequence of these calculations required several iterations with different assumed oxide film thickness to match the calculated bulk oxygen content with the measured bulk oxygen content. Figure 5.13 shows a comparison of the AES oxide film

$$wt\%_{Oxygen} = \sum_{n=1}^{n=i} V_{i.fraction} * \left(\frac{m_{i.Oxygen}}{m_{i.Particle}} \right) \tag{5.5}$$

thickness measurements and the oxide film thickness used in the calculations for the GARS, CIGA and CAA aluminum powders. The model shows reasonably good agreement with the AES oxide film thickness measurements for the GARS and CIGA aluminum powders due to the spherical nature of the powder particles.

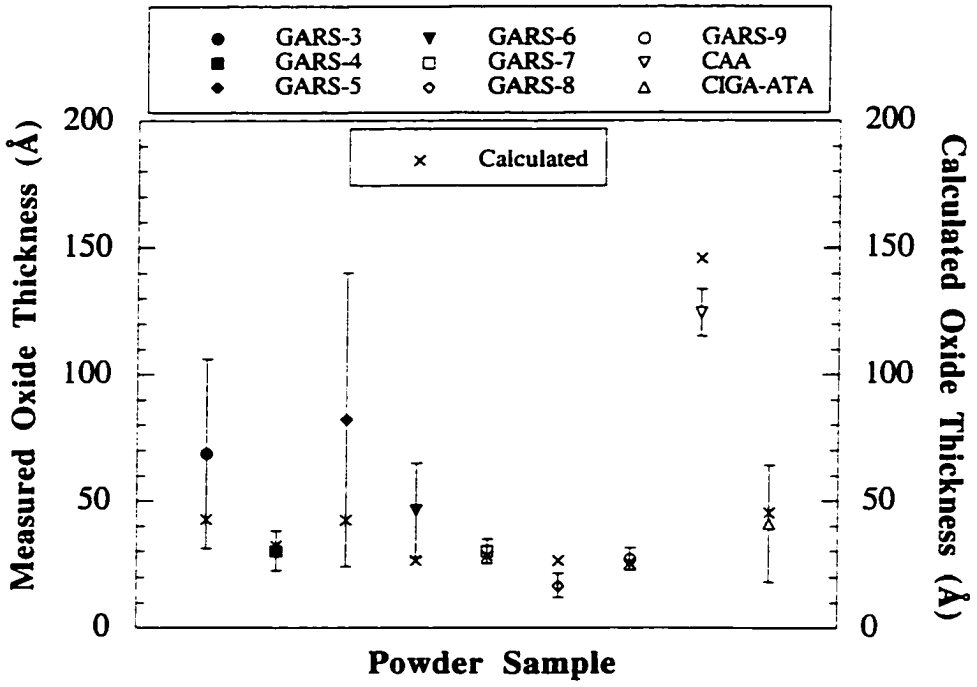

Figure 5.13. Comparison of oxide film thicknesses predicted from the model presented in the text and as measured by AES.

The overestimation of the oxide thickness for the CAA aluminum powder may be due to a combination of variables, such as the irregular particle shape of the CAA aluminum powder and the elevated water content of the CAA aluminum powder as measured by QMS. The model does not accommodate irregular shape particles. The backbone of the model rests solely on the particle size distribution. The irregular particle shape creates an erroneous particle size distribution, because the data was obtained under the assumption that the powder particles are spherical. The model, though, would appear to calculate an upper limit for the oxide film thickness on the CAA aluminum powders, given the current data.

The other variable is the elevated water content of the CAA powder particles. Recall, the iterative model assumes a specific oxide film thickness composed of only an anhydrous aluminum oxide and the calculated oxygen content is directly proportional to the assumed oxide film thickness. QMS results of the CAA aluminum powder indicates a hydrated oxide film. A bulk oxygen measurement would account for both the aluminum oxide and water in

the oxide film. If the water content of the oxide was not included in the bulk oxygen measurement, the result would be a lower measured oxygen content. The lower measured oxygen content could be matched with a calculated oxygen content using a smaller assumed oxide film thickness, which would show better agreement with the CAA aluminum powder AES measurement of the oxide film thickness.

GARS Aluminum powder oxidation

Pure aluminum powder

The oxidation of aluminum powders begins within the first milliseconds of the gas atomization process, see atomization time scale figures above. Oxidation continues in the atomization system during the flight of the liquid aluminum droplets, during solidification of the droplets, and during collection of the solid powder particles. The in-flight oxidation reaction products are aluminum oxide and varying concentrations of hydrated aluminum oxide incorporated into an amorphous oxide surface film (Figure 4.22 and Figure 4.23). The oxidation reaction reactants are the result of residual oxidizing agents in the atomization gas, in the spray chamber, and in the powder collection vessel of the atomization system. During post-atomization handling of the aluminum powder, oxidation will continue depending on the oxygen content and the relative humidity of the post-atomization handling atmosphere. In the case of the CAA process, for example, the CAA aluminum powder is removed from the atomization system and handled either under an inert gas [2] or in dry air [3].

An observation of the post-atomization oxidation was made by exposing GARS aluminum powder to air containing various levels of humidity, ranging from 0% relative humidity to 85% relative humidity, held at room temperature for up to 125 days (Figure 4.38 and Figure 4.40). The GARS-9 aluminum powder was exposed to ambient air at 300°C for up to 41.7 days (Figure 4.45). The oxidation of the GARS aluminum powders is due to oxygen and water in the air. The moisture content of the air appears to have a strong

influence on the oxidation behavior of aluminum powders. Note in Figure 4.38, as the relative humidity level in the ambient air increases, the initial rate of oxidation and hydration of the aluminum powders surfaces increases and tapers off towards a limiting value.

An hydration reaction is evident from the QMS results of the unexposed and exposed states of the GARS-9 aluminum powder (Figure 4.39). The exposed GARS-9 aluminum powder sample tested in the QMS system was subjected to the 15% to 25% relative humidity level, shown in Figure 4.38, for 125 days at room temperature. The unexposed GARS-9 aluminum powder was collected from atomization powder collection can in a glove box with an argon atmosphere. The hydration observed in Figure 4.39 is shown as an increase of the QMS hydrogen spectra signal in the range of 200°C to 500°C. The hydrogen spectra originates from the reaction of water in and on the oxide film with aluminum cations diffusing from the metal core, through the oxide film, to the surface of the powder particle. Hydration is also observed from the significant increase of measured bulk oxygen in Figure 4.40. The GARS-9 powder was exposed to an air environment at 29.4°C with 85% relative humidity for 41.7 days. Note the significant change in the ordinate scales of Figure 4.40 compared with Figure 4.38. The results of these air exposure experiments point to the fact that the water content of the atmospheric air is a significant source of the oxidation and hydration on aluminum powder surfaces.

In Figure 4.38, the first 12.5 days of air exposure shows rapid increase of the measured bulk oxygen content. After 12.5 days, the rate of oxidation and hydration slowly decreases towards a constant oxygen level. The measured oxidation and hydration translates to an increase of the oxide film thickness. Figure 4.42 shows the GARS-8 aluminum powder to increase its oxide thickness from about 20 Å in the unexposed state to nearly a constant level of 80 Å after 12.5 days of air exposure. The latter AES oxide film thickness is similar to the TEM oxide film thickness shown in Figure 4.24. In reference to Figure 4.38, the GARS-8 aluminum powder was exposed at room temperature in the 45% to 50% relative

humidity range.

A similar trend was observed with -38 μm, GARS-9, aluminum powders exposed to ambient air at 25°C and 300°C for the MEC testing. Figure 4.45 shows the measured bulk oxygen content as a function of time. The oxidation rate of the -38 μm aluminum powder at 300°C is much faster than the oxidation rate at 25°C. Table 4.11 shows the measured AES oxide film thickness for some exposure conditions of the -38 μm aluminum powder. After ten hours of exposure at 25°C, the AES oxide film thickness is about 50.5±11.1 Å compared with the unexposed, GARS-9, oxide film thickness of 26.9±4.4 Å (Table 4.7). Increasing the exposure time and temperature to 100 hours and 300°C, respectively, increases the oxide to 81.4±8.4 Å. At the same temperature, but after 1000 hours of exposure, the oxide film thickness increases to 225.4±21.0 Å.

The growth, or thickening, of aluminum oxide films residing on flat aluminum or aluminum alloy substrates has been described mathematically for oxidation at low temperatures. In dry oxygen, the oxide growth has been described by an inverse logarithmic type function of time at temperatures below 400°C, equation 5.6 [97]. K and K' are constants, t is the oxidation time, and δ is the oxide thickness. A constant t_0 is necessary, because the oxide forming during the oxidation experiments grows on top of a previously formed oxide film. t_0 is the time to thicken an oxide film of the same thickness as the original oxide film. In principle, the inverse logarithmic function represents the migration of

$$\frac{1}{\delta} = -K \log_{10}(t + t_0) + K' \tag{5.6}$$

aluminum cations through the oxide film initially due to strong electrical potentials across the oxide film. At room temperature, the electric field is created by electrons from the aluminum atoms that have "tunneled" through the oxide film and ionized the adsorbed oxygen molecules on the aluminum surface. Before the aluminum ions can migrate from the metal-oxide boundary to the oxide-gas boundary, the aluminum ions must overcome an activation

energy barrier at the metal-oxide boundary. The presence of the potential field reduces the energy required to surmount the energy barrier. As the oxide film grows thicker, the electrical potential decreases exponentially, increasing the energy required for an aluminum ion to pass the metal-oxide boundary, reducing the rate of oxidation of the substrate surface. The logarithmic formulation leads to a limiting oxide thickness of 20 Å to 30 Å.

Hart [97] states that the "practical limit" is superseded by the presence of moisture in the oxygen environment. The initial growth is dependent on a direct logarithmic function of time, equation 5.7, during the first ten hours of exposure, after which the growth

$$\delta = -K \log_{10}(t + t_0) + K' \tag{5.7}$$

is best matched by the inverse logarithmic function of time. The direct logarithmic growth law describes the migration of aluminum cations as being faster than the electron motion and is applicable until both the electron and aluminum cation motion are equal. Once the electron motion surpasses the aluminum cation diffusion, the inverse logarithmic function describes the thickening of the oxide film. The diffusion of the aluminum cations through the amorphous oxide film is likely due to the specific volume of the amorphous film. The larger the specific volume, the more open the structure of the amorphous film, leading to higher cation diffusivities [98].

The application of the inverse logarithmic oxide growth function has been extended to aluminum alloy powders, as present by Carney et al. [99], to describe the oxidation of aluminum alloy powders in the atomization system. For this research, a review of the results from the powder oxidation experiments shows the best type of curve fit to the bulk oxygen measurements in Figure 4.38 and Figure 4.40 is a logarithmic function of time. The oxidation is initially fast, but approaches a limiting value at exposure times greater than 12.5 days. The "practical limits" of the oxide film thickness on GARS-8 and CAA aluminum powder appears to be nearly 80Å (Figure 4.41) and 125Å (Figure 4.21), respectively. One

could say with reasonable assurance that the oxidation occurring on the surfaces of the GARS pure aluminum powders is probably controlled primarily by cation migration through the oxide film.

GARS Al-Ti-Y aluminum alloy powder

The addition of alloy elements to produce a prealloyed aluminum powder can lead to different oxidation behavior than observed with the oxidation of pure aluminum powders, particularly at elevated temperatures. The oxidation rate of the GARS Al-Ti-Y powder exposed at 25°C and 162°C (Figure 4.41) is similar to the oxidation rate of the GARS-7 and GARS-8 pure aluminum powders exposed at 25°C in an air atmosphere of 45% to 50% relative humidity (Figure 4.38). Increasing the oxidation temperature to 300°C, increases the oxidation rate of the Al-Ti-Y alloy powder within the first 142 hours or 5.9 days. After this time, the oxidation rate increases further as indicated by the "knee" in the oxidation curve. The rate change is referred to as a "break away" oxidation mechanism, attesting to some change in the transport mechanism of either aluminum cations or oxygen anions through the oxide film.

The oxidation behavior of the Al-Ti-Y alloy may be explained in terms of how "active" alloy elements, such as yttrium and titanium, can influence the oxidation behavior of alumina forming scales. The information about these and other active elements is from literature discussing alumina scales on high temperature alloys containing aluminum. The same information will be assumed to apply to low temperature oxidation of the Al-Ti-Y alloy powder, especially to explain the observed "knee" in the oxidation curve at 300°C.

The role of titanium has been shown to have adverse effects as well as no effect on the oxidation behavior of high temperature alloys [100]. The influence of titanium appears to be dependent on its concentration in the alloy. For example, Huntz states that 0.2% titanium by weight in an FeNiCrAl alloy does not alter the oxidation kinetics. However, increasing

the titanium content to 0.54% by weight increases the oxidation weight gain rate at 1200°C. The combination of titanium with yttrium in the same FeNiCrAl alloy shows no effect on the alloy oxidation behavior. Huntz continues to state that there is general agreement that rare earth elemental additions, such as yttrium, have beneficial effects on the high temperature oxidation resistance of alumina-forming alloys. The observed benefits depends on the concentration and the presence of other active elements. Jedlinski [101] states that yttrium additions improve the adherence of the oxide scale to the substrate.

The literature shows much debate over the effect of yttrium on the transport properties of alumina on alumina forming alloys. Yttrium has been shown to increase aluminum cation diffusion and decrease oxygen anion diffusion as well as decrease aluminum cation diffusion and increase oxygen anion diffusion [100]. One summary statement of this controversy is that yttrium alters the transport processes in the alumina surface oxide. Prescott and Graham [102] comment in their review of active elements that yttrium additions suppress aluminum cation diffusion outward and promote oxygen anion diffusion inward.

One way yttrium can affect the oxidation behavior is by the formation of a yttrium-aluminum-oxide phase, such as $Y_3Al_5O_{12}$ or Y_2O_3. These two phases appeared in the XRD pattern of the Al-Ti-Y alloy (Figure 4.30). Because the oxygen resides on the surface of the powder particles, the yttrium-aluminum-oxide phases most likely reside on the surfaces of the powder particle, and are of a sufficient volume fraction to be detected with XRD. Huntz cites Choquet [103] as showing that the oxygen diffusion through the $Y_3Al_5O_{12}$ and Y_2O_3 phases is greater than alumina at 1100°C. In the same XRD pattern (Figure 4.30) the presence of titanium phases, other than a slight indication of the Al_3Ti phase, is below the detectability limit of XRD. The heating curve of the DTA trace of the Al-Ti-Y powder also indicates no prevalent titanium phases. As a result, titanium is assumed to be benign during the oxidation of the Al-Ti-Y alloy powder at 300°C, a role deemed plausible given the

information about the effect of titanium combined with yttrium during the oxidation of alumina on alumina forming alloys.

To described the oxidation behavior observed in Figure 4.41, oxygen anion diffusion is assumed to be the predominate transport species through the oxide film. The justification of this assumption comes from the presence of the $Y_3Al_5O_{12}$ and Y_2O_3 phases and the experimental evidence of others, as cited by Prescott and Graham [102], which shows a relative reduction in the aluminum cation diffusion through the oxide. Evans [104] and Schütze [105] comment that anion diffusion inward through the oxide film will create new oxide at the oxide-metal boundary. Evans [104] pictorially describes the failure mechanism of oxide layers on convex surfaces by anion diffusion. One failure mechanism is decohesion and subsequent delamination of the oxide layer. This failure mechanism does not seem plausible with the experimental evidence available, cited by Prescott and Graham [102], that yttrium additions improve the adherence of oxide films to the substrate. The other failure mechanism is tensile cracking of the oxide film due to the oxide formed at the oxide-metal boundary pushing the original oxide to larger circumferences. This latter failure mechanism would create fissures or microcracks in the oxide film, creating a short circuit diffusion path for oxygen anions, as well as aluminum cations. An increase in the exposure temperature would most likely raise the diffusivity of the oxygen through the oxide film resulting in a measurable increase of the bulk oxygen content of the Al-Ti-Y aluminum alloy powder, as seen in Figure 4.41.

In light of the previous discussion, an interpretation of the 300°C oxidation experiment is given. From the unexposed state to about 142 hours of exposure, oxygen anions diffuse through the oxide film due to the presence of the yttrium additions. During this exposure time, the new oxide growing at the oxide-metal boundary is pushing the old oxide film to the point of forming tensile cracks which lead to fissures and/or microcracks in the oxide film. As the exposure time increases above 142 hours, the tensile cracks have

created short circuit diffusion paths for both the aluminum cations and oxygen anions. During this time frame the oxide is healing and cracking itself, creating more oxide, which corresponds with the increasing bulk oxide content of the Al-Ti-Y powder as a function of time.

Aluminum powder explosibility

The degree of explosibility of aluminum powder has been documented in the literature only as a function of surface area, similar to the data shown in Figure 4.44. The MEC data in this figure shows fine particle sizes, or larger surface areas, of pure aluminum powder are more explosive than the coarse particle sizes, or smaller surface areas. In general, the MEC data in Figure 4.43 indicates the GARS aluminum powders are rated in the "strong" category for the probability of a dust cloud type of explosion hazard. The same figure shows the CIGA-AT, CIGA-VAL, and CAA pure aluminum powders to be rated in the "severe" category for the probability of a dust cloud type of explosion hazard. The CIGA-AT and CAA have larger surface areas compared to the GARS aluminum powders, which would indicated surface area is a strong variable for explosibility.

The MEC value of the CIGA-VAL aluminum powder is 0.030 ounces per cubic foot, placing the CIGA-VAL aluminum powder in the "severe" category for the probability of a dust cloud type of explosion hazard. However, the particle size distribution, or specific surface area, of the CIGA-VAL (Table 4.1 and Table 4.2) is similar to the -38 μm GARS-9 aluminum powder (Table 4.10 and Table 4.11) yet the GARS-9 aluminum powder has better explosibility properties as measured by a MEC test. One may infer from these results that surface area may be only one variable contributing to the MEC of pure aluminum powders. Other explosibility variables related to the powders to consider are the oxide film thickness on the aluminum powder surfaces and the gas atomization method used to produce the aluminum powders. The latter variable determines the oxidizing atmosphere in which the

oxide film was initially formed on the nascent aluminum droplet.

The CIGA-VAL aluminum powder has an oxide film thickness of 159±29 Å, which is mid-range between the thermally grown oxide films on the -38/100/300 and -38/1000/300 GARS-9 aluminum powders, 81.4±8.4 Å and 225.4±21.0 Å, respectively. One would expect, if the oxide film thickness contributed to the MEC of the aluminum powders, then the MEC value of the CIGA-VAL aluminum powder should be between the -38/100/300 and -38/1000/300 GARS-9 aluminum powder samples. As was mentioned above, the CIGA-VAL powder has a lower MEC value than the -38 μm GARS-9 powders, i.e., the former has more of an explosive tendency than the latter. From these MEC results, oxide thickness may still be a variable, but the MEC test may not be sensitive to these levels of oxide film thickness.

The other dependent variable of explosibility to consider is the atomization method used to produce the aluminum powders and the post-atomization oxidation conditions. The CIGA-VAL process purges the atomization system with a process gas and uses an atomization gas mixture of helium gas and a maximum of two volume percent oxygen gas. Recall, the gas purging may not remove residual oxidizing agents, such as oxygen and water, from the atomization system. The initial oxide to form on the CIGA-VAL aluminum droplet surface must form in a relatively high temperature oxidation process. The oxide forms near the temperature of the melt as is exits the pour tube, before solidification of the molten droplets (Figure 5.10) due to the close proximity of oxygen to the freshly, atomized aluminum droplets. Similar oxidation behavior is shown to occur with a CAA process (Figure 5.5). The CIGA-VAL oxide film thickens during the flight of the particle in the spray chamber and powder collection vessel, incorporating oxygen and water into the oxide film. As shown by the QMS results (Figure 4.13) the hydrogen profile of the CIGA-VAL aluminum powder indicates a notable content of hydrated alumina, which is much more than the GARS-4 aluminum powder (Figure 4.14). If the oxide thickness of the CIGA-VAL

powder has not reached its "limiting value" during gas atomization, the oxide film will continue to grow until the limiting value is reached during post-atomization handling, probably near 159 Å for this powder.

The GARS process, on the other hand, utilizes evacuation of the atomization system prior to gas atomization, minimizing any residual oxygen or water contaminants from the atomization system. Also, the UHP nitrogen gas has a negligible oxygen content, further reducing the oxidation potential of the gas. The initial oxide film to form on the GARS aluminum droplets probably forms at a relatively low oxidation temperature, near the droplet solidification time, as interpreted from the atomization time scale model previously discussed (Figure 5.6). Even for the highest atomization pouring temperature used in this research, 1600°C for the GARS-5 aluminum powder, the oxidation is predicted not to begin until near the minimum time of solidification. The evacuation of the atomization system before gas atomization reduces the content of the hydrated alumina constituent of the oxide film, which is significantly lower than the CIGA-VAL powder (Figure 4.16). With respect to the -38 μm, GARS-9, aluminum powders tested for MEC, the post-atomization oxide film was thermally grown to a maximum of about 225 Å. In summary , the conditions under which the oxide film initially forms and continues to grow on aluminum powder surfaces apparently does affect the powder explosibility characteristics. In other words, an atomization process, like GARS, that suppresses high temperature oxidation and minimizes moisture exposure, has been demonstrated to provide aluminum powder with significantly reduced explosive properties.

Aluminum Powder Consolidation

Tap densify and air sinter

The ability to solid state sinter aluminum powders, especially in air, requires the oxide film on the aluminum powder surfaces to be thinner than the "practical limit" of the

oxide film as defined by Hart [97]. Otherwise, if the oxide film on the aluminum powders reaches its limiting thickness, the aluminum cation diffusion through the surface oxide film diminishes, and solid state sintering in negligible. The solid state sintering observed in Figure 4.49 was completed in air at 300°C, because the aluminum oxide film on the GARS-9 aluminum powder had not reached its "practical limit." This thin oxide film, about 27 Å thick, permitted the diffusing aluminum cations of neighboring powder particles to form necks at the contact points between the powder particles. In the case of the CAA aluminum powder, no solid state sintering was observed because the oxide film was apparently too thick, i.e., the oxide film thickness was near its "practical limit."

The opportune time for solid state sintering aluminum powders is immediately after gas atomization. If the powder needs to be stored or shipped for some time, the powder can be packaged either under inert gas as discussed by Williams [2] or under dry air as is done at the Alcoa CAA facility in Rockdale, TX, [3]. The dry air storage atmosphere would be less expensive than the inert gas atmosphere, and as shown in Figure 4.38, dry air does not appear to oxidize the aluminum powder surfaces after 100 days of exposure.

CIP-VHD-HIP and CIP-VCD-HIP consolidation

The gas atomization method selected for producing aluminum powders directly affects the consolidation of the aluminum powders. High hydrated alumina contents, such as those detected in the CAA, CIGA-ATA, and CIGA-VAL aluminum powders by QMS, should be reduced before the aluminum powders are consolidated into components at or near full density. The QMS experiments, conducted for this research, demonstrate that chemisorbed water in the oxide film can react with aluminum cations diffusing through the oxide film to form oxide and hydrogen gas. Inadequate degassing of these aluminum powders can lead to material defects later in the consolidation process or during in-service operation related to the presence of hydrogen trapped along the prior particle boundaries.

The conventional degassing procedure has been a VHD procedure of a CIP aluminum powder billet, such that the porosity of the billet is interconnected to maximize the degassing process. An alternative to the VHD method is to substitute the VHD process with a VCD operation. Such a substitution would help reduce the costs of consolidating aluminum powders by eliminating an elevated temperature process and potentially retain some of the rapid solidified microstructure after the consolidation process.

Figure 4.58 and Figure 4.59 show that the VCD operation is as effective as the VHD process in reducing the physiosorbed water content of the as-atomized powders prior to a HIP consolidation. One may infer that the VCD of as-atomized aluminum powders would also be applicable for other full densification operations, such as direct powder forging and die pressing. However, the VCD does not remove the chemisorbed water in the surface oxide film on aluminum powders as well as the VHD procedure (Figure 4.56 and Figure 4.57). In these figures, the amount of hydrogen evolving from the CIP-VHD-HIP samples is less than from the CIP-VCD-HIP samples. The results of theses QMS analyses are supported by the measured amount of hydrogen in each consolidated sample (Table 4.14).

Other indirect evidence for the VCD procedure not completely removing the chemisorbed water is shown in Figure 4.60. As the heat treatment temperature of the CIP-VCD-HIP route increased to 550°C, more trapped hydrogen evolves from the consolidated samples. Recall from Figure 4.9, the position and singular peak of the hydrogen signal is characteristic of trapped hydrogen evolving from the bulk volume. During the subsequent 300°C and 550°C heat treatments of the HIP sample, the chemisorbed water remaining in the oxide, primarily the monohydroxide, was further reduced as indicated by the increase of the respective area under the hydrogen profiles (Table 4.15).

The hydrogen reduction was not complete though until the heat treating temperature was 550°C. Notice that the area listed for the 550°C heat treated sample is similar to the area listed for the as-atomized powder. Reviewing the hydrogen signal of the as-atomized

powder, the monohydrate transforms to the anhydrous oxide near 550°C. Since the 550°C sample was at temperature for 3 hours, this would seem like plenty of time to convert any remaining hydrated alumina phases to an anhydrous alumina state.

The microstructures of the GARS-4 and CAA powders consolidated by CIP-VCD-HIP and CIP-VHD-HIP are different. In general, the CIP-VCD-HIP microstructures are more dense than the CIP-VHD-HIP microstructures. Two probable explanations can describe the observable differences. The first possibility is that during the VHD process the hydrogen gas produced may have been trapped in isolated pores within the CIP sample. Recall, the CIP density of these samples was above the ideal degassing density mentioned by Kim et al. [42]. During the HIP cycle of the consolidation procedure, the isolated pores with the trapped hydrogen were unable to collapse due to the gas pressure within the voids.

Another reason for the presence of pores in the CIP-VHD-HIP microstructures is inadequate degassing of the CIP-VHD samples prior to welding the vent pipe on the HIP can closed. Recall, after the VHD cycle, the sample was backfilled at room temperature with UHP argon gas and the sample was transferred to an electron beam melter (EBM) chamber for welding the HIP can shut. The evacuation time may not have been long enough to remove the UHP argon gas from CIP-VHD samples in the EBM chamber. If argon gas remained in the porosity of the CIP-VHD sample after welding the HIP can close, then during the HIP cycle, the gas pressure in the void would have been sufficient to inhibit the collapse of the void. To confirm this possibility of the observed porosity, the argon gas could be monitored during a QMS analysis of the CIP-VHD-HIP sample.

Aluminum alloy powder consolidation

The consolidation of aluminum alloy powders, especially elemental blends or prealloyed powders with a few weight percent magnesium, requires knowledge of phase transformations or powder reactions that may occur during elevated temperature processing

of the alloy powders. Magnesium is a uselful and reactive alloy element in aluminum P/M processing. In the case of LPS of elemental blends, the magnesium reacts with the aluminum to form a low melting point eutectic phase at 451°C. This reaction is apparent from the DTA heating curve of the Al-Cu-Mg alloy powder shown in Figure 4.34a. In the case where the aluminum alloy powders were to be sintered in the solid state, the sintering temperature should be below 451°C to avoid any liquid formation.

A closer look at the DTA heating curve in Figure 4.34b shows a deviation from baseline at 432.5°C prior to the aluminum-magnesium liquid formation at 453.7°C. The deviation may be attributed to the reaction of magnesium with the chemisorbed water in the oxide film to form magnesium oxide and hydrogen gas. Confirmation of this possible reaction is observed in a QMS analysis of the same powder (Figure 4.33) which shows a hydrogen spike at 432.3°C. The importance of knowing a reaction temperature as indicated by DTA and QMS is during a VHD procedure of the aluminum powder. At the risk of forming a small volume fraction of liquid, a complete degassing of an aluminum-magnesium based alloy powder could possible be completely degassed slightly above the aluminum-magnesium eutectic temperature. Evidence for this procedure is in Figure 4.35, where a comparison of the water content with a pure aluminum powder produced at the same gas atomization facility as the Al-Cu-Mg alloy powders shows the water content of the Al-Cu-Mg alloy to be more than one order of magnitude lower than the pure aluminum powder.

Punch testing

All the consolidated samples punch tested for this research have nearly ideal load-displacements curve similar to the one described by Kameda [75]. The significance of these nearly ideal punch test curves is that the empirical mechanical property equations described in Chapter 4 are directly applicable for the consolidated samples of aluminum powders. The relatively high ductile nature of the consolidated aluminum powders is illustrated in Figure

4.62 and Figure 4.63. The punch test coupons after testing have "hat" shaped geometries due to the rounded indenter used for punch testing. A magnified view of the fracture surface (Figure 4.63) shows the fracture mode to be pure shear as noted by the ductile tearing of the microstructure.

The intent of punch testing was to statistically evaluate the mechanical properties the CIP-VHD-HIP and CIP-VCD-HIP consolidated samples. Because the different aluminum powders are of varying size, shape, and chemistry, only direct comparisons are valid for a given powder type. The measured mechanical properties for each consolidation sequence, shown in Figures 4.64, 4.65, and 4.66, are statistically insignificant. A similar comment may be made about the measured mechanical properties of the consolidated and heat treated samples plotted in Figures 4.67, 4.68, and 4.69. The punch test evaluation appears to be insensitive to the observable differences of the microstructure and residual hydrogen chemistry of the CIP-VHD-HIP and CIP-VCD-HIP samples. Other mechanical test, such as fatigue testing, are probably more sensitive to microstructural and hydrogen chemistry differences as demonstrated by Kim [61]. The development of a statistically significant fatigue study would require more aluminum powder than was available for this research.

CHAPTER 6. CONCLUSIONS

Throughout this research, the commercial aluminum powders have been benchmarks for making direct comparisons with the GARS aluminum powder. The intent of these comparisons was to illustrate the strong linkage between the gas atomization process conditions, the resulting powder characteristics, and the required powder consolidation sequence. The principles demonstrated for the pure aluminum powders would be applicable to aluminum alloy powders.

The surface oxidation during aluminum particle flight and collection in the atomization system is directly dependent on the residual partial pressures of oxygen and water vapor in the atomization gas and the atomization chamber. The atomization time scale model shows that the oxygen partial pressure affects the final shape of the aluminum powder particles. The model successfully predicts the observed aluminum powder morphologies with the assumption that an initial oxide film thickness of 5 Å on the molten droplet can inhibit spheroidization. The residual water in the atomization gas and spray chamber is chemisorbed into the oxide film and physiosorbed onto the surface of the oxide film. During post-atomization powder handling, if the oxide thickness has not reached its "practical limit" in the atomization system, oxidation continues until the oxide thickness has grown to a maximum value. The rate of post-atomization oxidation of the aluminum particle surfaces is directly proportional to the relative humidity of the handling and storage atmospheres. Alloy elements and exposure temperatures also contribute to the continued growth of the oxide film after gas atomization.

The explosibility hazard of aluminum powders is more severe with aluminum powder particles having high surface areas. The explosibility of aluminum powder is reduced by suppressing high temperature oxidation of the aluminum droplets. The MEC results of the GARS aluminum powders show that oxide film thickness is not a variable affecting powder

explosibility. However, the MEC test may not be sensitive enough to significant changes of oxide thickness. A comparison of the predicted and measured post-atomization surface oxide film thickness on aluminum powder particles shows reasonable agreement for a spherical powder morphology, based on bulk oxygen measurements. The oxide film thickness calculated for CAA aluminum powder is higher than the measured value, primarily due to the irregular shape of the aluminum powder particles.

The CIP-VCD-HIP and CIP-VHD-HIP consolidation experiments demonstrate the possibility of substituting a low temperature vacuum degassing operation for the conventional high temperature vacuum degassing process. A CIP-VCD-HIP consolidated microstructure has less porosity than a CIP-VHD-HIP consolidated microstructure, consistent with a reduction of trapped residual gas. The mechanical properties measured with the small punch test were insensitive to the level of porosity and hydrogen content of the consolidated aluminum samples. Fatigue property measurements are more sensitive to porosity and residual hydrogen in a consolidated aluminum powder microstructure and would probably give a more thorough evaluation of whether or not a VCD process is feasible for consolidation of aluminum powder components.

In summary, the GARS processing methodology offers a number of benefits to the production of aluminum and aluminum alloy powders by gas atomization. The aluminum powder is "clean" with respect to a thinner oxide film and a reduced hydrated alumina content. The GARS aluminum powder has good handling characteristics related to post-atomization oxidation and reduced explosibility hazards. The thin oxide film enhances interparticle bonding during compaction and significantly increases the for solid state sintering rate of aluminum powders. The spherical shape of the aluminum powders would provide good powder flowability and die filling characteristics for pressing and sintering operations. The GARS process should be adaptable to existing commercial gas atomization facilities and applicable to other oxygen sensitive metals.

REFERENCES

1. F.R. Billman, J.C. Kuli, Jr., G.J. Hildeman, J.I. Petit, and J.A. Walker, "Processing of P/MAluminum Alloys X7090 and X7091," *Rapid Solidification Processing: Principles and Technologies III*, ed. R. Mehrabian, National Bureau of Standards, Washington D.C., 1983, pp. 532-546.

2. J.E. Williams, Jr., "Production of Aluminum Powder," *ASM Metals Handbook*, 9th ed., Vol. 7, American Society for Metals, Metals Park, OH, 1984, pp. 125-130.

3. R. Selgelid, Private Communication, Alcoa, Rockdale, TX, July, 1997.

4. A. Ünal, Private Communication, Alcoa, New Kensington, PA, April, 1998.

5. J.W. Bohlen, R.J. Kar, and G.R. Chanani, "A Comparative Evaluation of Aluminum Alloy Powders Used for Fabricating High-Strength Powder Metallurgy Extrusions," *Rapidly Solidified Powder Aluminum Alloys*, ed. by M.E. Fine and E.A. Starke, Jr., ASTM Special Technical Publication 890, Philadelphia, PA, 1986, pp. 166-185.

6. B. van Hoose, Private Communication, Alcan-Toyo America, Napierville, IL, August, 1998.

7. A. Ünal, Private Communication, Alcoa, New Kensington, PA, June, 1997.

8. G.T. Campbell, Private Communication, Valimet, Inc., Stockton, CA, September, 1998.

9. G.T. Campbell, R.W. Christiensen, D.L. Oberholtzer, and R.R. Phillips, "Low Temperature Passivated Aluminum Powder, Properties and Benefits," *Advances in Powder Metallurgy and Particulate Materials - 1997*, compiled by R.A. McKotch and R. Webb, Metal Powder Industries Federation, Princeton, NJ, Vol. 1, part 10, 1997, pp. 3-10.

10. L. Nyborg and I. Olefjord, "Surface Oxidation of Steel Powder During Atomization," *Key Eng. Matls.*, Vol. 29-31, 1989, pp. 9-20.

11. L. Nyborg and I. Olefjord, "Surface Analysis of Ultrasonically Gas Atomized Aluminium and Aluminium Alloy Powders," *Internatl. J. Rapid Solid.*, Vol. 4, 1989, pp. 271-286.

12 O.S. Nichiporenko, and Yu.I. Naida, "Fashioning the Shape of Sprayed Powder Particles," *Sov. Powd. Metall. and Met. Cer.*, Vol. 10, No. 7, 1968, pp. 753-755.

13. S. Özbilen, A. Ünal, and T. Sheppard, "Influence of Oxygen on Morphology and Oxide Content of Gas Atomized Aluminium Powders," *Physical Chemistry of Powder Metals: Production and Processing*, ed. W.M. Small, The Minerals, Metals, & Materials Society, 1989, pp.489-505.

14. L. Goumiri and J.C. Joud, "Auger Electron Spectroscopy Study of Aluminum-Tin Liquid System, " *Acta Metall.*, Vol. 30, 1982, pp. 1397-1405.

15. F. Spaepen and D. Turnbull, "Negative Pressures and Melting Point Depression in Oxide-Coated Liquid Metal Droplets", *Scripta Metall.*, Vol. 13, 1979, pp. 149-151.

16. L. Nyborg and I. Olefjord, " Degassing of USGA-atomized Al-5Mn-6Cr Powder After Exposure to a Humid Atmosphere," *Matls. Sci. Eng.*, Vol. A134, 1991, pp. 1225-1228.

17. A. Ünal, "Effect of Processing Variables on Particle Size in Gas Atomization of Rapidly Solidified Aluminium Powders, *Matls. Sci. Tech.*, Vol. 3, 1987, pp. 1029-1039.

18. J.F. Flumerfelt, I.E. Anderson, and T.W. Ellis, "Thermodynamic Assessment of Gas Atomization Reaction Synthesis," *Applications of Thermodynamics in the Synthesis and Processing of Materials,* ed. by P. Nash and B. Sundman, The Minerals, Metals & Materials Society, 1995, pp. 49-60.

19. T.J. Carney, P. Tsakiropoulos, J.F. Watts, and J.E. Castle, "Oxidation and Surface Segregation in Rapidly Solidified Aluminum Alloy Powders, *Internatl. J. Rapid Solid.*, Vol. 5, 1990, pp.189-217.

20. F.V. Lenel, *Powder Metallurgy - Principles and Applications*, Metal Powder Industries Federation, Princeton, NJ, 1980.

21. R.M. German, *Powder Metallurgy Science*, second edition, Metal Powder Industries Federation, Princeton, NJ, 1994.

22. H. Schlich, M. Thumann, and G. Wirth, "Effect of Degassing on Microstructure of Rapidly Solidified Aluminium Powder," *P/M Aerospace Materials*, Paper 31, 1987, pp. 31.1-31.19.

23. H. Schlich, M. Thumann, and W. Bunk, "Degassing Effects on Oxides in P/M Aluminium Alloys," *Solid State Powder Processing*, ed. by A.H. Clauer, and J.J. deBarbadillo, The Minerals, Metals and Materials Society, 1990, pp. 111-125.

24. J.L. Estrada and J Duszczyk, "Surface Oxide Film Analysis of Rapidly Solidified Aluminium Alloys by Auger Electron Spectroscopy," *Advances in Powder Metallurgy and Particulate Materials - 1994*, Metal Powder Industries Federation, Princeton, NJ, Vol. 2, 1994, pp. 141-155.

25. S.J. Davis, A.P. Miodownik, and J.F. Watts, "Degassing and Surface Analysis of Gas Atomized Aluminium Alloy Powders," *J. Matls. Sci.*, Vol. 30, 1995, pp. 3811-3819.

26. J.F. Flumerfelt and I.E. Anderson, "High Purity Aluminum Powder Processed Using High Pressure Gas Atomization," *Advances in Powder Metallurgy and Particulate Materials - 1996*, ed. by T.M. Cadle and K.S. (Sim) Narasimhan, Metal Powder Industries Federation, Princeton, NJ, Vol. 1, Part 1, 1996, pp. 87-96.

27. L. Ackermann, I. Guillemin, R. Lalauze, and C. Pijolat, "Study of Water Desorption During Degassing of Aluminium Powders," *High Strength Powder Metallurgy Aluminum Alloys II*, ed. G.J. Hildeman and M.J. Koczak, The Metallurgical Society, Warrendale, PA, 1985, pp. 175-191.

28. A.I. Litvintsev and L.A. Arbuzova, "Kinetics of Degassing of Aluminum Powders," *Sov. Powd. Metall. and Metal Cer.*, Vol. 1, No. 49, 1967, pp. 1-10.

29. L. Kowalski, B.M. Korevaar, and J. Duszczyk, "Some New Aspects on the Theory of Oxidation and Degassing of Aluminium-Based Alloy Powders," *J. Matls. Sci.*, Vol. 27, 1992, pp. 2270-2780.

30. D.T. Peterson, P.B. Wheelock, and L.L. Jones, "A Modern Hot Vacuum Extraction System for Analyzing Metals for Hydrogen, in press, 1998.

31. F. Degrève, J-C. Carle, and N. Gonzalez, "New Methods for the Determination of Hydrogen Content of Aluminum and its Alloys: Part I. Improvements in the Vacuum Extraction Method," *Met. Trans. B*, Vol. 6B, 1975, pp. 539-544.

32. R.A. Outlaw, D.T. Peterson, and F.A. Schmidt, "Diffusion of Hydrogen in Pure Large Grain Aluminum," *Scripta Metall.*, Vol. 16, 1982, pp. 287-292.

33. D.T. Peterson, Private Communication, Ames Laboratory, Ames, IA, 1997.

34. M. Jacobson, A.R. Cooper, and J. Nagy, "Explosibility of Metal Powders," *Bureau of Mines, Report of Investigations*, 6516, U.S. Department of the Interior, Bureau of Mines, 1964.

35. K.L. Cashdollar and M. Hertzberg, "20-L Explosibility Test Chamber for Dusts and Gases," *Review of Sci. Instru.*, Vol. 56, 1985, pp. 596-602.

36. C.J. Dahn, B. Reyes, and A. Kashani, "Dust Explosibility Parameters for Metal Powders," *Processing and Handling of Powders and Dusts*, ed. by T.P. Battle and H. Henein, The Minerals, Metals & Materials Society, 1997, pp. 93-102.

37. A. Ünal, Private Communication, Alcoa, New Kensington, PA, October, 1995.

38. V.M. Boborykin, V.M. Gremyachkin, A.G. Istratov, V.I. Kolenikov-Svinarev, G.P. Kuznetsov, O.I. Leipunskii, and V.M. Puchkov, "Effects of Nitrogen on the Combustion of Aluminum," *Combustion, Explosion, and Shock Waves*, November, 1983, pp. 270-276.

39. D. Prentice, *Combust. Sci. Tech.*, Vol. 1, No. 5, 1970.

40. R. Bouriannes and N. Manson, *C.R. Acad. Sci. Paris*, Vol. 274, 1971, p. 817.

41. R. Bouriannes, A. Hardy, and N. Manson, *C.R. Acad. Sci. Paris*, Vol. 272, 1971, p. 561.

42. Y-W. Kim, W.M. Griffith, and F.H. Froes, "Surface Oxides in P/M Aluminum Alloys," *J. Metals*, August, 1985, pp. 27-33.

43. J.E. Davidson, "Compressibility of Metal Powders," *ASM Metals Handbook*, 9th ed., Vol. 7, American Society for Metals, Metals Park, OH, 1984, pp. 286-287.

44. R.W. Stevenson, "P/M Lightweight Metals," *ASM Metals Handbook*, 9th ed., Vol. 7, American Society for Metals, Metals Park, OH, 1984, pp. 741-764.

45. K.B. Patel, "Flow Rate of Metal Powders," *ASM Metals Handbook*, 9th ed., Vol. 7, American Society for Metals, Metals Park, OH, 1984, pp. 278-279.

46. F.V. Lenel, "Physical Fundamentals of Consolidation," *ASM Metals Handbook*, 9th ed., American Society for Metals, Metals Park, OH, Vol. 7, 1984, pp. 308-321.

47. S. Sun, "The Effect of Liquid Formation and Spreading on the Sintering Process and Mechanical Properties of Al-Cu-Mg-Si P/M Alloys," Ph.D. Thesis, Michigan Technological University, 1992.

48. S.S. Gutin, A.A. Panov, and M.I. Khlopin, "Effect of Oxide Films in the Sintering of Aluminum Powders," *Poroshkovaya Metall.*, Vol. 4, No. 12, 1972, pp. 32-35.

49. Z.A. Munir, "Surface Oxides and Sintering of Metals," *Powd. Metall.*, Vol. 24, No. 4, 1981, pp. 177-180.

50. R.M. German, *Sintering Theory and Practice*, Metal Powder Industries Federation, Princeton, NJ, 1996.

51. S. Storcheim, "Air Sintering Improves Aluminum P/M Economics," *Precis. Met.*, Vol. 32, No. 6, 1974, pp. 54-55.

52. W. Hunt, Jr., Private Communication, Alcoa Technical Center, Pittsburgh PA, September, 1993.

53. H. Jones, "Observations on the Structural Transition in Aluminum Alloys Hardened by Rapid Solidification", *Mater. Sci. Eng.*, Vol. 5, 1969/70, pp. 1-18.

54. D.L. McDanels, "Analysis of Stress-Strain, Fracture, and Ductility Behavior of Aluminum Matrix Composites Containing Discontinuous Silicon Carbide Reinforcement", *Metall. Trans.*, Vol. 15A, 1984, pp. 139-146.

55. W.M. Griffith, R.E. Sanders, Jr. and G.J. Hildeman, "Elevated Temperature Aluminum Alloys for Aerospace", *High Strength Powder Metallurgy Aluminum Alloys*, ed. by G.J. Hildeman and M.J. Koczak, The Metallurgical Society, Warrendale, PA, 1982, pp. 209-224.

56. D.J. Skinner, K. Okazaki, and C.M. Adam, "Physical Metallurgy and Mechanical Properties of Aluminum Alloys Containing Eight to Twelve Weight Percent Iron," *Rapidly Solidified Powder Aluminum Alloys*, ed. by M.E. Fine and E.A. Starke, Jr., ASTM Special Technical Publication 890, Philadelphia, PA, 1986, pp. 211-236.

57. M.J. Couper and R.F. Singer, "Influence of Cooling Rate on Microstructure and Mechanical Properties of Rapidly Solidified Al-Fe-X Alloys," *High Strength Powder Metallurgy Aluminum Alloys II*, ed. by G.J. Hildeman and M.J. Koczak, The Metallurgical Society, Warrendale, PA, 1986, pp. 199-211.

58. S.D. Kirchoff, R.H. Young, W.M. Griffith, and Y.W. Kim, "Microstructure/Strength/Fatigue Crack Growth Relations in High Temperature P/M Aluminum Alloys," *High Strength Powder Metallurgy Aluminum Alloys*, ed. by G.J. Hildeman and M.J. Koczak, The Metallurgical Society, Warrendale, PA, 1982, pp. 237-248.

59. C.M. Adam and S.K. Das, "The Design of New Engineering Alloys Using Rapid Solidification Technology", *Rapid Solidification Processing: Principles and Technologies IV*, ed. by R. Mehrabian and P.A. Parrish, Claitor's Publishing Division, Baton Rouge, LA 1988, pp. 66-81.

60. P.P. Millian, "Application to High-Temperature Powder Metal Aluminum Alloys to Small Gas Turbines", *High Strength Powder Metallurgy Aluminum Alloys*, ed. by G.J. Hildeman and M.J. Koczak, The Metallurgical Society, Warrendale, PA, 1982, pp. 225-236.

61. Y-W. Kim, "Effect of Non-Uniform Microstructure and Hydrogen in High Temperature P/M Aluminum Alloy Al-8.4Fe-7.2Ce," *Progess in Powder Metallurgy*, Vol. 43, 1987, pp. 13-31.

62. I.E. Anderson, B.K. Lagrasso, and T.W. Ellis, "Gas Atomization Synthesis of Refractory or Intermetallic Compounds and Supersaturated Solid Solutions," U.S. Patent No. 5,368,567.

63. T.B. Massalski, *Binary Alloy Phase Diagrams*, second edition, Vol. 1, American Society for Metals, Metals Park, OH, 1990, pp. 176-177.

64. K.A. Gschneidner, Jr. and Nancy Kippenhan, "Thermochemistry of the Rare Earth Carbides, Nitrides, and Sulfides for Steelmaking," IS-RIC-5, Rare-Earth Information Center, Iowa State University, Ames, IA, 1972.

65. K.A. Gschneidner, Jr., Nancy Kippenhan and O.D McMasters, "Thermochemistry of the Rare Earths," IS-RIC-6, Rare-Earth Information Center, Iowa State University, Ames, IA, 1973.

66. P. Sthapitanonda and J.L. Margrave, "Kinetics of Nitridation of Magnesium and Aluminum," *J. Phys. Chem.*, Vol. 60, No. 12, 1956, pp. 1628-1633.

67. J.F. Flumerfelt and I.E. Anderson, "Gas Atomization Reaction Synthesis," *Processing and Fabrication of Advanced Materials III*, ed. by V.A. Ravi, T.S. Srivatsan, and J.J. Moore, The Minerals, Metals & Materials Society, 1994, pp. 475-486.

68. I.E. Anderson, R.S. Figliola, and H. Morton, "Flow Mechanisms in High Pressure Gas Atomization," *Matls. Sci. Eng.*, Vol. A148, 1991, pp. 101-114.

69. P.J. Heinzer, "Pycnometry", *ASM Metals Handbook*, 9th ed., Vol. 7, American Society for Metals, Metals Park, OH, 1984, pp. 265-266.

70. H.J. van Beek and E.J. Mittemeijer, "Amorphous and Crystalline Oxides on Aluminium," *Thin Solid Films*, Vol. 122, 1984, pp. 131-151.

71. M. Conserva and P. Fiorini, "Interpretation of Quench-Sensitivity in Al-Zn-Mg-Cu Alloys," *Met. Trans. A*, Vol. 4A, 1973, pp. 857-862.

72. M. Grootfeld, Private Communication, Engineering Services, Ames Laboratory, Ames, IA, April, 1998.

73. K.L. Cashdollar, "Flammability of Metals and Other Elemental Dust Clouds," *Process Safety Prog.*, Vol. 13, No. 3, 1994, pp. 139-145.

74. J.F. Flumerfelt, I.E. Anderson, and J.C. Foley, "Consolidation of Pure Aluminum Powders," *Advances in Powder Metallurgy and Particulate Materials - 1997*, NJ, Vol. 1, part 10, 1997, pp. 11-19.

75. J. Kameda, "Development of Small Punch Testing Technique and its Application To Evaluation of Mechanical Properties Degradation," *Non-Destructive Evaluation and Material Properties II*, ed. by P.K. Liaw, O. Buck, R.J. Arsenault, and R.E. Green, Jr., The Minerals, Metals & Materials Society, 1994, pp. 43-60.

76. B.H. Kaye and R. Trottier, "The Many Measures of Fine Particles," *Chem. Eng.*, April, 1995, pp. 78-86.

77. T.B. Massalski, *Binary Alloy Phase Diagrams*, second edition, Vol. 1, 1990, pp. 147-149.

78. J.C. Foley, "Rapid Solidification Processing of Aluminum-Rare Earth Alloys", Ph.D. Thesis, University of Wisconsin, Madison, WI, 1997.

79. R.A. Outlaw, D.T. Peterson, and F.A. Schmidt, "Hydrogen Partitioning in Pure Cast Aluminum as Determined by Dynamic Evolution Rate Measurements," *Met. Trans. A*, Vol. 12A, 1981, pp. 1809-1816.

80. R.D. Craig and E.H. Harden, "The Interpretation of Mass Spectra in Vacuum Measurement," *Vacuum*, Vol. 16, No. 2, 1966, pp. 67-73.

81. M. Norell, L. Nyborg, and I. Olefjord "Thickness Determination of Surface Oxides on Metal Powder by AES Depth Profiling," *Surf. Interface Anal.*, 1992, pp. 71-76.

82. T.B. Massalski, *Binary Alloy Phase Diagrams*, second edition, Vol. 1, American Society for Metals, Metals Park, OH, 1990, pp. 236-237.

83. T.B. Massalski, *Binary Alloy Phase Diagrams*, second edition, Vol. 1, American Society for Metals, Metals Park, OH, 1990, pp. 225-227.

84. L. Nyborg and I. Olefjord, "Surface Analysis of Air Exposed Rapidly Solidified Aluminium Powder," *Powd. Metall.*, Vol. 36, No. 3, 1993, pp. 193-197.

85. David Cann, Private Communication, Iowa State University, Ames, IA, April, 1998.

86. R.J. Fruehan, "Gases in Metals," *ASM Handbook*, 10th ed., Vol. 15, American Society for Metals, Metals Park, OH, 1988, pp. 82-87.

87. R.W. Hertzberg, *Deformation and Fracture Mechanics of Engineering Materials*, third edition, John Wiley & Sons, Inc., 1989.

88. J.B. See and G.H. Johnston, "Interactions Between Nitrogen and Liquid Lead and Tin Streams," *Powd. Tech.*, Vol. 21, 1978, pp. 119-133.

89. R.H. Perry and C.H. Chilton, Chemical Engineers' Handbook, 5th ed, 1973, Table 3-299.

90. J. Ting, Private Communication, Ames Laboratory, Ames, IA, May, 1998.
91. E.A. Brandes, Smithells Metals Reference Book, 6th ed., Butterworth & Co Ltd., England, 1983.

92. T. Chapman, "The Viscosity of Liquid Metals", *AIChE Journal*, Vol. 12, 1966, pp. 395-400.

93. Outokumpu HSC Chemistry for Windows, version 3.0, 1996.

94. Air Products and Chemicals, Specialty Gas Department, Allentown, PA.

95. *CRC Handbook of Chemistry and Physics*, ed. R.C. Weast, 66th ed., 1985-1986, F-20, Ref. 199.

96. K. Wefers, "Properties and Characterization of Surface Oxides on Aluminum Alloys," *Aluminium*, Vol. 57, No. 11, 1981, pp. 722-726.

97. R.K. Hart, "The Oxidation of Aluminium in Dry and Humid Oxygen Atmosphers," *Proc. Royal Soc., London*, Vol. A236, 1956, pp.68-88.

98. W.D. Kingery, H.K. Bowen, and D.R. Uhlmann, *Introduction to Ceramics*, 2nd. ed., John Wiley & Sons, New York, NY, 1976.

99. T.J. Carney, J.E. Castle, P. Tsakiropoulos, M.B. Waldron, and J.F. Watts, "Surface Studies of Rapidly Solidified Aluminium Alloy Powder," *Key Eng. Matls.*, Vol. 29-31, 1989, pp. 291-302.

100. A.M. Huntz, "Effect of Active Elements on the Oxidation Behaviour of Al_2O_3-Formers," *The Role of Active Elements in the Oxidation Behaviour of High Temperature Metals and Alloys*, Elsevier Science Publishers, Essex, England, 1989.

101. J. Jedlinski, "The Influence of Reactive Elements on the Oxidation Behaviour of Alumina Formers - Review Paper, *Proc. 11th Internatl. Corros. Congress*, Vol. 4, 1990, pp.4.21-4.29.

102. R. Prescott and M.J. Graham, "The Formation of Aluminum Oxide Scales on High-Temperature Alloys," *Oxid. Metals*, Vol. 38, Nos. 3-4, 1992, 233-254.

103. P. Choquet, Doctor Thesis, University Paris XI, Orsay, France, 1987.

104. H.E. Evans, "Stress effects in High Temperature Oxidation of Metals," *Internatl. Matls. Rev.*, Vol. 40, No. 1, 1995, pp. 1-40.

105. M. Schütze, *Protective Oxide Scales and Their Breakidown*, Wiley, Chichester, NY, 1997.

ACKNOWLEDGMENTS

I would like to first thank my wife and family for their encouragement and support during my research years at Iowa State University. My advisor Dr. Iver E. Anderson is especially thanked for his role as my advisor, mentor, and friend. Dr. James C. Foley is also thanked for his probing questions, interpretation, and insight about the research problems that occurred.

For the analytical results presented in my thesis, I thank the Ames Laboratory staff. The aluminum powder production and powder handling was conducted by Bob Terpstra, Eric Zoellner, Gary Houston, and the undergraduate hourly workers. The powder size distribution was done by Bob Terpstra. Kevin Dennis gathered the DTA results of the as-atomized pure aluminum and aluminum alloy powders. The analytical chemistry results were done by Bob Hofer, Cheryl Kamman, and Chris Gross. Hal Sailsbury did the metallographic preparation of the as-atomized and consolidation aluminum powders. He also took optical micrographs and developed the pictures for publication. Fran Laabs dedicated extensive SEM time to the micrographs of the as-atomized and consolidated aluminum powder samples. He also was instrumental in operating the TEM for the oxide film characterization study. Tamara Bloomer conducted the AES evaluations of the oxide film thickness measurements. James Anderegg did an outstanding job in helping to gathering and interpret the QMS data. He helped design, assemble, operate, and maintain the QMS system.

The Materials Preparation Center is thank for their metal production, powder consolidation, and cutting the punch test coupons. The punch test coupons were mechanically ground by hourly undergraduate students Matt Anderson and Mike Lane. Arne Swanson and Andy Kilborn mechanically tested the samples and collected the data. Jun Kameda is thanked for his role in interpreting the punch test results. The Ames Lab electrical and mechanical

sections are thanked for their roles in designing, machining, and assembling various experimental equipment.

My gratitude for monetary support is extended to the Materials Science Division of U.S. DOE-BES under contract number W-7405-Eng-82 and EE-OTT USAMP CRADA No. 96-MULT-AMP-0444 (B&R No. EE-07-02). The United States government has assigned the DOE Report number IS-T 1858 to this thesis.

IMAGE EVALUATION
TEST TARGET (QA-3)

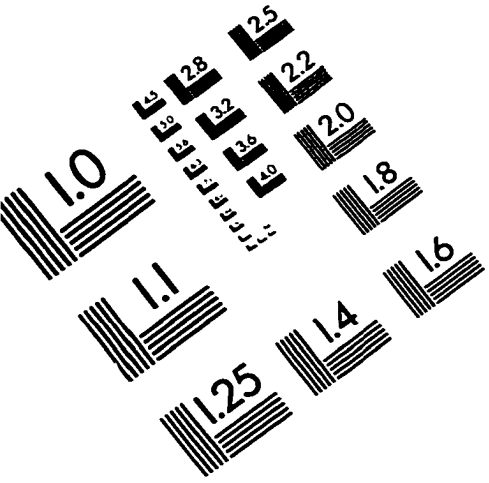

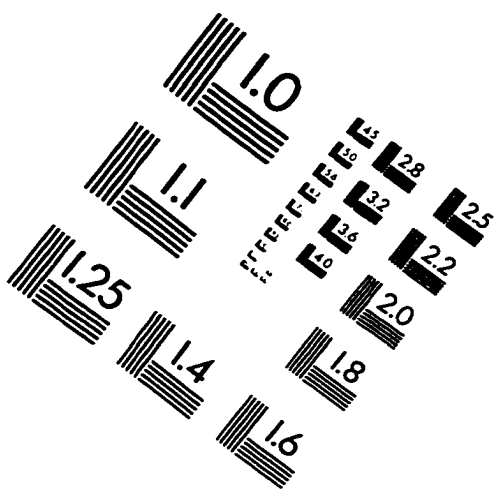

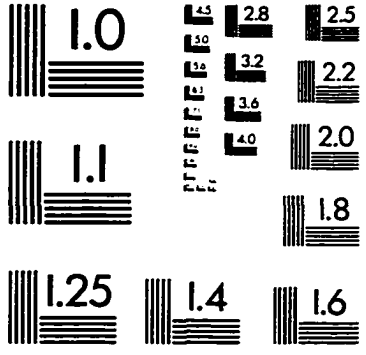

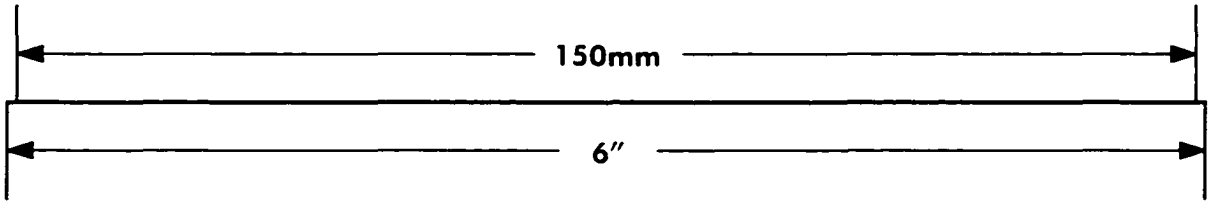

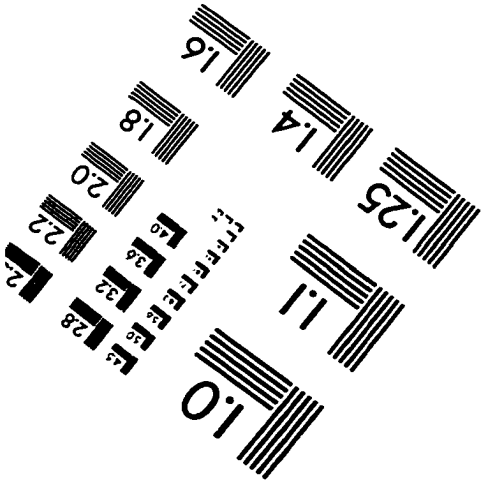

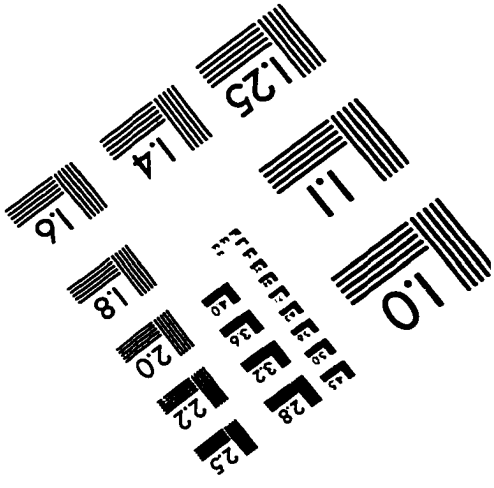

APPLIED IMAGE, Inc
1653 East Main Street
Rochester, NY 14609 USA
Phone: 716/482-0300
Fax: 716/288-5989